TUD Civil Engineering
Concrete Structures

Usage of FBG fiber optic sensors to monitor the structural behaviour of a geopolymer concrete structural member

J. F. Chan

Master Thesis

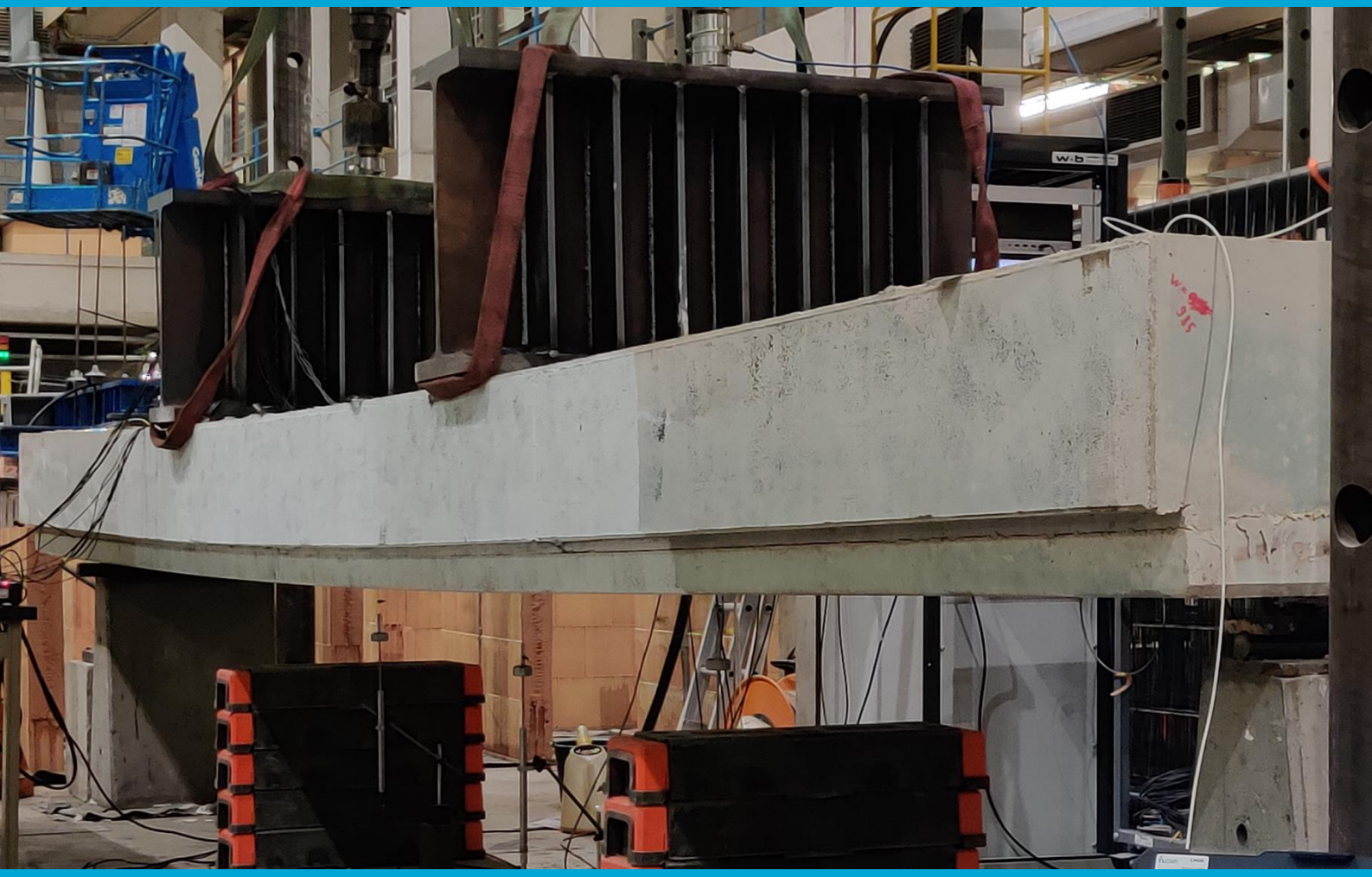

TU Delft

Usage of FBG fiber optic sensors to monitor the structural behaviour of a geopolymer concrete structural member

By

Ji Fan Chan

Master's Thesis

Master of Science in Civil Engineering
Master track: Structural Engineering – Concrete Structures
Delft University of Technology

Student number: 4293096

Thesis committee:	Dr. ir. Y. Yang,	TU Delft, Chairman
	Dr. M. Poliotti	TU Delft, Daily Supervisor
	Dr. G. Ye	TU Delft

Preface

This thesis is the result of many months of work. I was allowed to join the large ongoing geopolymer concrete experimental program with a final goal being the realization of an actual geopolymer concrete bridge deck in Friesland, The Netherlands. This project has allowed me to broaden my horizons regarding new monitoring techniques and a different form of concrete I was never aware of. The thesis research and writing did result in stretching out the project as there was just so much data to consider. Balancing the thesis work while still working part-time at my parents' snack bar/cafetaria was rough, but I would not have it any other way.

I would like to thank Yuguang Yang and Guang Ye for their guidance and feedback on the thesis and research during the committee meetings. Their patience and willingness to share knowledge was very useful and motivating. Special thanks to Yuguang for allowing me to slot into this ongoing project, when I displayed interest in this thesis subject.

I would also like to thank Mauro for his daily supervision and guidance during the entire thesis process, his suggestions during critical parts of the research and feedback on the thesis structure and document helped in shaping the final form of this thesis, along with thesis structure feedback from Yuguang.

I also owe my thanks to the Shizhe, Hao and Zhenxu for their willingness to answer questions and sharing data regarding the sensor setups, data from other monitoring techniques, and their general companionship during the testing days in Ghent.

Finally I would like to thank my parents, their many years of hard work in the shop allowed me to pursue a degree at the TU Delft. Their everlasting support gave me motivation and drive during these years.

Ji Fan Chan
Maassluis, March 2023

Abstract

Geopolymer concrete, a relatively new building material has been suggested as an alternative to Ordinary Portland Cement (OPC) based concretes for within the building sector, due to it having a relatively low CO2 emission during production. An issue with geopolymer concrete however, is that high amounts of early age creep, shrinkage and decrease in elastic modulus over time has been observed which in conjunction with the existing research on geopolymer concrete having been predominantly conducted in laboratory settings, leads to questions about the applicability of these findings and thus the use of geopolymer concrete as a replacement for OPC based concretes in concrete structures. To address this issue, this study makes use of Fiber Bragg Grating (FBG) fiber optic sensors, placing them within reinforced steel which in turn are placed inside geopolymer concrete to obtain data that is more applicable to real world settings compared to prior findings observed within laboratory settings.

Four precast prestressed geopolymer concrete girders are produced and rebars containing FBG fiber optic sensors are placed prior to casting. Measurements before and after the release of prestressing are analysed to determine the apparent transmission length of the prestressing strands and compared to methods defined by Eurocode EN 1992-1-1. The applicability of these guidelines is evaluated, as these are intended for use with conventional concretes. The changes in strain over time, and elastic modulus changes during curing of the precast girder is monitored and analysed, focusing on the effect of time dependent changes of the concrete to the effectiveness of the prestressing forces. The girders are combined with a geopolymer concrete topping to form two beams and one slab. The beams are subject to a flexural test and a shear test respectively. The slab undergoes a cyclic loading test before being tested in two critical point load locations in two separate tests. The FBG measurements gained during the tests are evaluated using analytical methods.

The results show that the FBG fiber optic sensors integrated into steel rebar can deliver strain measurements in locations conventional strain sensors cannot be applied. The FBG data suggests that conventional concrete transmission length guidelines are applicable to this geopolymer concrete mixture. As the FBG-integrated rebars were all placed in the same location in the precast girder cross section, the strains measured by these FBGs are only representative of concrete near the core of the girder, where the concrete is not exposed to drying conditions. And because this geopolymer concrete is susceptible to drying, the difference between measurements and expected values such as the elastic modulus and the drying shrinkage can be explained by the low amount of drying that the concrete in the core of the girder experiences. Due to the positioning of rebar in the cross section of the precast girder in this study, crack initiation during the flexural test was not detected. The occurrence of cracks is detected in the measured strains as it diverged from the linear elastic model during the crack propagation phase. This shows that the cross sectional position of the sensors is important for the desired function and role of concrete in-situ FBG monitoring.

Overall, the data that the (rebar-integrated) FBG strain sensors can provide can be of great use towards the larger task of bringing geopolymer concrete structures to a real life application. In-situ FBG strain data of the precast prestressed girders provide additional information into the application of this SCGC mixture in larger scale structural elements. This data is a useful addition to the data gained through conventional methods, and results from lab testing. FBG monitoring can provide strain data from the core of structural elements, giving an insight of the behaviour during curing and (destructive) testing that is otherwise difficult to obtain.

Contents

Symbols and abbreviations

Symbols

Latin upper case

A	Strain coefficient [$\mu\varepsilon^{-1}$]
A_c	Area of the concrete section
A_p	Area of prestressing steel in the section
B	Strain coefficient [°C]
E	Elastic modulus
E_c	Elastic modulus of the concrete
$E_{cm}(t)$	Elastic modulus of the concrete at a specific timeframe t
E_p	Elastic modulus of prestressing steel
E_s	Elastic modulus of steel rebar
F	Force (general)
F_{piston}	Piston force
F_{pi}	Initial prestressing force
F_{Pm0}	Prestressing force at time t=0
F_{pmax}	Maximum prestressing force
I_c	Second moment of area of the concrete
I_{zz}	Second moment of area around the z-z axis
K	Principal lateral distribution coefficient
L	Span length
M	Moment (general)
M_{ecc}	Moment due to eccentricity of the working forces of the strands
M_{eg}	Moment due to own weight
T	Temperature
T_0	Initial temperature
T_{act}	Actual temperature
T_{s1}	Temperature sensitivity 1
T_{s2}	Temperature sensitivity 2
T_{s3}	Temperature sensitivity 3
V_{Ed}	Shear force

Latin lower case

a	Distance from point load to support in beam formula
$a1$	Span as used in formulas for Guyon-Massonnet method
a_p	Effective centre of prestressing forces
b	Half of the slab width
$b1$	Width value as used in formulas for Guyon-Massonnet method
f_{bpd}	Bond strength for anchorage in the ultimate limit state
f_{bpt}	Bond stress between concrete and tendons
f_{cm}	Mean compressive strength of concrete at 28 days
f_{ctd}	Design tensile value of concrete strength
f_{ctm}	Mean tensile value of concrete strength

f_{pk}	Characteristic value of the tensile strength of prestressing steel
l_{bpd}	The total anchorage length for anchoring a tendon
l_{pt}	Transmission length
l_{pt2}	Upper design value of transmission length
k	Gauge factor
n	Elastic modulus ratio
n_c	Average refractive index of the grating
q_{eg}	Load per unit of length due to own weight
s_{rm}	Crack spacing
s_{rm0}	Crack spacing coefficient
t	Time after tensioning
w	Deflection
z	General indicator of distance to centre of gravity
z_{cog}	Location of centre of gravity in the cross section
z_{cp}	Distance from centre of prestressing strands to centre of gravity

Greek letters

α	Angle between the shear reinforcement and the beam axis perpendicular to the shear force
α_{ct}	Value used for calculation of design tensile strength as stated by the National Annex
α_1	Value used for transmission length calculation involving tendon release
α_2	Value used for transmission length calculation involving tendon details
α_δ	Change of the refraction index
σ_{pi}	Initial prestressing stress
$\beta_{cc}(t)$	Coefficient which depends on the age of the concrete
γ_c	Partial safety factor for concrete
ϵ	Strain
ϵ_c	Strain in concrete
ϵ_{cs}	Strain in concrete due to shrinkage
ϵ_m	Mechanical strain
ϵ_s	Strain in steel
η_1	Bond condition factor
η_{p1}	Coefficient that takes into account the type of tendon used and the bond situation at release
θ	Angle (general use)
θ_2	Value for stiffness and geometry relation in Guyon-Massonnet formulas
λ	Coefficient for crack spacing =
λ_{act}	Actual measured strain wavelength
λ_b	Reflected wavelength/Bragg wavelength
λ_0	Initial strain wavelength
$\lambda_{T,act}$	Actual temperature wavelength
$\lambda_{T,ref}$	Reference temperature wavelength
μ	Eurocode 1992-1-1 formula 3.29 calculation factor
ρ	Reinforcement ratio
ρ_d	Density

ρ_x	Average bending stiffness per unit width around local x-axis
ρ_y	Average bending stiffness per unit width around local y-axis
ρ_{1000}	Relaxation loss (in %) at 1000 hours after tensioning at a mean temperature of 20°C
σ_c	Stress in concrete
$\sigma_{cpi,55}$	Stress in concrete at 55 mm above the bottom of the girder
$\sigma_{cpi,100}$	Stress in concrete at 100 mm above the bottom of the girder
$\sigma_{c,eg}$	Stress in concrete due to own weight
$\sigma_{c,FBG}$	Stress in concrete at FBG level
$\sigma_{c,Pm0}$	Stress in concrete due to prestressing forces at time t=0
$\sigma_{c,QP}$	Stress in the concrete adjacent to the tendons, due to self-weight, initial prestress and other quasi-permanent actions where relevant
σ_{pd}	Tendon stress according to EC2 formula 8.21
σ_{pm0}	Tendon stress just after release
$\sigma_{pm\infty}$	Tendon stress after all losses
σ_s	Steel stress
τ_{b0}	Bond shear stress prior to yielding
φ	Creep factor
ϕ (Ø)	Nominal diameter of prestressing tendon
$\Delta\epsilon$	Strain shift
$\Delta\sigma$	Change in stress
$\Delta\sigma_{pr}$	Relaxation stress loss of prestressing strands
$\Delta\sigma_{c+s+r}$	Prestressing stress loss due to creep, shrinkage, relaxation over time
ΔF	Change in (piston) force
ΔF_{pel}	Elastic force loss of prestressing strands
ΔF_{pr}	Relaxation force loss of prestressing strands
ΔM	Change in bending moment
ΔP_c	Prestressing force loss due to creep over time
ΔP_r	Prestressing force loss due to relaxation over time
ΔP_s	Prestressing force loss due to shrinkage over time
ΔP_{c+s+r}	Prestressing force loss due to creep, shrinkage, relaxation over time
ΔT	Change in temperature
Λ	Period of refractive index modulation

Abbreviations

AAM	Alkali-activated material
DIC	Digital image correlation
EC2	Eurocode 1992-1-1 (Eurocode 2)
FBG	Fiber Bragg grating
LVDT	Linear variable differential transformer
OPC	Ordinary Portland cement
SCGC	Self-compacting geopolymer concrete

1 Introduction

1.1 Environmental impact of concrete

Concrete is one of the most used building materials in the modern world due to its valued properties, such as strength, durability, availability, and workability to name a few. Due to rapid urbanization in developing areas in combination with a population growth, the demand for affordable housing and buildings, and thereby concrete will continue to grow. (The Boston Consulting Group, 2013).

Concrete is comprised of a mixture of components, the basic components are water, binder, and filler materials such as gravel and sand (also called aggregates). The most commonly used binder material is ordinary Portland cement (OPC), made by pulverizing cement clinker. This binder material undergoes chemical reactions when combined with water, also known as hydration. The hydration refers to the chemical reactions of water with cement particles present in OPC. Combining this cement paste with the aggregate mixture will result in concrete. The cement paste will continue to harden, as hydration processes continue as long as there is water to react with unhydrated cement particles (Michael S. Mamlouk, 2018).

Due to the production processes for OPC, a large amount of CO2 is released into the air: The chemical reaction responsible for most of the CO2 occurs when ground limestone and clay or shale are heated up in a rotating kiln as seen in Figure 1-1. Limestone decarbonises in this process and the carbon is released into the air in the form of carbon dioxide. The other large contributor to CO2 emission is the use of fuels to reach the kiln processing temperatures. OPC production is responsible for 5-8% of all man-made CO2 emissions across the globe (CORDIS, 2018). There are many attempts to reduce the CO2 impact of concretes containing OPC, such as the usage of alternative fuels in the clinker production (Chatziaras, 2014), and reducing the contribution of OPC in concretes by using cement-like materials such as blast furnace slag, fly ash and silica fumes as supplementary cementitious materials in blended Portland cements.

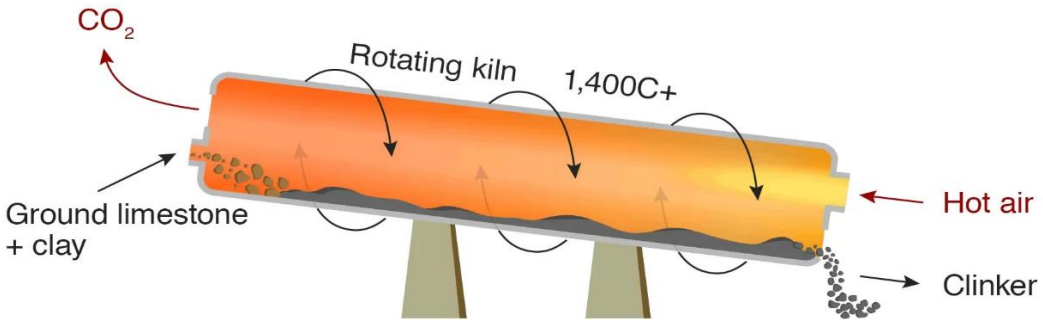

Figure 1-1: Typical kiln processing of raw materials into cement clinker (Lucy Rodgers, 2018)

1.2 Geopolymer concrete introduction, problem statement

Supplementary cementitious materials used in OPC-based cements can instead be used in combination with an alkaline medium to create a cementitious material for making a concrete without the use of OPC. These are referred to as alkali-activated materials (AAM), or in a wider term: geopolymer cement. Aluminosilicate precursor reacts with alkaline activators to create a 2-part binder system. By omitting OPC completely in this geopolymer cement, geopolymer concrete can be created with the same basic formulation as normal concretes: binder, water and aggregates, but with a much lower CO2 emission due to this omission. However, differences in material properties

compared to OPC-based concretes and lack of standards hold geopolymer concretes back from widespread use in structural applications. Major differences include the early age shrinkage and creep, and the effects of drying on the elastic modulus (E-modulus).

In recent years, as the environmental aspect of building materials became much more important, geopolymer concretes saw a rise in applications. There are standards in Australia for example, where VicRoads, the state roads authority for the state of Victoria amended existing standards for pavements, underground storm water drains, drainage pits and wire rope safety barriers among other concrete works to include geopolymer concrete (Andrews-Phaedonos, 2014). However, to further diversify the use of geopolymer concretes in larger scale applications and eventually develop new standards for AAM/geopolymer concretes, more research is needed in this field. It is particularly tricky, as different locations in the world will have different amount of natural materials, precursors and alkaline activators available to them. Each precursor needs the correct activator, or a combination of activators to be sourced. There is currently limited information available for methodologies regarding the pairing of precursors to activators, so most of the development in this area has been achieved through testing. (Provis, 2018)

One of these developments is the geopolymer mixture developed at TU Delft. This is a self-compacting geopolymer concrete (SCGC) developed at the TU Delft Microlab with a strength of C45/55. This mixture is to be applied in a geopolymer concrete structure in a larger project. The geopolymer concrete structure to be investigated is a planned bridge named the “Kowebrege”, in Metslawier: A small town in Friesland, The Netherlands. It will be a solid deck bridge consisting of 6 precast and prestressed girders made of the C45/55 SCGC mixture, topped with a ready-mix geopolymer concrete topping The precast girders are produced by Haitsma Beton and this project is assigned by Provincie Fryslân in the pursuit of a OPC-free concrete solution to replace the road bridge that connects Metslawier to Jouswier. The bridge structure experiences time dependent effects, such as creep, shrinkage, and changes to the elastic modulus, these aspects need to be focused on, as not much is known yet about the behaviour of structures made of geopolymer concrete.

There are already lab tests done by the TU Delft Microlab on C45/55 self-compacting geopolymer concrete specimens. Valuable data is collected regarding several aspects:

1. Mechanical properties, such as compressive strength, tensile splitting strength, change of elastic modulus and Poisson ratio over time, and bond strength (pull-out tests).
2. Volumetric stability properties, including autogenous shrinkage, drying shrinkage, creep and cracking potential by temperature stress and autogenous shrinkage.
3. Durability aspects, such as chloride diffusion resistance, carbonation resistance, and freeze and thaw resistance.

As these lab tests are performed on smaller scale specimens, this data is not entirely applicable to larger structures or structural elements made by this SCGC mixture, such as the aforementioned precast prestressed girder. Properties that are most likely to be different to lab test results when applied in the prestressed girder include but are not limited to: shrinkage, creep, and the elastic modulus (over time).

The interaction of these properties of the SCGC mixture with the effects of prestressing also needs investigation, as these shrinkage and creep effects can result in loss of prestressing force over time. This can have a large impact on the long term behaviour of the eventual structure, as a loss in prestressing forces can lead to cracking and excessive deflection. These serviceability failures affect the durability of the prestressed concrete structure negatively and can pose structural risks. (Abdel-Jaber & Glišić, 2019) Additionally, the bond strength between the SCGC and prestressing tendons

could be different in the girder, compared to the bond strength following lab tests, this can have an effect on the transmission length. It is important to determine the transmission length in a prestressed concrete structural member as it is needed to determine the maximum allowable stresses at the release of the prestressing strands, as well as checking for maximum anchorage capacity of the structural member.

To gain more knowledge regarding (long term) behaviour of prestressed precast geopolymer structural members, structural health monitoring is applied. Structural health monitoring is a process consisting of continuous monitoring of structural parameters to provide accurate information regarding structural condition and performance. (Glišić & Inaudi, 2007). To obtain data for analysis on prestressing losses and behaviour regarding transmission length, sensors are needed that can monitor strain from within the concrete. Since the sensors are to be applied on the inside of concrete, they need to be robust, resistant against a harsh environment, and stable on the long term. For these reasons, FBG fiber optic sensors are chosen.

1.3 FBG fiber optic sensor introduction

The Fiber Bragg grating or FBG is the result of advancements within the fiber optic technology. Since fiber optics were introduced, the field telecommunications has arguably been improved significantly. Fiber optic technology has more applications than providing advancements in communications, and these applications came with the ability to change the core index of refraction inside the optical fiber. The first occurrence of a fiber grating applied inside a fiber optic cable was in 1978 (Hill, Fujii, Johnson, & Kawasaki, 1978). By changing the refraction index of the fiber core in a periodic manner, phase gratings are obtained. This periodic pattern of the refraction index in the fiber has the ability to act as a selective mirror for the optical wavelength by behaving as a series of weak partial reflecting mirrors (Suleman, 2001). As a result of this, the phase grating, or Fiber Bragg grating has the ability to selectively reflect a narrow band of the incoming wavelength spectrum as seen in Figure 1-2, this reflected wavelength is called the Bragg wavelength, and has the following relationship:

$$\lambda_b = 2n_c\Lambda \qquad (1)$$

With: λ_b = reflected wavelength/Bragg wavelength
n_c = average refractive index of the grating
Λ = period of the modulation

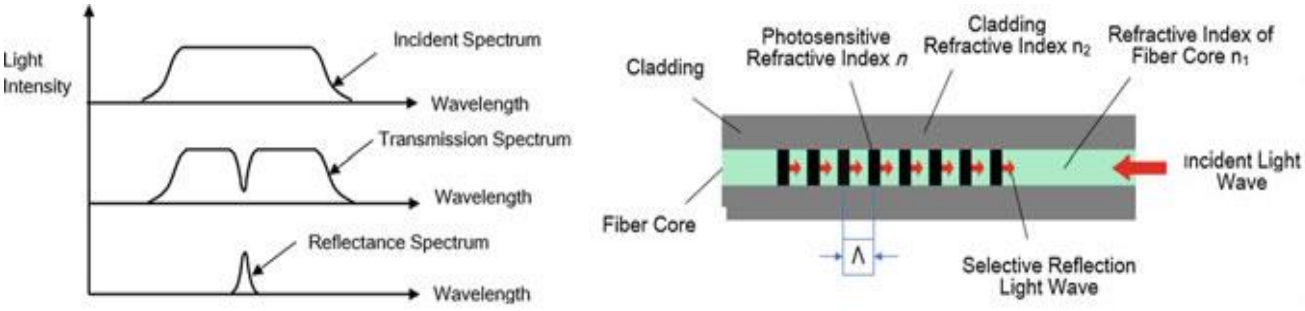

Figure 1-2: The working principle of a FBG (Du, Sun, Li, & Zhang, 2019)

This grating is very sensitive to changes in temperature, and external strains. When exposed to a changes in strain due to thermal expansion/contraction or an external strain, this changes the refractive index of the optical fiber. This change to refractive index in turn changes the Bragg wavelength. The relative shift of the Bragg wavelength can be directly related to the change in temperature and applied mechanical strain in the formula below (Manfred Kreuzer, 2006):

$$\frac{\Delta\lambda}{\lambda_0} = k \times \epsilon_m + \alpha_\delta \times \Delta T \qquad (2)$$

With: $\Delta\lambda$ = measured wavelength shift
λ_0 = base wavelength
k = gauge factor
ϵ_m = mechanical strain
α_δ = change of the refraction index
ΔT = change in temperature in K

This relation is particularly interesting if the change in wavelength due to temperature fluctuations can be compensated for. What is left is a measurement of purely mechanical strain that the FBG experiences. This is the core mechanic for FBG based strain sensors.

1.4 Research objectives and research questions

This research aims to study the usage of FBG fiber optic sensors to gain more information about geopolymer concrete as used in a prestressed structural member. In-situ strain data is to be validated using data from lab tests and analytical models to gain an insight into the structural behaviour of the geopolymer concrete structural member and to study the FBG fiber optic sensor monitoring setup.

The main question for this research is as follows:

How can FBG fiber optic sensors be used to monitor and assess the structural behaviour of a geopolymer concrete structural member?

The main question can be divided into sub questions:

- How can the effects of (autogenous and drying) shrinkage on the precast girders be determined from the measurements?
- This shrinkage has an effect of reducing the prestressing force in the rebar together with the creep strain, can this be quantified using the optic fiber measurements?
- Does geopolymer concrete have the same transmission length as OPC-based concretes and can this be determined using the specifically placed sensors?
- How do the geopolymer concrete structural elements behave during (destructive) testing according to FBG measurements, and is this behaviour according to expectations as derived from simple analytical prediction methods ?

1.4.1 Methodology

FBG fiber optic sensors are applied in precast prestressed geopolymer concrete girders by using integrated sensors in steel rebar. These steel rebars are located above the prestressing strands to gather data relevant to prestressing, transmission length, and cracking behaviour. The geopolymer concrete mixture used in the girder is based on the SCGC mixture mentioned in the introduction.

Raw strain data gathered from the FBG sensors during curing of the girders is processed and analysed to check for abnormalities to evaluate the reliability of the strain measurements. This is done by comparing the results to analytical models, and referencing laboratory tests performed on samples using the same mixture, as performed by the Microlab (Faculty of Civil Engineering & Geosciences, Delft University of Technology)

Strain data during curing is used to approximate prestressing losses based on shrinkage and creep. This has been performed by using Eurocode 1992-1-1, formula 5.46. Eurocode 1992-1-1 methods regarding transmission length are applied to compare with the results of FBG measurements that are aimed to detect the apparent transmission length in the prestressed girder.

A geopolymer concrete topping is cast after sufficient curing of the precast girders to form two separate beams and a mock-deck consisting of three girders with the topping. The beams are to be tested in a flexural test and a shear test respectively, after sufficient curing of the topping. FBG strain data from these tests is collected and evaluated using analytical methods.

For the slab/mock-deck, after curing, it is subject to a cyclic load test, before being tested in two separate occasions for a point load in a critical position. Data collected from FBGs during these tests are compared to analytical models and measurements from LVDTs to verify data collected by FBG sensors, and to gain an insight into the behaviour of the slab.

1.5 Document outline

Chapter 2 starts with a short literature study on material properties of geopolymer concrete relevant to this study, general behaviour of prestressed concrete, and interaction of rebar-integrated FBG fiber optic sensors with (cracked) concrete. In Chapter 3, the entire experimental program is explained, this includes the girder properties, casting operations, prestressing and reinforcement setups. The integration of the FBG sensors is described, with details on calibration and locations of the FBGs inside the girders. Finally, the test setups are shown. Chapter 4 embodies measurement results and analyses, starting with an analysis on prestressing losses due to time-dependent factors using strain data measured by the FBGs. After this, the prestressing transmission length analysis using data from FBGs is presented, before analyses of data gathered during the flexural test, shear test and mock-deck tests are shown. In Chapter 5, the results and observations during the project are discussed, followed by conclusions drawn regarding the use of these rebar integrated FBGs, and the analyses resulting from the gathered data. Discussions and conclusions of the analyses are summarized and expanded on. Finally, recommendations are proposed for usage of these FBG sensors and further research.

2 Literature study

2.1 Introduction

This chapter provides insights on several material properties of geopolymer concretes and how they differ from conventional concretes based on OPC, as well as possible interactions of FBG fiber optic sensors with concrete. This literature study aims to gather more knowledge, relevant to the research objectives, in material properties that are different in geopolymer concretes, compared to OPC-based concretes, and their effects on structural performance. Existing literature and experimental studies are used to gain an insight on these material properties, and their possible impact on structural performance. After this, the possible interactions of applying FBG fiber optic sensors inside concrete is investigated.

2.2 Shrinkage and creep effects of concrete, and geopolymer concretes

Effects of shrinkage and creep on structures made of regular concrete are well documented, as research and experience has been accumulating over the years. This information can still be useful, even when the materials in geopolymer concrete are different. The fundamental effects of shrinkage and creep are still present in geopolymer concrete.

Shrinkage is a gradual process mainly caused by loss of water during the drying of concrete over time, this is called drying shrinkage. The exposed surfaces will experience this first, and then the drying will go further inwards of the concrete. The free water loss happens first, this causes little or no shrinkage at all. After that, the adsorbed water is removed and this will have an effect on the shrinkage. Several factors contribute to early age moisture loss, and thus, drying shrinkage of concretes, such as the size of the specimen, the shape of the specimen, ambient temperature, the humidity, the water-to-binder ratio. (Neville, 2011). These factors are also applicable to geopolymer concrete mixtures. And since high early age drying shrinkage is one of the drawbacks of geopolymer concretes (Deb, Nath, & Sarker, 2015), more data of drying shrinkage and the used curing method is helpful in expanding the practical uses of geopolymer concrete mixtures.

Another type of shrinkage in geopolymer concrete that will differ from OPC concrete is autogenous shrinkage. Autogenous shrinkage is the volume change of concrete without any moisture transferred to the environment. This is caused by the chemical reactions of the concrete and will occur mostly in the early ages. The products of the reactions have less volume than the reagents, resulting in shrinkage. Several factors that contribute to autogenous shrinkage are including, but not limited to: aggregate properties, curing environment, water content, binder materials (Idorn, 1982) (Collins & Sanjayan, 1999). Research shows that alkali-activated fly ash-slag pastes, a form of geopolymer, exhibits a very high amount of autogenous shrinkage when compared to shrinkage of pastes made with OPC or blast furnace slag cement pastes (Guohao Fang, 2018) (Y. Ma, 2015). When the contraction and warping of the concrete is not constrained (statically determinate), deformations will still occur, but no stresses will occur due to the free deformation.

As for creep, the main phenomenon to be investigated is the effects of creep on a prestressing in a precast beam. Creep is the deformation of a material under a constant load, and prestressing introduces this constant load on the concrete via the pre-tensioned steel bars. Since prestressing introduces compression stresses into the concrete, the expectation is that creep causes a reduction in the prestressing force, just like in OPC-based concretes. A lower amount of creep strains is reported in a study on a fly ash-based geopolymer concrete (Hardjito, Wallah, Sumajouw, & Rangan, 2004).

This contrasts with the higher creep observed in a study on slag-based geopolymer concrete (Collins & Sanjayan, 1999).

As the creep and shrinkage behaviour is different per geopolymer concrete mixture, and even dependent on the curing method and environment, formulas and prediction methods cannot be relied on. The creep and shrinkage values have to be experimentally obtained. In-situ FBG fiber optic sensors can be used to determine the strain (over time) in the prestressed SCGC structural member in a real world setting. This data can then be evaluated by comparing the results to tests performed on smaller scale specimens in a laboratory setting. This is important because shortening of the concrete due to shrinkage effects also reduces the prestressing force and when this is combined with creep, the prestressing effects of elastic tendons can be reduced by 5% up to 30% in regular concrete(Hubert Rüsch, 1983). Testing for creep is important, as errors in prediction of creep (and shrinkage) effects can lead to excessive deflections in the bridge structure (Z. P. Bažant, 2017).

2.3 Elastic modulus

A significant difference between OPC concretes and geopolymer concretes is the elastic modulus, this is resistance of a material to being deformed elastically when a stress is applied. Research from Neupane et al. (Neupane, Bajewa, Shrestha, Chalmers, & Sleep, 2014), and Loya et al. (Diaz-Loya, Allouche, & Vaidya, 2011) found that the relationship between E-modulus and compressive strength in fly ash-based geopolymer concrete is similar to OPC-based concretes. Wardhono et al. (Wardhono, Gunasekara, Law, & Setunge, 2017) found that the alkali activated slag geopolymer concrete shows a drastic decrease of E-modulus over time. For the SCGC mixture in this study, laboratory tests from the TU Delft Microlab has shown that this geopolymer concrete exhibits a decrease in elastic modulus when subjected to drying conditions after curing. (Zhang & Ye, 2021)

The behaviour of the tested samples is known. However, in a larger structure e.g. these precast prestressed girders, depending on the curing method as well, will have a more complicated E-modulus development over time. This is further complicated by the geometry of the girder. As concrete closer to the surface will experience the effects of drying quicker than concrete in the core of the girder. When the elastic modulus decreases with the same amount of strain, the stress will decrease too. This is especially important, because prestressing is applied in the studied beams. Furthermore, the topping of the girder consists of a different type of concrete than the precast girder. The details of this ready-mix geopolymer concrete are undisclosed by the provider and material properties including the E-modulus have to be experimentally obtained. When the topping concrete has a different E-modulus than the precast girders, this has an effect on the overall behaviour of the structural elements and needs to be taken into account. As the FBGs are to be applied internally, the aim is to use the sensors to obtain strain measurements to analyse the apparent E-modulus in the core of the girder.

2.4 Prestressing, transmission length

The effects of shrinkage and creep have a negative effect on prestressed structures due to the reduction of strain, caused by concrete deformation. In this section, prestressing and transmission length is shortly explained. Prestressing is achieved by applying tension to steel strands or cables, releasing these on concrete result in a compressive stress to areas of the concrete cross section. This additional compressive stress is aimed to combat the effect of tensile stresses. As concrete is weak in tension, prestressing is often used in concrete structures. For this precast girder type, it is done via pre-tensioning internally, with the use of bond between steel and concrete. Other types of concrete

prestressing exist: External prestressing is usually performed without the use of bond, and there is also internal prestressing via post-tensioning, which can be done with or without bond. These different types of prestressing are outside of the area of interest and will not be discussed.

Internal prestressing is applied by tensioning up steel prestressing strands in a prestressing bed before the concrete is cast. The concrete is allowed to develop sufficient strength, before the tendons are released. The tendons transfer their forces solely by connection to the concrete: bond. This is also the limiting factor, as only a certain amount of stress can be transferred from the strand surface to the concrete per meter of prestressing strand. The distance from the edge of the girder that is needed for the full transfer of prestressing forces to the concrete cross section is called the transmission length. The transfer of forces is established by friction and adhesion only, as the steel strands do not have ribbed surfaces, unlike the conventional steel rebar. For this friction to occur, lateral stresses between steel and concrete are needed. In the transmission length, a so called “push-in” situation occurs. The prestressing strand tries to return to its unstressed state, but the concrete around it prevents that from happening. The counteraction of this expansion generates lateral pressure. This entire process is known as the Hoyer effect (Hoyer & Friedrich, 1939).

The bond strength of the tendons in pre-tensioning can be divided into three parts, according to a model as seen in Figure 2-1 (Nitsch, 2001): A constant part caused by basic friction, a part based on the Hoyer effect that increases with the prestressing force, and a part that is dependent on the amount of slip, and independent of the amount of prestressing. For steel strands, this slip effect can be explained by the “lack of fit” that results from a geometry that is not completely uniform (Geßner, 2017). An illustration of this model can be seen in Figure 2-1, where the bond stress is highest near the edge of the girder. This is because the full prestressing force has yet to be transferred to the concrete, causing high lateral pressure from the Hoyer effect. All of the aforementioned contributions to the bond strength are fully active. Moving further from the edge, the amount of prestressing force that has to be transferred decreases, while also decreasing the stresses.

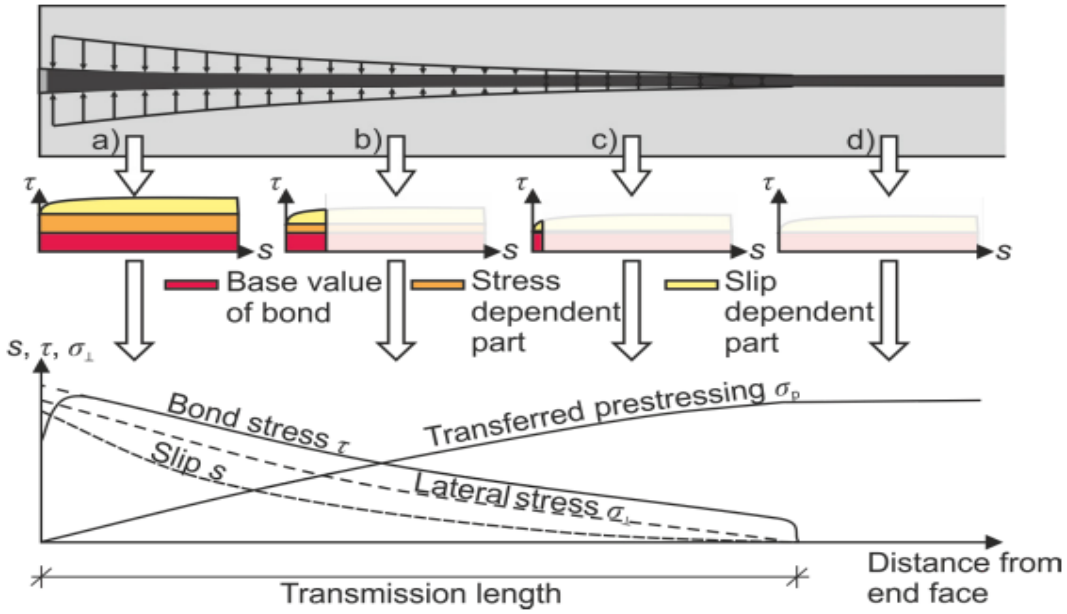

Figure 2-1: The transfer of prestressing and 3 components of bond strength (Geßner, 2017)

Near the end of the transmission length, the bond is mostly comprised of the base value, whereas the slip and lateral stress components are low. The design model used by Eurocode EN 1992-1-1 (Eurocode 2, EC2) for the transmission length, uses an idealised bilinear relationship over which the prestressing force is fully transmitted to the concrete, seen in Figure 2-2.

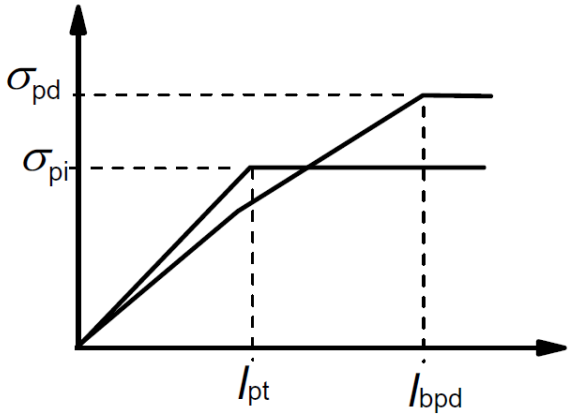

Figure 2-2: Eurocode 2 bilinear relationship for the transmission length lpt, and the total anchorage length lbpd

This assumes that the bond strength is constant, unlike described before, where the bond strength is highest at the edge of the girder and nonlinearly decreasing until the transmission length has been reached. However, this simplification does not differ significantly from measured values and is permissible (Martí-Vargas & Hale, 2013). This bilinear relationship will be used to calculate the transmission length of geopolymer concrete specimens in the uncracked situation, and compared to strain measurements.

Although the Eurocode 2 formulas are intended for use in OPC-based concretes, the comparison between Eurocode 2 predictions and the geopolymer concrete in practice can still give valuable insights regarding the validity of current codes for OPC-based concretes for geopolymer concretes such as this application. The bond strength of geopolymer concretes is generally found to be higher than OPC-based concretes, according to a review of 10 studies encompassing various test methods and constituents. (Mo, Alengaram, & Jumaat, 2016).

As bond strength is directly related to transmission length, the expectation is that the transmission length prediction method from Eurocode 2 calculations is applicable on geopolymer concretes. The comparison of strain monitoring results with Eurocode 2 predictions will give an insight on the apparent transmission length of this SCGC mixture as applied in a prestressed girder.

2.5 FBG fiber optic sensor, embedding into steel rebar

Applying FBG sensors to measure concrete strains come with their challenges. When applying the fiber optic directly inside a concrete girder, by embedding it, measurements can be done accurately. This is because the strain in the concrete will equal the strain in the fiber optic. This is only valid for when the concrete is uncracked. For example, in a concrete rod under tension with fiber optic sensors running through it: when enough tension is applied for a through-crack in the rod, the strain of concrete is infinite at the crack location. The optical fiber running through the crack is restrained by the uncracked concrete, and cannot match the strain of the crack and will therefore break (Faassen, 2021). To avoid the breaking of the fiber optic due to a crack, the fiber optic can be embedded in reinforcement steel. Even if a crack occurs in the concrete, the steel rebar will ensure the crack strain is spread across the steel, protecting the fiber from failing.

The observation from a study by Kaklauskas et al. (Kaklauskas, Sokolov, Ramanauskas, & Jakubovskis, 2019) is that these strain measurements are accurate, when compared to conventional electrical strain gauges that are also embedded in rebar. Compared to electrical strain gauges, the FBG sensors are also found to be less labour intensive and less time-consuming, while providing more measuring points due to the space required to accommodate wiring of the electrical strain gauges.

(Kaklauskas, Sokolov, Ramanauskas, & Jakubovskis, 2019). The embedding of the FBGs was achieved by milling a shallow longitudinal groove in the rebar, putting the fiber through it, and filled with an epoxy adhesive. (See Figure 2-3)

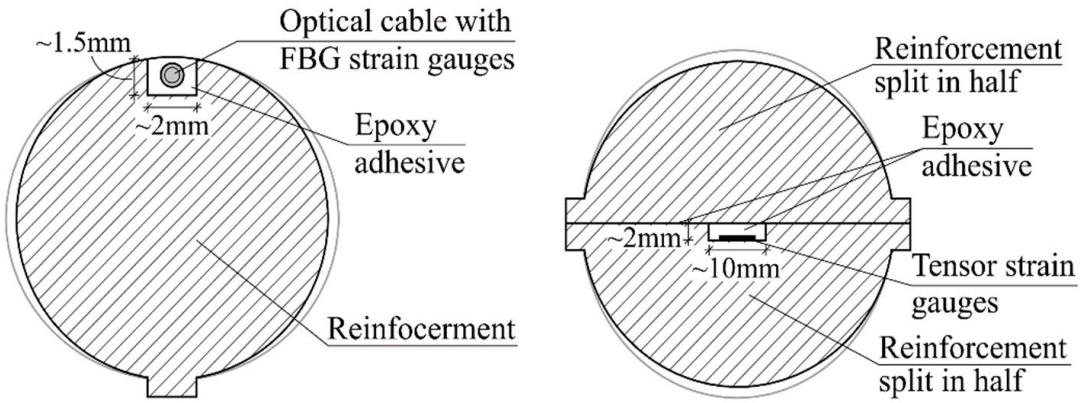

Figure 2-3: Experimental setup embedding FBGs and tensor strain gauges in 2 rebars (Kaklauskas, Sokolov, Ramanauskas, & Jakubovskis, 2019)

This achieves a bond between the FBGs and the rebar while giving sufficient protection to the sensors. This results in a measurement setup that can monitor occurring strains inside concrete as the strain in the rebar is equal to strain in the concrete.

This research will contribute to ongoing research on the application of the SCGC mixture in a precast prestressed structural element. The implementation of FBG fiber optic sensors to measure in-situ strain is also investigated.

For this, FBG fiber optic sensors are integrated into steel rebar, to be inserted in the centre of 4 precast prestressed geopolymer concrete girders to study their behaviour. The girders experience time dependent effects, such as creep, shrinkage, and changes to the elastic modulus during curing, and the FBG sensors inside the girder will provide data to analyse the behaviour, including the transmission length. A geopolymer concrete topping is added to the girders to form structural elements that are subject to load tests. Measurements during the load tests give an insight into the behaviour of these elements. This is to gain knowledge before the geopolymer concrete girders are applied in a planned real-life bridge structure.

2.6 Interaction of FBG sensors with uncracked and cracked concrete

Embedding the sensors into steel rebar and applying this inside concrete has complications when cracks start to occur. The assumption that the measured strains are equal to the strain in the concrete only works until the concrete starts cracking due to tension occurring that exceeds the tensile strength of concrete. The tensile stress is too large for the concrete and the concrete cracks. The problem is when this crack is near, or exactly on the spot of the rebar containing sensors. As explained in the section before, the steel bar spreads the strain across the steel, preventing the optic fiber from breaking locally. This also distorts the measurements, as the sensors are measuring the strain of the steel, rather than the strain in concrete.

Using a simple tensile chord model, this concept can be explained. This model consists of a concrete chord element reinforced with a single steel rebar of diameter Ø in the middle seen in Figure 2-4. Applied to the ends of this element is a tensile force. This force causes a stress in the cross section. As long as the tensile stress of the concrete σ_c is below the tensile strength f_{ct} of the

concrete, this results in equal strain in the concrete and steel ($\epsilon_c = \epsilon_s$), but not an equal amount of stress (σ) due to the difference of E-modulus of concrete (E_c) and steel (E_s):

$$\epsilon_s = \frac{\sigma_s}{E_s}, \quad \epsilon_c = \frac{\sigma_c}{E_c} \tag{3}$$

Figure 2-4: Tensile chord model where no cracking is present, concrete strain is equal to steel strain

When the tensile strength of the concrete is reached, the first crack occurs. At the crack location, all of the tensile force is transferred by the steel rebar, as the concrete is unable to transfer tensile forces. In the vicinity of the crack, the tensile forces in the steel is distributed back to the concrete via the surface of the steel rebar that is in contact with the concrete. This distribution is limited by the bond strength, which for ordinary ribbed steel bars is assumed as $\tau_{b0} = 2f_{ct}$ prior to yielding (Sigrist & Marti, 1994). When the concrete tensile strength is reached due to the tensile stress distribution from steel to concrete, the next crack occurs, this results in a fully developed crack pattern in the tensile chord model as seen in Figure 2-5.

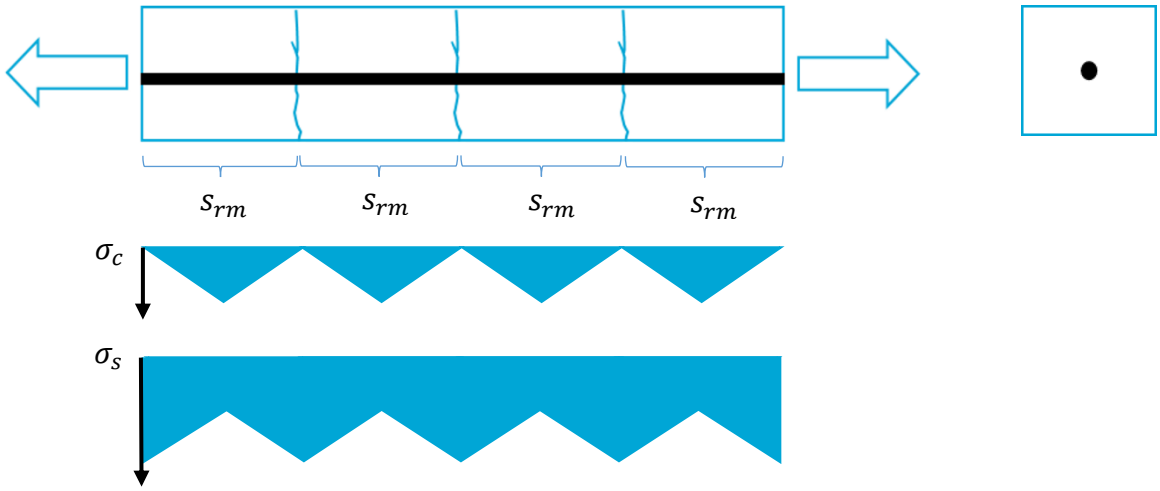

Figure 2-5: Tensile chord model, tensile stress is above concrete tensile strength, through cracks occur and a crack spacing is visible along with the stress in the concrete and steel

The crack spacing s_{rm} in a fully developed crack pattern is based on a number of factors (Marti, Alvarez, Kaufmann, & Sigrist, 1998):

$$s_{rm} = \lambda s_{rm0} \quad (4)$$

$$s_{rm0} = \frac{\emptyset\, f_{ct}(1-\rho)}{2\,\tau_{b0}\,\rho} \quad (5)$$

With: $0.5 \leq \lambda \leq 1$
$\rho = 0.25\pi\emptyset^2/A_c$

If this steel rebar contains FBG fiber optic sensors, the sensors will measure the local steel strain at discrete points along the rebar. When in the vicinity of a crack, the FBG will return data that shows a higher strain, related to stress as seen in equation 3. The amount of measured strain depends on the distance between the sensor and the crack, depending on the stress remaining in the steel that has not been transferred to concrete via bond stress. If the spacing of the FBG sensors is smaller than the crack spacing, two adjacent sensors can be affected by the same crack. This is because the distance that is needed to distribute tensile stresses from the steel to concrete is larger than the FBG spacing.

On the other hand, if the spacing of the FBG sensors is larger than the crack spacing, one sensor is only influenced by one nearby crack. This is valid for the crack spacing in the tensile chord model, but also applicable on crack spacing during a 4-point bending text on a girder for example. In reality though, the crack spacing during such a test is not consistent. This inconsistency needs to be taken in account when determining crack proximity using FBG sensors.

2.7 Conclusions

Experimental studies suggest that a few material properties of geopolymer concretes are similar to OPC-based concretes, such as the elastic modulus and the bond strength. However, most studies report differences of the amount of shrinkage, creep and elastic modulus, also depending on the composition of the used geopolymer concrete mixture. As it is evident that the material properties of geopolymer concrete differ per mixture, it is important to gather as much information on the material properties of the used SCGC mixture. As there are laboratory tests performed on samples of this mixture, more data is needed on the properties of the concrete when applied in a larger scale structural element, which this study aims to aid in.

For this, the interaction of FBGs as applied in concretes is shortly investigated in the latter portion of the literature study. It is evident that the direct application of FBG fiber optic sensors in concrete is not feasible due to the possible failure in cracked concrete. FBG fiber optic sensors integrated in steel rebar is shown to have remedied this issue, while exhibiting similar levels of performance as conventional strain sensors. This application is to be further analysed in this study to gain knowledge into the interaction of rebar-integrated FBG fiber optic sensors as used in a structural element to gain more knowledge about the material properties of the SCGC mixture as used in a real life scale. Potential interactions of the sensors in uncracked and cracked concrete have been investigated by using a simple tensile chord model. This confirms that there should be a significant increase in measured strain in the FBGs, also depending on the proximity of the FBG to a crack, when the tensile stress exceeds the tensile strength of the concrete.

3 Experimental program

The province of Friesland, in the Netherlands is looking to replace an old bridge deck with a new one. The Kowebrêge is a bridge near Jouswier that carries the provincial road N358 across the Zuider Ee or Suderie, a small river in Friesland. The longest span of the new deck will be 7 m. Since the province has ambitions regarding circular economy, and innovation, a new bridge deck based on geopolymer concrete was chosen to replace this old deck. The new bridge deck will consist of a prestressed precast girder based on the self-compacting geopolymer concrete mixture (SCGC) from TU Delft, produced by Haitsma Beton. These girders together with a cast-in-situ ready-mix geopolymer concrete top layer will form the deck.

The SCGC mixture already has seen extensive lab testing before this point, so material properties in that scale are known. The goal of the project is to apply geopolymer concrete on a larger structural scale. To realise this, the properties and behaviour of this SCGC mixture in larger scale specimens in the form of girders and a slab (mock-deck) is studied. Material and structural performance has to be satisfactory, as well as several other factors including the integration of the two different geopolymer concrete mixtures (girder and topping), and the performance of the SCGC mixture when used in a prestressed system.

To gain information that is otherwise difficult to get to, FBG fiber optic sensors are used to determine strain of the concrete in the core of the girder. This data is to be verified and checked using existing data gathered in laboratory tests, and/or analytical models for abnormalities. This data is then used to analyse the effects of prestressing in this SCGC mixture, the change in strain over time and its effects on prestressing forces, and (cracking) behaviour of the specimens during load testing.

A total of 8 prestressed girders type HKO-300 with a length of 7.35 m have been produced at Haitsma Beton, with the prestressing strands released at 2.5 days after casting.

3.1 Specimen description

Four of the produced girders have FBG fiber optic sensors integrated in them, and will be focused on. The girders are cured to ensure the curing condition is an environment with a high percentage of humidity after the prestressing strands are released. This is done by wrapping the girders in a wet burlap cloth and sealed in plastic right after release of prestressing and demoulding. The girders are left to cure in the storage yard at Haitsma, as seen in Figure 3-2. The girders are ready for transport at 14 days after casting, they are transported to Ghent while retaining the curing conditions, where the girders await the date of the casting of the topping. The burlap cloth and plastic seal are removed at ±21 days after casting, this is to prepare the reinforcements of the girders for the casting of the toppings.

The casting of a topping creates a composite beam with a total height of 420 mm, and a width of 1100 mm, see the schematic cross section in Figure 3-3. This creates a cross section where the total concrete area is 453.3 $\times 10^3$ mm^2. The toppings are cast when the girders are 30 days old. The topping is a ready-mix C30/37 geopolymer concrete provided by Cementbouw Mortel B.V. in collaboration with Sqabe and Rumst Recycling. (Matthys, Proia, Sun, Ghorbani, & Krajnovic, 2022). An overview of the four girders and their topping casting moments are summarized in Table 1.

For precast girders specimen 3 and 4, the geometry of the composite beam after the casting of the topping can be seen in the top of Figure 3-3. The precast girders of specimen 1 and 2 are combined with another girder, and concrete topping to form a slab/mock-deck, its dimensions can be seen in a schematic cross section in the bottom of Figure 3-3.

Table 1: Casting dates of girders containing FBG sensors and topping casting dates

	Rebar sensors	Days passed between casting of girder and casting of topping
Specimen 1	Short 1	31
Specimen 2	Long 1	31
Specimen 3	Short 2	31
Specimen 4	Long 2	31

Figure 3-1: Left: Before casting, visible are the reinforcements, the white cable: fiber optic cable.
Right: Casting of the same girder at Haitsma Beton, September 17th

Figure 3-2: Open storage of 2 girders at Haitsma Beton's yard, wrapped in burlap cloth and plastic

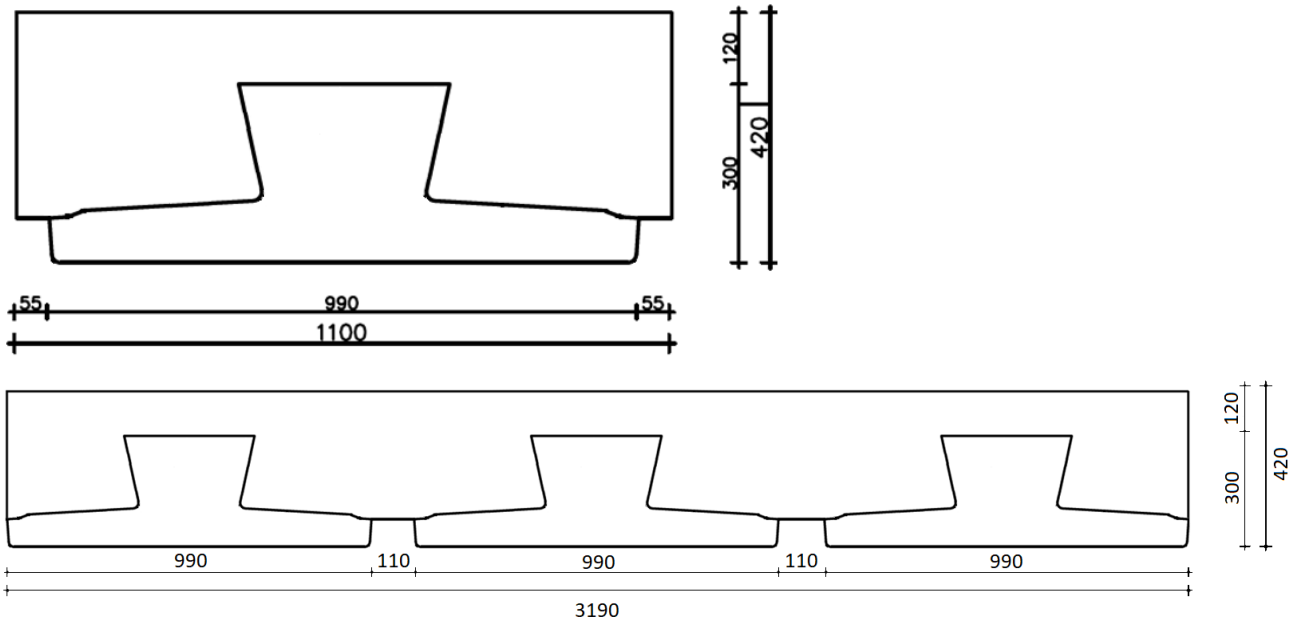

Figure 3-3: Top: Cross section of a composite beam, with the precast girder in the bottom side of the beam, values in mm Bottom: Schematic cross section of the mock-deck comprising of 3 precast girders and a topping, values in mm

Specimen 3 is tested in a 4-point bending test on 15/11/2021, roughly 4 weeks after the casting of the topping. A simple schematic of the 4-point bending test can be seen in Figure 3-4. Specimen 4 is tested in a shear test on 19/11/2021 as seen in Figure 3-5. The loads in both tests are spread over the width of the girder, details of the loading procedure will be discussed in Chapter 3.5.

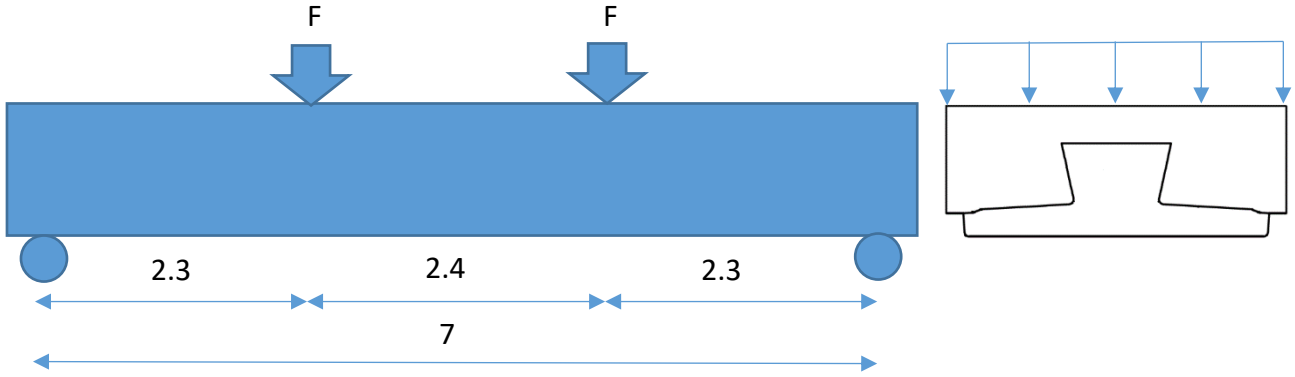

Figure 3-4: Simple schematic of the 4-point bending test (shear test) performed on specimen 3, units in meters

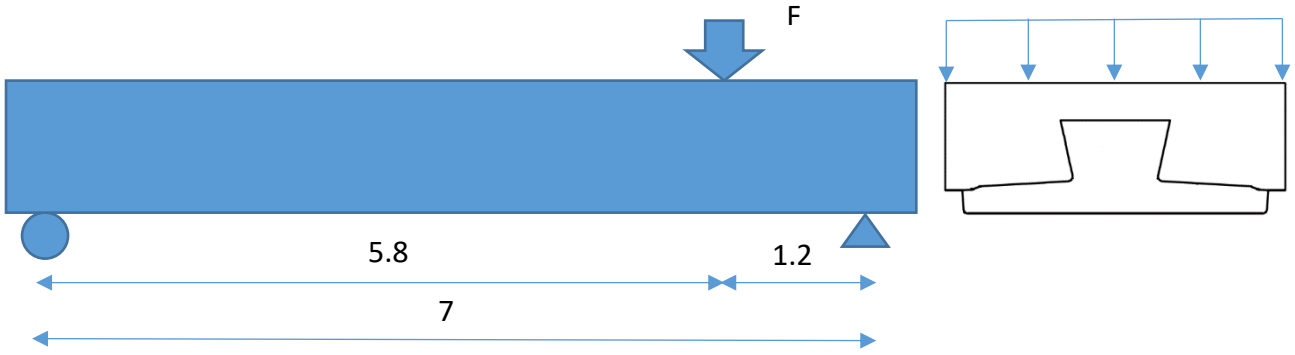

Figure 3-5: Simple schematic of the 3-point bending test (shear test) performed on specimen 4, units in meters

For the mock-deck, a cyclic loading test has been performed by Soete Laboratory of Ghent University. The test started when the topping of the concrete reached an age of 28 days. Cyclic loading between 20 and 200 kN for up to 3 million cycles at a frequency of 3 Hz were applied in the centre of the slab (see appendix B1). The magnitude of this cyclic load test was determined on the heaviest fatigue traffic load model for bridges. After this has been performed, the mock-deck is tested in critical locations on 2 different days. The static load test for a position in the middle (flexural) is performed seven weeks after the topping has been casted, and nine days later for a position in shear. Details regarding this will be shown in Chapter 3.5.

3.2 Reinforcements

3.2.1 Prestressing

The precast girders all have the same design: the prestressed precast HKO-300 girder. This section summarizes the reinforcement setup of the girders and mock-deck. The full technical drawings as supplied by Haitsma Beton are available in Appendix A.

There are a total of 16 prestressing strands used each girder, these are Y1860 7-wire strands with a diameter of 12.9 mm, and an area of 100 mm^2. Four strands are unbonded for the first 1000 mm from the edge of the girder to combat excessive prestressing forces at the edges that could pose a problem. As visible in the same Figure 3-6, each of the strands will be prestressed to an initial force of 140 kN.

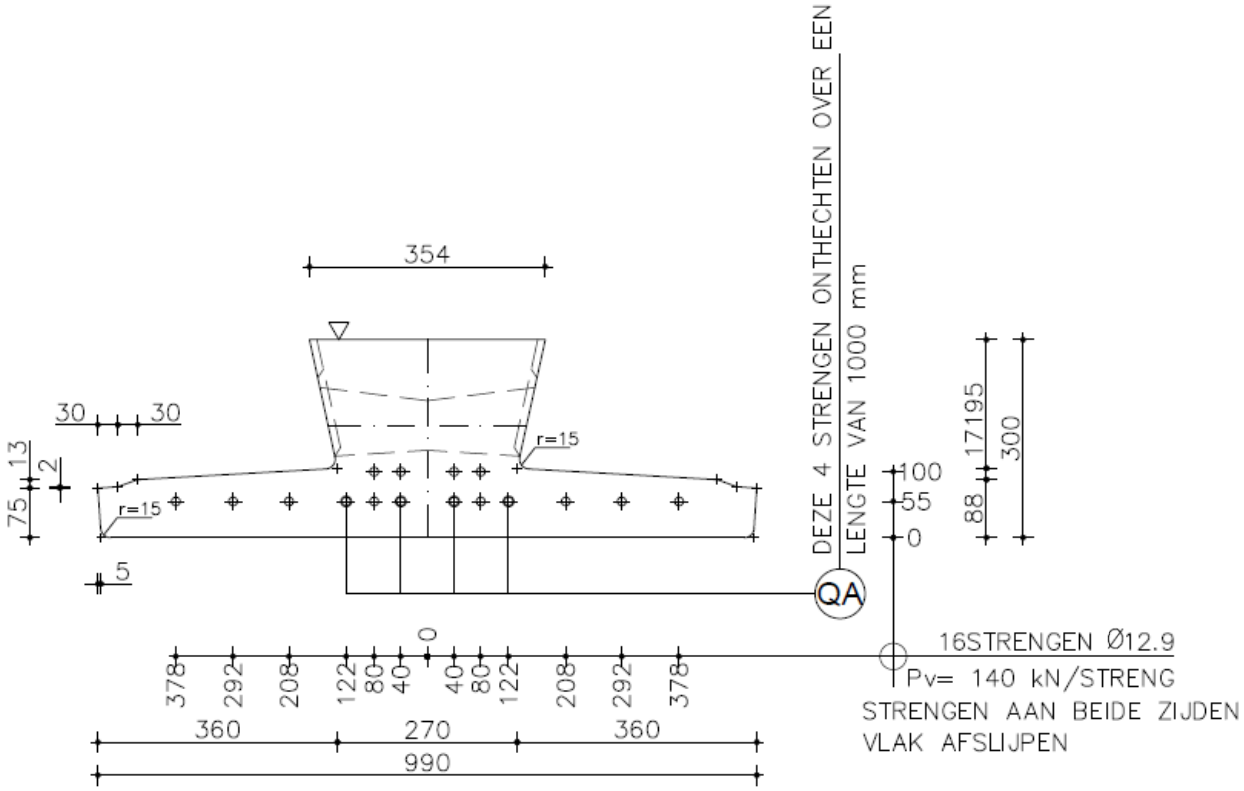

Figure 3-6: Schematic cross section and prestressing layout of an HKO-300 prestressed geopolymer concrete girder

3.2.2 Reinforcements in precast girder

B500B steel reinforcement bars have been applied as shear reinforcement and longitudinal reinforcements. The six 10 mm diameter longitudinal reinforcement bars are marked in Figure 3-7, as well as the 8 mm stirrups.

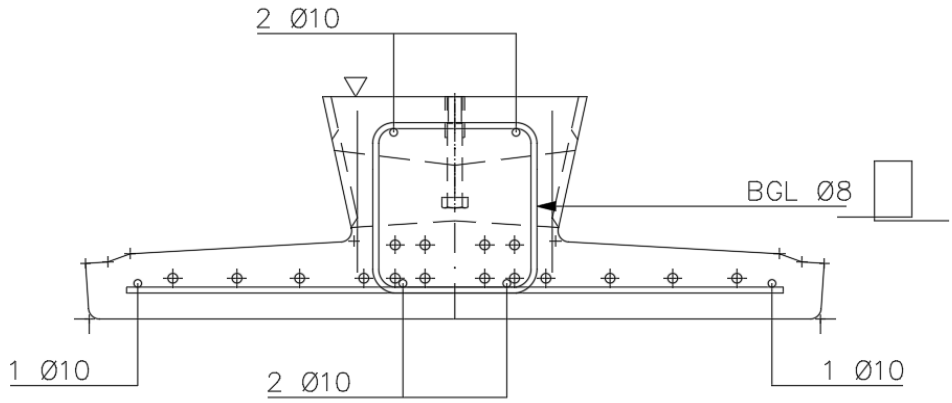

Figure 3-7: Longitudinal rebar and stirrup locations in the girder cross section

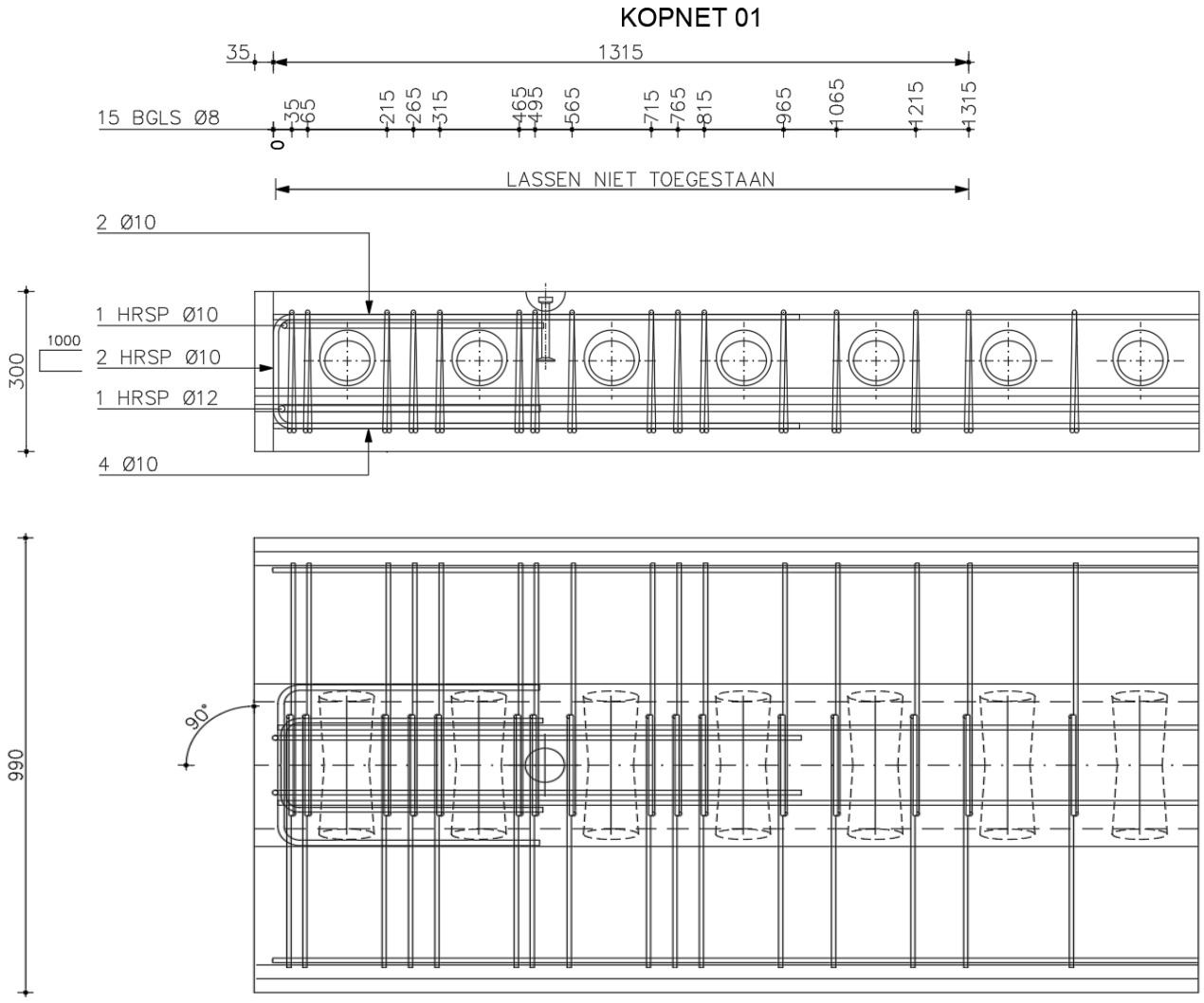

Figure 3-8: Side view, and top view of the edge of the girder, showing stirrup placements, and gaps with a spacing of 250 mm

The stirrup spacing is denser at the edges of the beam, where shear forces are expected to be higher. The stirrup spacing at the edge can be seen in Figure 3-8. In the midspan, 18 stirrups are spaced within 4250 mm with a spacing of 250 mm each. These are the same spacing as the gaps as seen in the side view. These are present to allow for reinforcements of the top layer to pass through. These will impact initial FBG measurements as well, as discussed later. Four additional U-shaped stirrups, are added to the edge of the girder.

3.2.3 Reinforcements in topping

As mentioned before, 21 days after the girder has been casted, the reinforcements are prepared for the casting of the topping layer. The details of a typical cross section showing the stirrups and longitudinal bars of the concrete topping can be seen in Figure 3-9. A side view of half of a composite girder showing angled U-shaped stirrups going through the 250 mm spaced gaps can be seen in Figure 3-10. A more detailed version can be found in the appendix, complete with a top view. As for the reinforcements in the topping in the mock-deck, these will not fit on a single page with all its details, therefore the details regarding these reinforcements can be seen in the appendix.

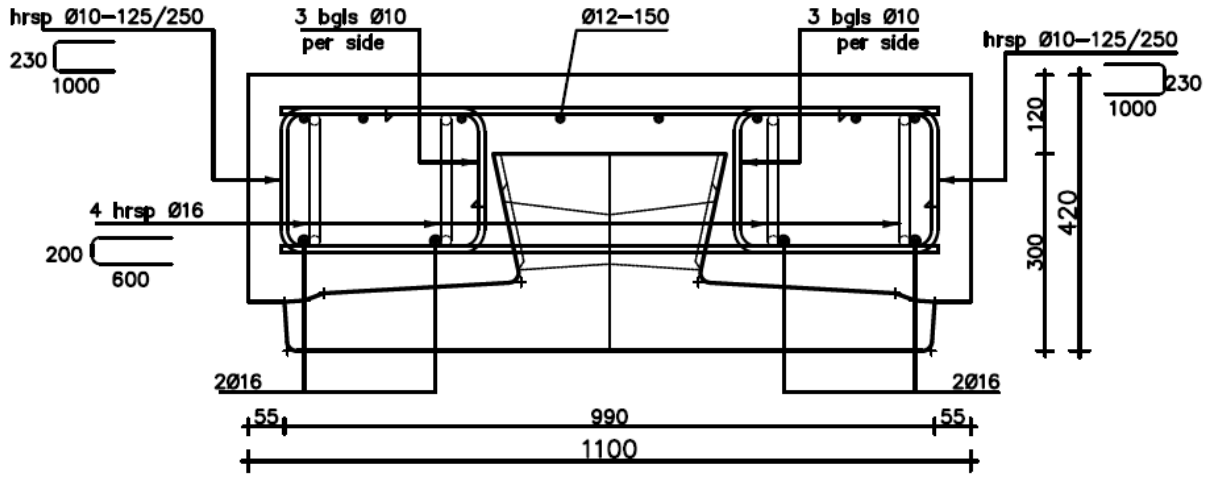

Figure 3-9: Reinforcement setup in the topping of the composite girder in a cross section at 925 mm from the edge.

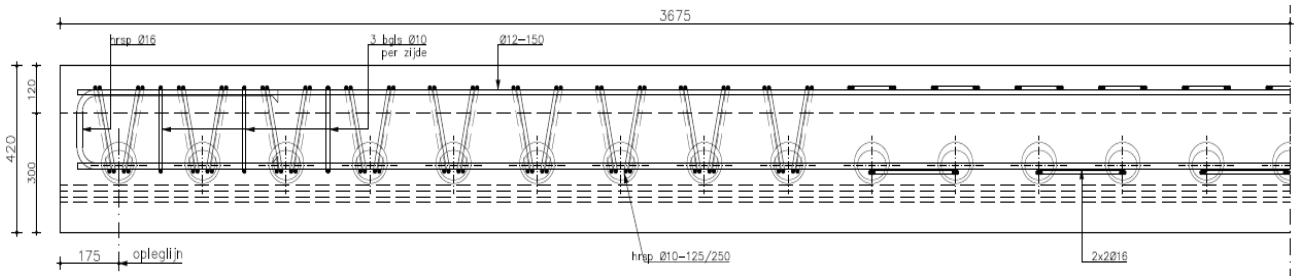

Figure 3-10: Schematic side view of the composite girder and the visible angled stirrups passing through the gaps in the precast girder

The mock-deck/slab topping has been cast 31 days after the girders are casted. The orientation of the slab in the Magnel lab will now be referred to as either the ‘’Door” side of the “Clock” side, see the pictures in Figure 3-11. In these pictures, the topping has just been cast, as visible by the condition of the topping, as well as the formwork and the clamps.

Figure 3-11: Pictures taken after the topping of the mock-deck has been cast, showing the two named sides of the slab

After the casting has been performed, all specimens were covered with wet burlaps and wrapped in plastic sheets. The formwork is removed 24 hours after casting. The testing of the girders is planned in such a way that the age of the topping concrete is close to 28 days (4 weeks). When needed, the burlaps and plastic cover was removed a couple days before testing for preparation of the testing setups. The white cables sticking out of the tubes are the fiber optic cables. The relevant material properties of the geopolymer concrete will be discussed in the next section.

3.3 Material properties resulting from laboratory tests

As mentioned in Chapter 1.2, several tests on this SCGC mixture have been performed at the TU Delft Microlab. The results of these tests are used in analytical methods to compare with results from FBG monitoring. For analysing prestressing losses over time, laboratory tests performed on creep, autogenous shrinkage and drying shrinkage are applied. Early results from lab tests on autogenous shrinkage can be seen in the figure below, where time is represented in days:

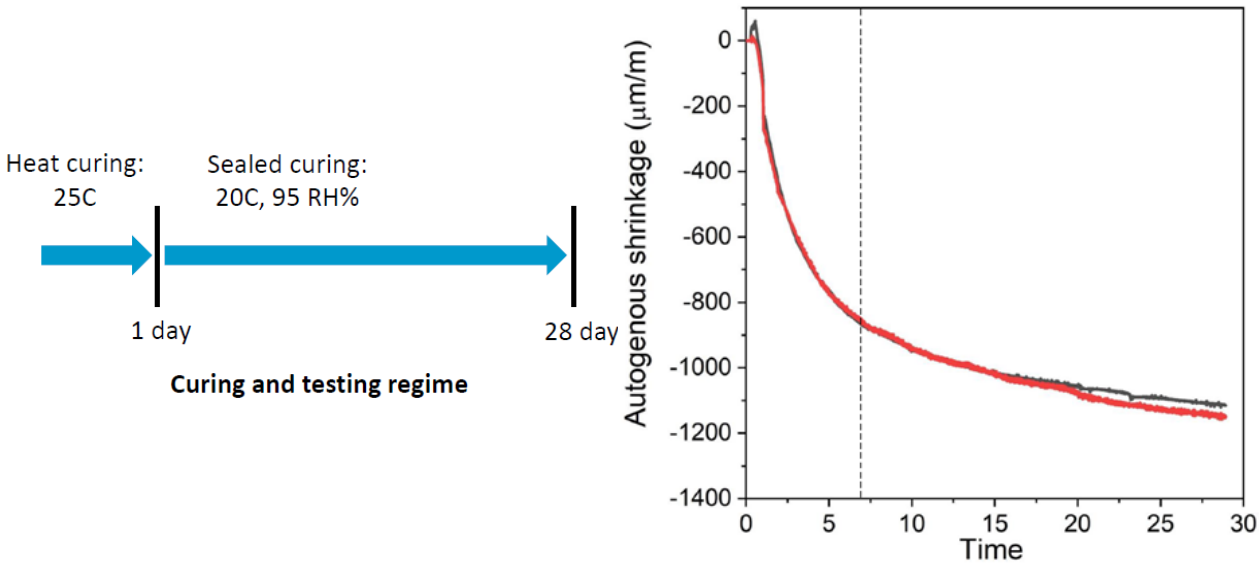

Figure 3-12: Autogenous shrinkage test performed on specimen made of the TU Delft SCGC mixture (Zhang & Ye, 2021)

As the prestressing is released 2.5 days after casting, a major amount of autogenous shrinkage will not affect the loss of prestressing force over time. There is still a significant amount of autogenous shrinkage that is expected to be detrimental to the prestressing forces.

For creep, a sample is subject to 17 MPa of compressive force during the test. This is to simulate a compressive stress similar to conditions inside the prestressed precast girder, near the prestressing tendons. The load is applied at 3 days after casting, which is also when the measurements start. The creep strain and the strain due to shrinkage are presented in the figure below:

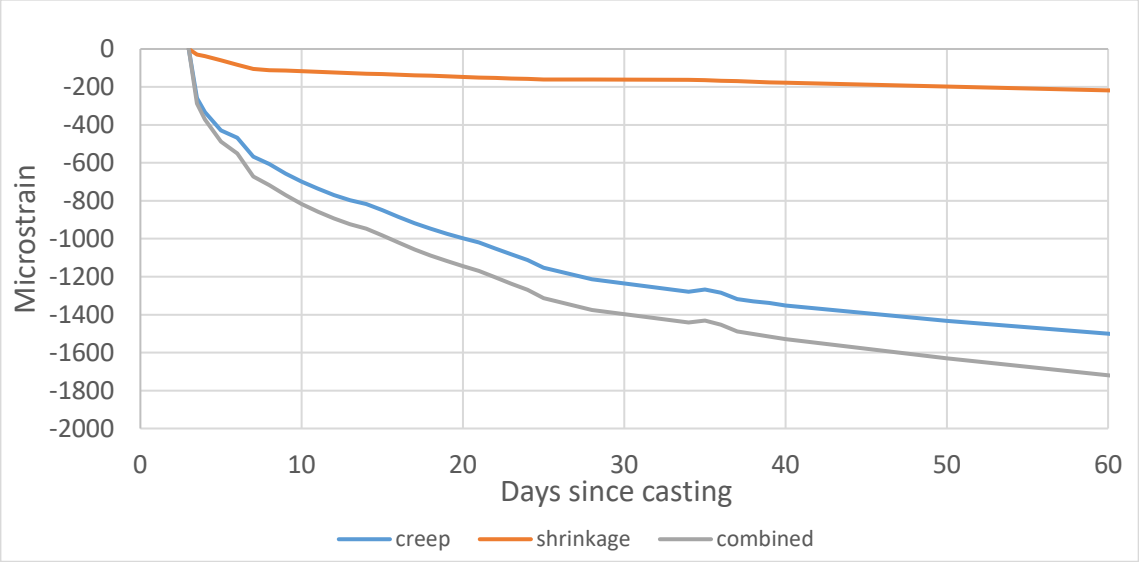

Figure 3-13: Microlab test data on SCGC, first 60 days of shrinkage and creep, tested at 17 MPa

The final material property for analysing prestressing losses over time is the elastic modulus. As mentioned before, the elastic modulus of geopolymer concrete is generally lower than OPC-based concretes. Lab tests have been performed with different curing regimes to show the effect of drying on the elastic modulus of the SCGC samples in Figure 3-14.

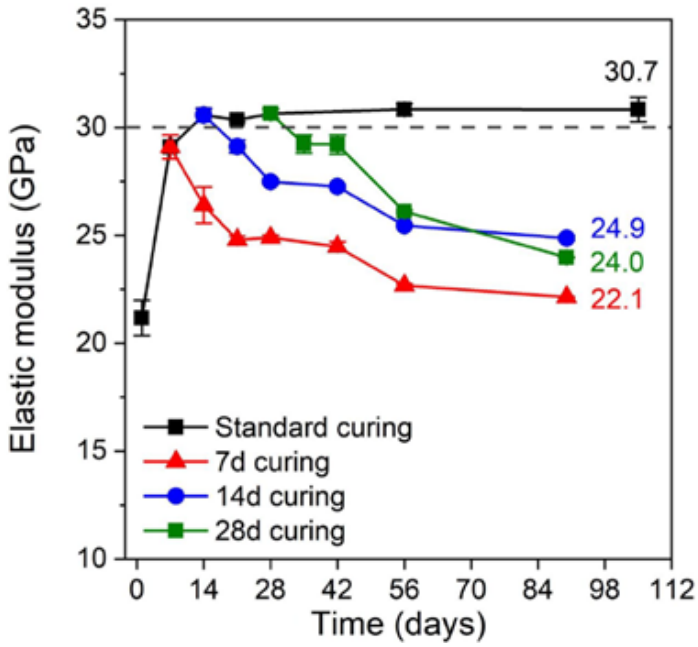

Figure 3-14: Microlab tests done on SCGC mixture regarding E-modulus over time for different curing regimes (Zhang & Ye, 2021)

The elastic modulus of the ready-mix geopolymer concrete that is applied in the topping is also tested using several curing regimes. The elastic modulus of the topping, which is a ready-mix geopolymer concrete (C30/37) is experimentally tested by J.E. Paredes Pineda in a Master Thesis (Pineda, 2022) Prisms of 100x100x400 mm are collected and tested at TU Delft. Plots summarizing the test results are shown in the figure below.

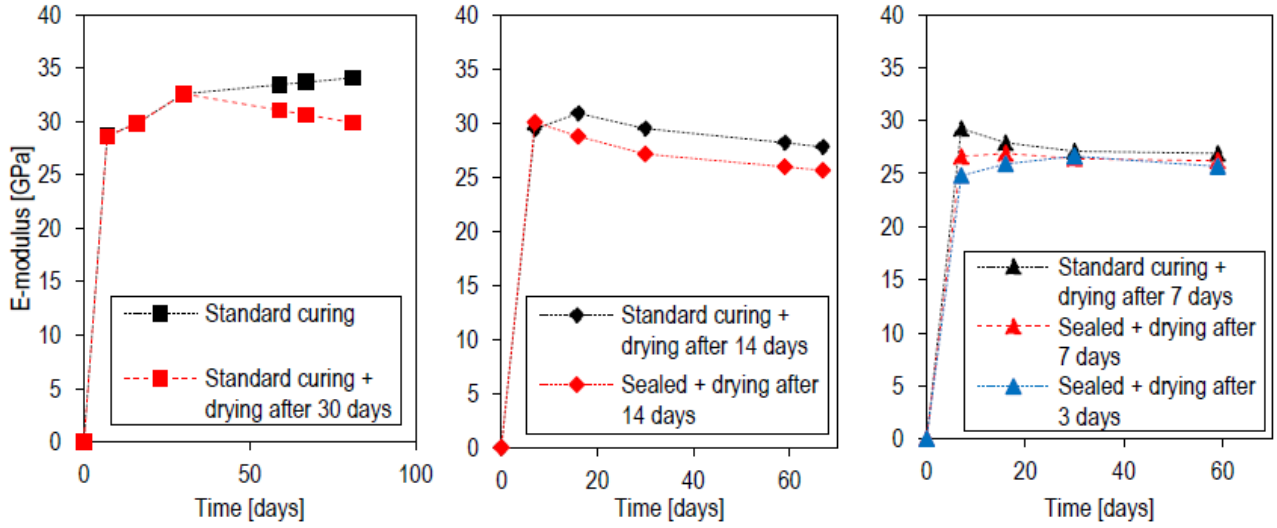

Figure 3-15: E-modulus test results following different curing regimes performed on prisms of ready-mix geopolymer concrete (Pineda, 2022)

The bond strength of the SCGC mixture has been tested using a pull-out test. Samples are tested at 1 day after casting, and 28 days after casting, as seen in the figure below. This data is used to compare with results following the transmission length analysis following Eurocode 2 procedures in Chapter 4.2.

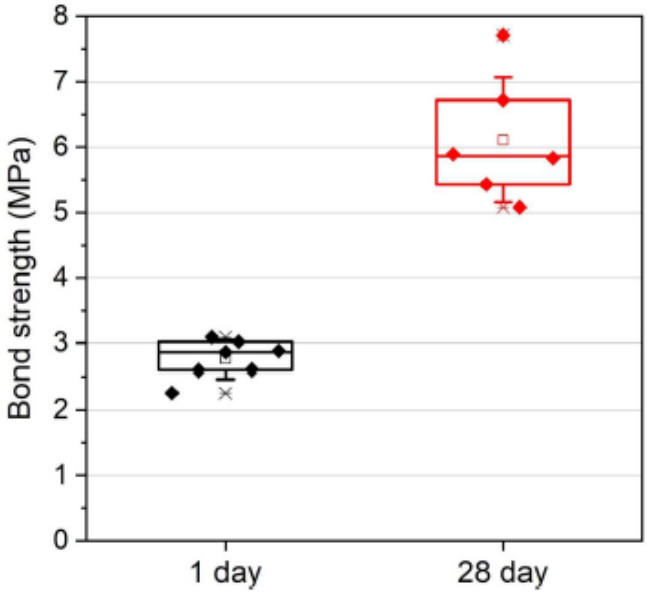

Figure 3-16: Bond strength following pull-out tests (Zhang & Ye, 2021)

3.4 FBG fiber optic sensor instrumentation

3.4.1 General

For gaining more insights in the behaviour of the girders, 4 girders are fitted with a steel rebar with a diameter of 10 mm (Ø10) containing FBG fiber optic sensors. The integration is realised by milling a slot in the rebar, placing the optic fiber sensors and cable in, and filling the slot up with epoxy. These sensors are made of optic fiber (glass) and are encased by plastic, which makes them protected well enough from moisture. The four girders will each undergo experiments, namely: Specimen 1, and 2, two girders with fiber optic sensors will be combined with a third girder and the ready-mix geopolymer concrete topping to create a mock-deck to be subject to cyclic loading, before getting tested in a critical point for bending, and another critical point for shear capacity.
Specimen 3 is to be tested in a 4-point bending test (flexural test)
Specimen 4 is to be tested in a 3-point bending test (shear test)
For this, two different FBG fiber optic sensor integrated rebar setups have been prepared.

First off: a setup consisting of four FBGs inside of a rebar with a length of 1470 mm. This type is labelled as the “Short variant”. A schematic can be seen in Figure 3-17. Specimen 1 and 3 will have 1 rebar of this variant inside of them, The FBG set +rebar inside of specimen 1 and 3 will be referred to as Short 1 and Short 2 respectively from now on.

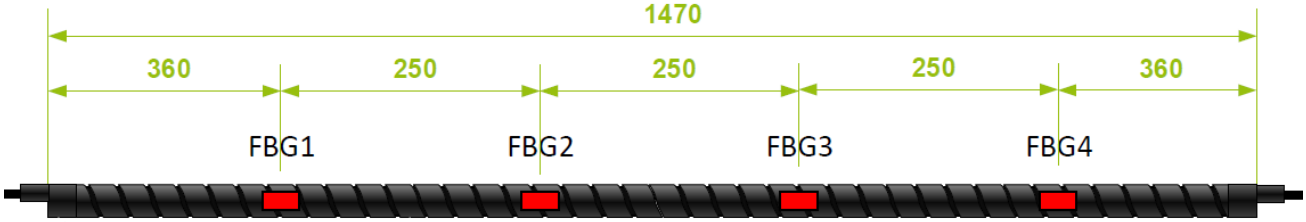

Figure 3-17: Schematic of the shorter variant of the applied rebar-integrated FBG fiber optic sensors

The longer variant FBG fiber optic sensor integrated rebar is a setup that consists of five FBGs inside of a rebar with a length of 1720 mm as seen in Figure 3-18. The only difference is that this variant is 250 mm longer with one more FBG. Specimen 2 and 4 will have this 1 rebar variant inside of them, these will be referred to as Long 1 and Long 2 respectively from now on.

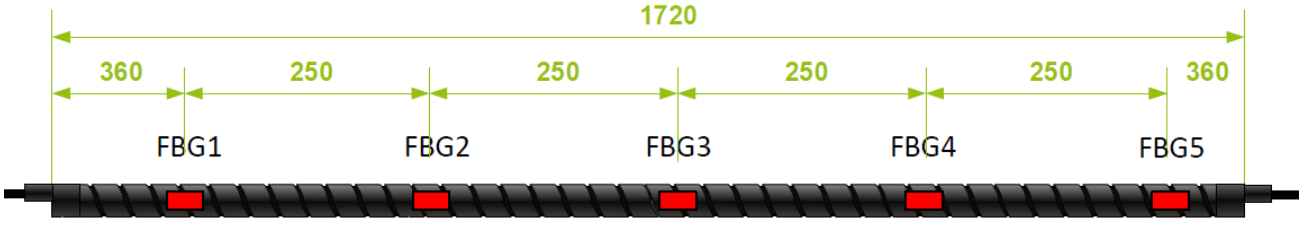

Figure 3-18: Schematic of the longer variant of the applied rebar-integrated FBG fiber optic sensors

Not shown in the schematics are the external temperature sensors. A set of FBGs is accompanied by one temperature sensor. These sensors are located at ±1 m from the edge of a rebar, on the side with the highest numbered FBG (to the right of Figures 3-17 and 3-18). These temperature sensors will be located in the same height of the girder as the rebar. Although the sensor is more than a meter away from the FBGs, the measured temperature should be close to the temperature of the FBGs, as they are both located at the core, at equal distances away from the surface of the girder. The temperature of the material at the core is less easy to sway because of environmental influences.

3.4.2 Calibration, temperature compensation

The calibration of the FBG embedded rebars been done using a laptop with the Femtosense software, as provided by Fugro, and an FBG interrogator device. This device provides the fiber optic sensors with a signal that comprises of a wavelength spectrum. The interrogator can detect wavelengths, as reflected by the FBGs, and log these with a frequency of up to 250 measurements per second. The reflected wavelengths are logged, and the strain at the location of each FBG is calculated using the strain equation, a derivation from the formula as seen in equation 6.

This strain equation takes the strain changes in the FBG due to temperature into account, and for this compensation to be applied correctly, all FBG sensors are manually added into the software. The four temperature sensors belonging to each rebar have been calibrated at the factory before, but need to be added in manually in the system, using the temperature equation:

$$T = T_{s1}\left(\frac{\lambda_{T,act} - \lambda_{T,ref}}{\lambda_{T,ref}}\right)^2 + T_{s2}\left(\frac{\lambda_{T,act} - \lambda_{T,ref}}{\lambda_{T,ref}}\right) + T_{s3} \qquad (6)$$

With:

T = Temperature [°C]
T_{s1} = Temperature sensitivity 1
T_{s2} = Temperature sensitivity 2
T_{s3} = Temperature sensitivity 3
$\lambda_{T,act}$ = Actual temperature wavelength [nm]
$\lambda_{T,ref}$ = Reference temperature wavelength [nm]

In the equation, the sensitivities and the reference wavelength are provided in the product sheet. During the calibration, the interrogator reads the actual temperature wavelength, and combines the input values in the equation to read a temperature as provided by the temperature FBG sensor.

Once the equation and these values are input into the software, in subsequent measurements. The measured temperature wavelengths will automatically be inserted in this equation to obtain a temperature reading. This is important for the next equation, which will calculate the mechanical strain as measured by the FBGs embedded in the rebars, using the temperature measured to compensate with. The following strain equation is used in the software. The strain coefficients A and B are provided in the product sheet. The initial values for temperature are input as the rebar is in a neutral state. Consequent measurements will always compare values to this neutral state.

$$\Delta\epsilon = \frac{\frac{\lambda_{act} - \lambda_0}{\lambda_0} - B \times (T_{act} - T_0)}{A} \qquad (7)$$

With:

$\Delta\epsilon$ = Strain shift [με]
λ_{act} = actual measured strain wavelength [nm]
λ_0 = initial strain wavelength [nm]
T_{act} = Actual temperature [°C]
T_0 = Initial temperature [°C]
A = Strain coefficient $\mu\varepsilon^{-1}$
A = 7.75842×10^{-7} $\mu\varepsilon^{-1}$
B = Strain coefficient [°C]
B = 5.89292×10^{-6} $°C^{-1}$

3.4.3 FBG location in girder

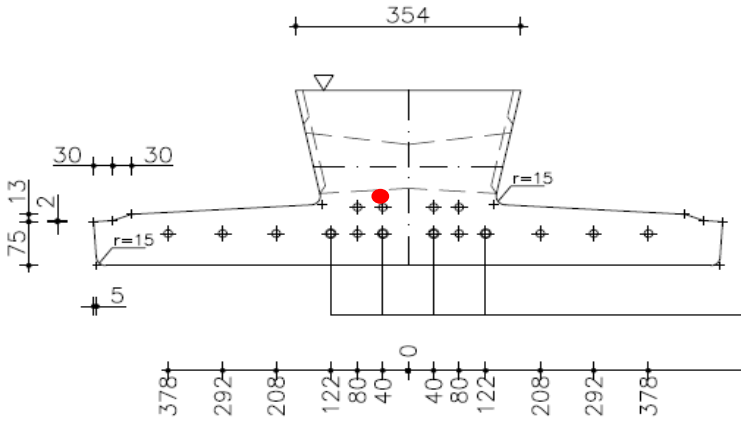

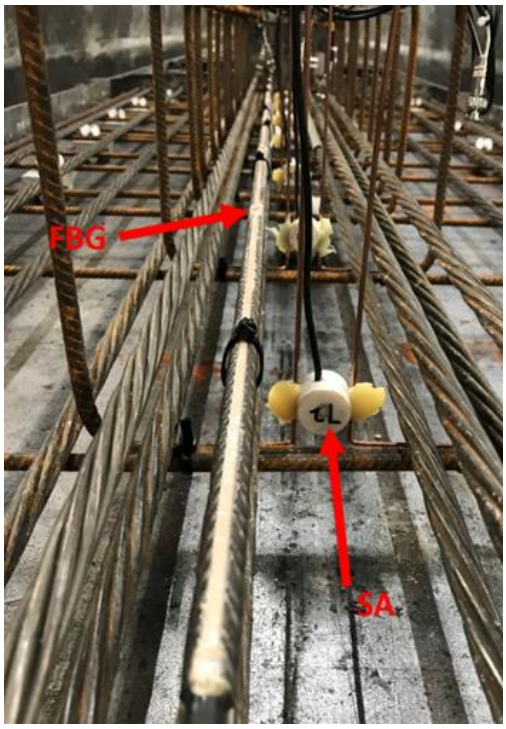

Figure 3-19: Left: Location of FBG sensors, above the prestressing strand in the cross section

Right: Photo taken showing location of FBG-integrated rebar and a Smart Aggregate sensor. Photo taken by Hao Cheng

The location of the FBGs in the cross section location is visible in the figure above. This location close to the prestressing strand is chosen because of the ability to monitor strain data that is relevant to investigate the transmission length, as well as cracking behaviour. This position aims to detect cracks as they are propagating to the tensile core (steel tendons and reinforcements) of the girder. The two differing setups of FBGs have a different setup location when looking at the longitudinal axis of the girder. Chronologically, the first FBGs to be integrated, are applied in 2 separate girders to be used in the mock-deck. Of course, the mock-deck will only be complete after the topping has been cast.

The girders used in the mock-deck are casted on September 10th. Until the topping is cast in Ghent, roughly four weeks later, the girders with integrated FBGs can supply data regarding the strains experienced before and after prestressing has been applied, as well as data regarding the strain changes during the strengthening/curing process caused by creep and shrinkage.

The purpose of this set of FBGs is to collect data after casting, as stated before, as well as collecting data during the cyclic loading test, and the residual strength tests. The rebar with FBGs integrated in specimen 1: Short 1, is seen in Figure 3-20, this is not to scale and just an indicator of the distances between FBGs and the edge of the girder with the load position used in the slab bending test. Distances of the strain sensors as well as the pure temperature sensor relative to the edge of the girder are collected before casting.

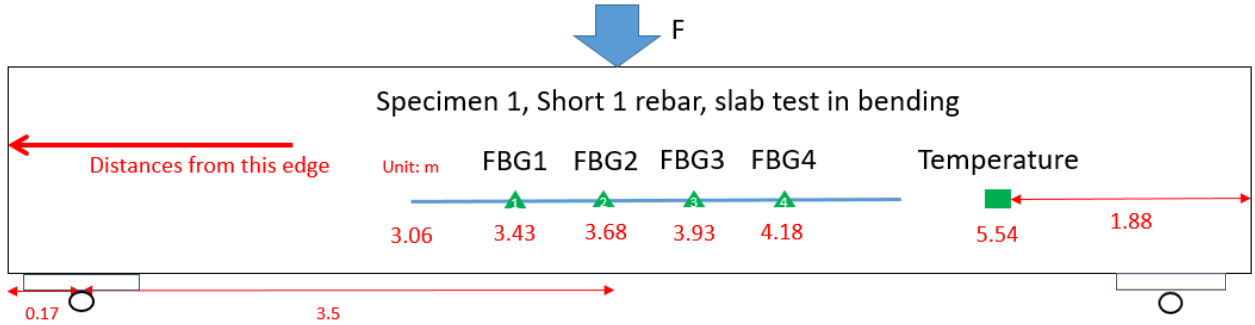

Figure 3-20: Schematic of Short 1 FBG locations relative to the edge of the specimen 1 girder, image is not to scale.

For specimen 2, the longer rebar (Long 1) is located closer to the edge of the girder as seen in Figure 3-21. This location relative to the edge of the girder is chosen to investigate the transmission length of this specimen. This section of the girder is affected by the transmission length, this should be visible in the strain measurements as the transferred force increases further from the edge of the girder. The sensors measure the strain in the concrete near the prestressing tendons. The transmission length phenomenon should manifest with the sensor closest to the edge measuring the lowest strain, and increasing the further away a sensor is positioned from the edge.

There is an additional complexity due to 4 tendons being unbonded for the first 1000 mm. The analysis of the transmission length will feature data from the FBGs in Long 1. Details regarding this analysis can be seen in Chapter 4.2.

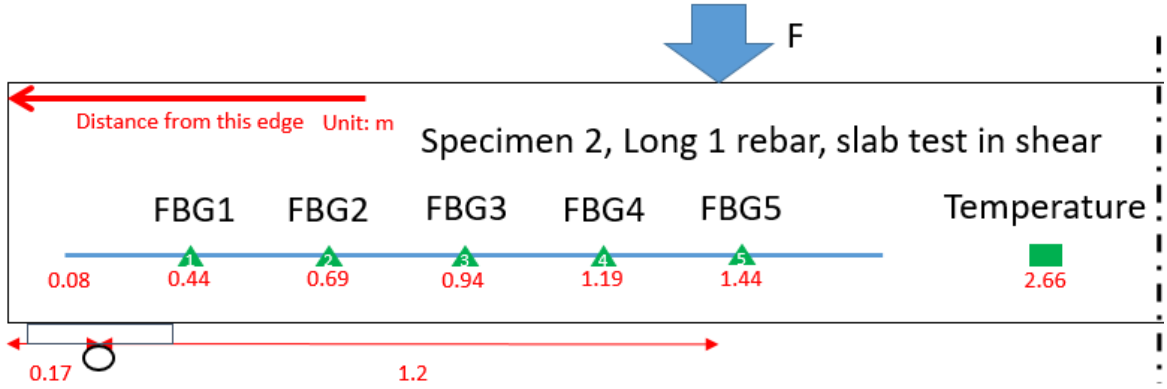

Figure 3-21: Schematic of Long 1 FBG locations relative to the edge of the specimen 2 girder, image is not to scale.

As for the girders cast on 17 September, Specimen 3 and 4 are integrated with FBG sensors. Specimen 3 will ultimately be subject to a flexural test, while specimen 4 will undergo a shear test. Both tests will occur 4 weeks after the topping has been cast. For the girder to be tested in a 4-point bending test, the same kind of shorter FBG embedded rebar has been applied at the height in Figure 3-19. This is the second of the shorter rebar series and dubbed: Short 2. The distances in the longitudinal axis differ slightly, compared to the rebar present in specimen 1, as seen in Figure 3-22.

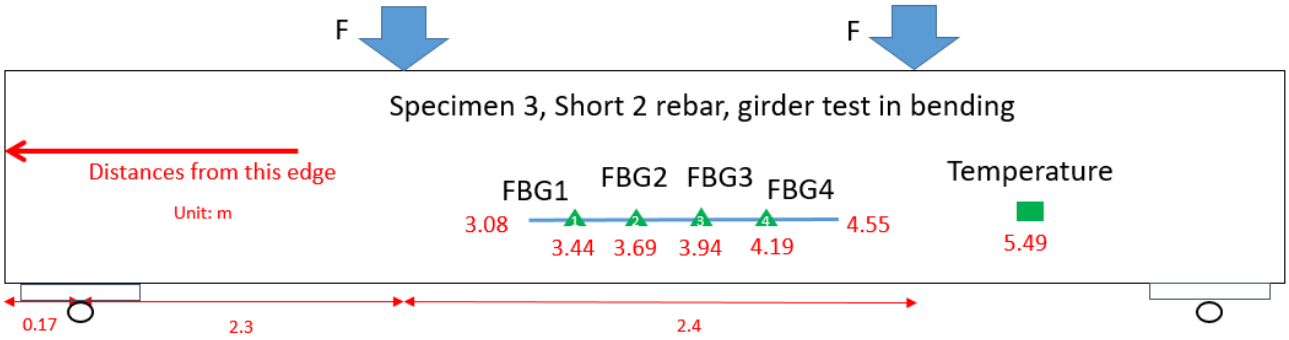

Figure 3-22: Schematic of Short 2 FBG locations relative to the edge of the specimen 3 girder, image is not to scale.

The final set of FBGs is inside of the girder to be tested in shear, specimen 4. Once again, the longer variant of the embedded rebar is used. This is positioned close to the edge of the girder to provide an additional dataset for the transfer length investigation, as well as providing data for the shear test.

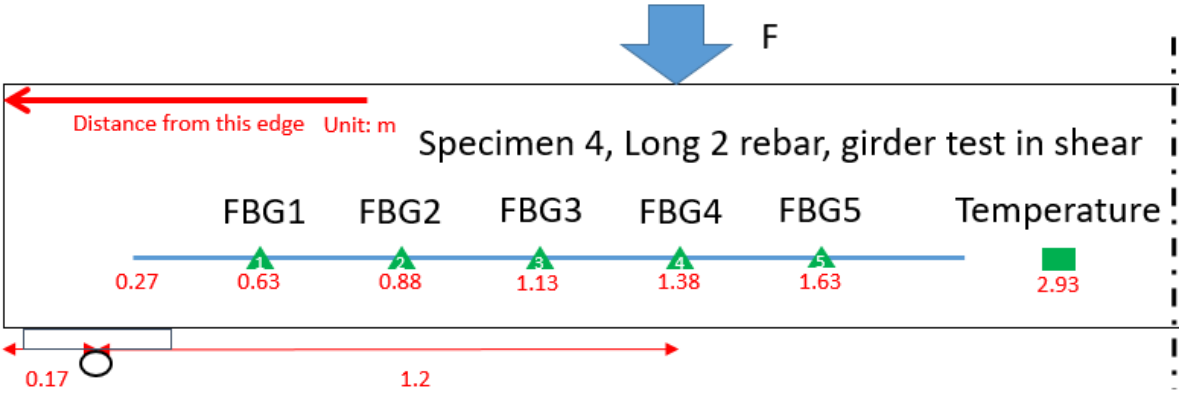

Figure 3-23: Schematic of Long 2 FBG locations relative to the edge of the girder, image is not to scale.

The distances in relation to the edge closest to FBG 1 summarized in the table below:

Table 2: FBGs and their distances relative to the beam edge closest to FBG 1, as integrated into 4 different girders.

Specimen #	Rebar+sensor type	FBG1 (m)	FBG2 (m)	FBG3 (m)	FBG4 (m)	FBG5 (m)	Temp. (m)
Specimen 1	Short 1	3.43	3.68	3.93	4.18	-	5.54
Specimen 2	Long 1	3.44	3.69	3.94	4.19	-	5.49
Specimen 3	Short 2	0.44	0.69	0.94	1.19	1.44	2.66
Specimen 4	Long 2	0.63	0.88	1.13	1.38	1.63	2.93

Also of note are the round trip distances, these are the distances from interrogator through the fiber optic cables to the individual FBGs and back. These distances are calculated and input into the software. The accuracy of these inputs has to be within a meter, as told by Fugro instructors.

3.5 Test setups

3.5.1 Flexural test

The first (destructive) test is on the specimen 3 with FBGs of the series Short 2. The flexural test is performed on 15/11/2021, 28 days after the casting of the topping. The girder is resting on supports that are 7 meters apart. The girder transfers the load to each support via a steel plate of 350 x 280 mm with a thickness of about 30 mm. The plate is connected to the girder with a thin mortar bed as

Figure 3-24: Picture examples of the blocked roller, and roller support with a metal plate between girder and supports, visible is the thin layer of mortar between the steel plate and girder.

seen in Figure 3-24. One of the supports is a roller, the other one is a blocked roller to simulate a hinge. These support conditions are the same for each girder test. The two hydraulic jacks are positioned at 2.3 m from the supports, and the load is transferred to the girder via two HEM600 spreader beams spanning the full width of the specimens. The spreader beams are positioned on top of a mortar bed of approx. 10 mm thickness. The flexural test setup can be seen in the figure below.

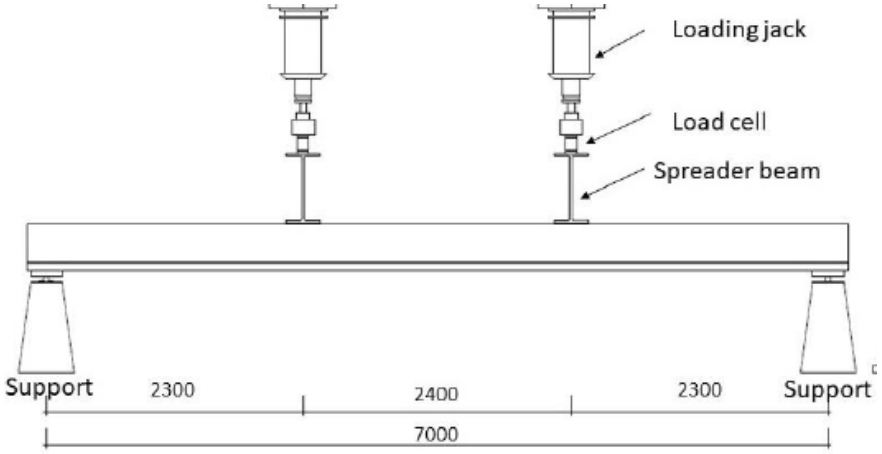

Figure 3-25: Flexural test setup at the Magnel Lab at Ghent University (Matthys, Proia, Sun, Ghorbani, & Krajnovic, 2022)

3.5.2 Shear test

The individual shear test is performed on the girder with FBGs of the series Long 2. The test is carried out on 19/11/2021, 32 days after the casting of the topping. The support setup is the exact same as the flexural test, but the location of the spreader beam and the loading jacks are changed to create a 3-point bending test setup.

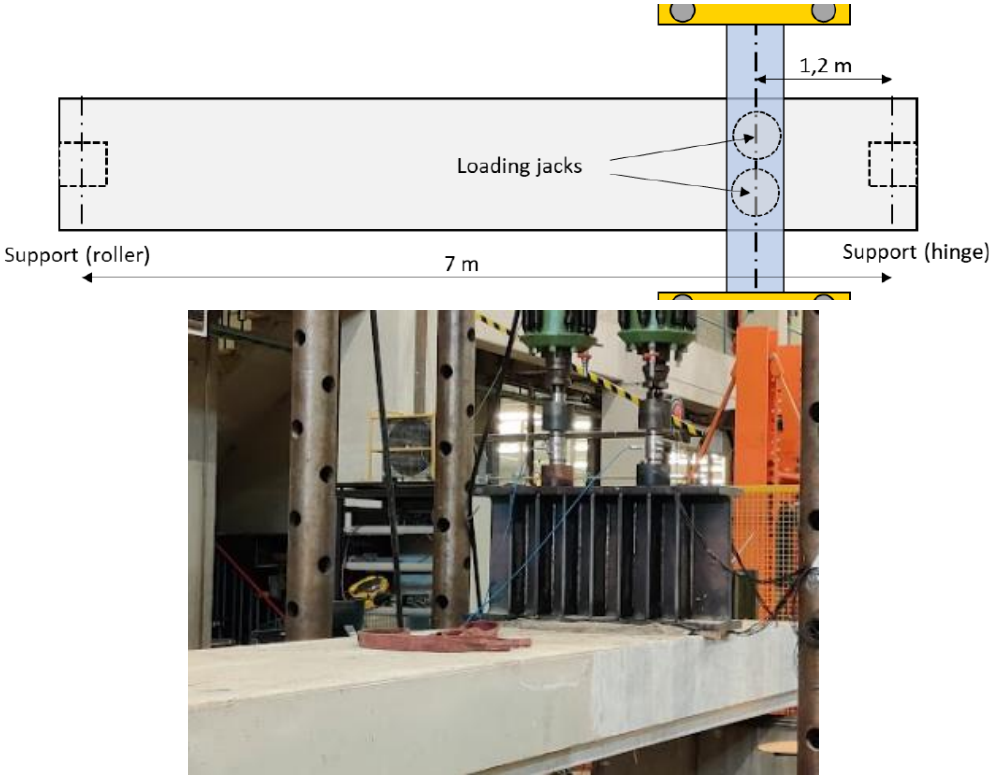

Figure 3-26: Top: Schematic top view of the single girder shear test setup. (Matthys, Proia, Sun, Ghorbani, & Krajnovic, 2022) Bottom: Photo of the side of the shear test setup

3.5.3 Mock-deck test setups

Two static load tests were performed on the same slab after the cyclic load test. (See appendix B1 and B2 for setup and results). The first of the two is performed shortly after the cyclic load test is the flexural test. A schematic top view can be seen in the figure below. The middle girder contains the Short 1 FBGs, and the girder on Side C contains Long 1 FBGs. Side B is on the aforementioned door side of the building, while side D is on the clock side.

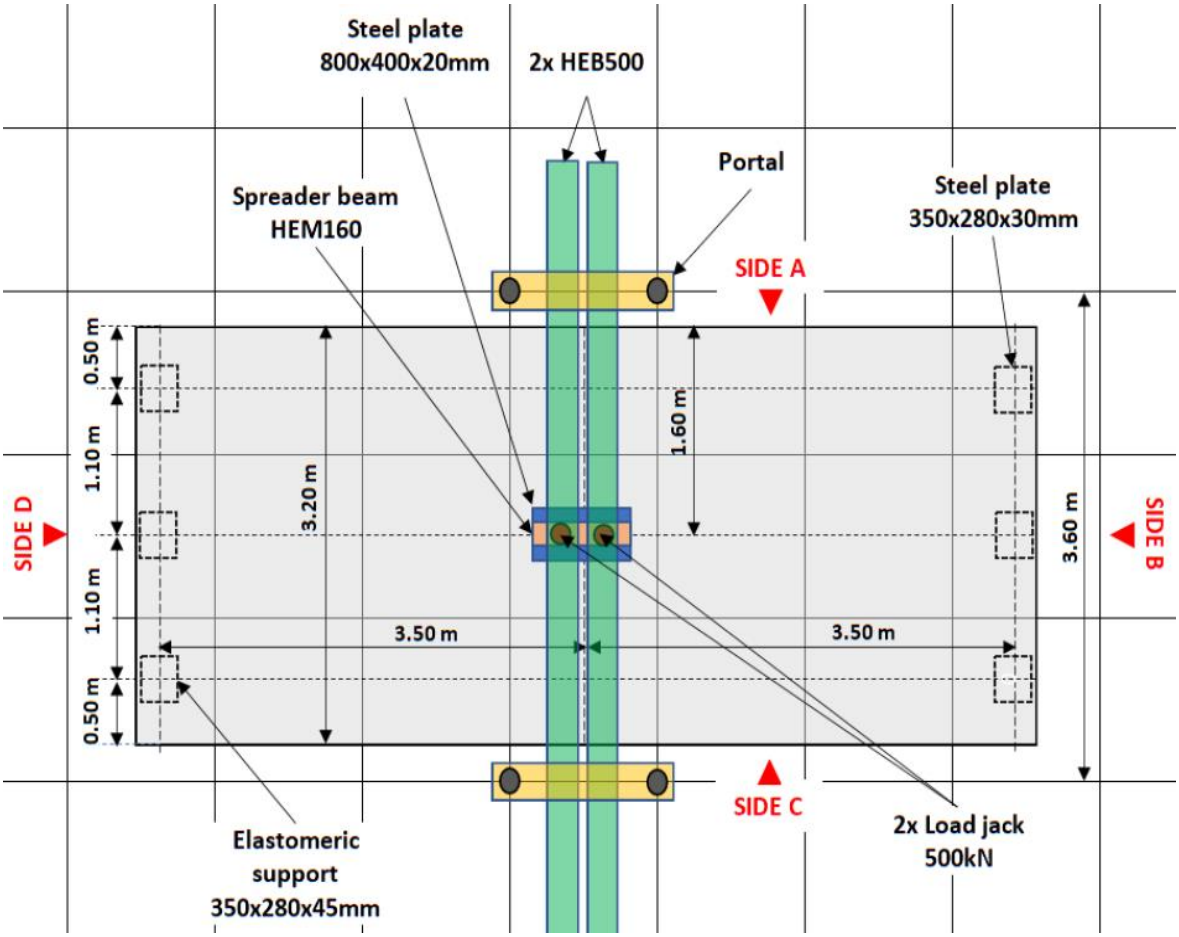

Figure 3-27: Schematic top view of the flexural test setup on the slab (Matthys, Proia, Sun, Ghorbani, & Krajnovic, 2022)

For this flexural test, the FBG sensors of Short 1 will be used for monitoring. These 4 sensors are in the middle of the span near the loading point. The sensors are positioned in such a way that they are near, or inside the area with the highest occurring moments, to possibly detect cracks deformation or propagation. The load comes from two hydraulic jacks with a capacity of 500 kN each. The load is transferred to the slab via a steel plate of 800x40x20 mm on a mortar bed layer. A HEM160 spreader beam between the jacks and the plate allows for the load to be spread more evenly on the steel plate. The slab is supported on side B on steel plates that are positioned on rollers, and on the other side on three elastomeric supports.

The other static load test is the slab shear test performed 9 days after the first test and features the load applied closer to the elastomeric supports on the clock side (side D) of the slab. Support conditions and the setup of the jacks is the same as in the previous test, aside from the location of the applied load as seen in the schematic in the figure below. The load is positioned between the sensors of Long 1 and Short 1. The sensors of Long 1 will be monitored continuously in this test.

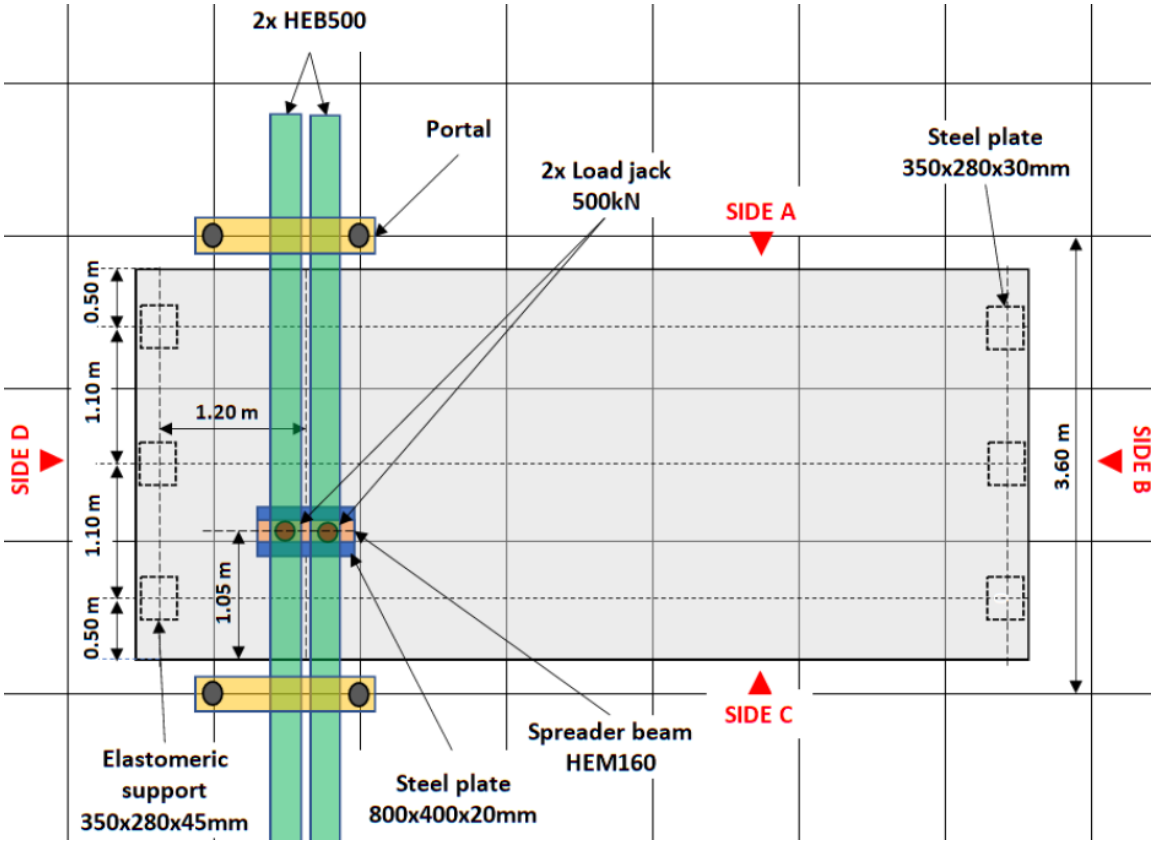

Figure 3-28: Schematic top view of the shear test setup on the slab (Matthys, Proia, Sun, Ghorbani, & Krajnovic, 2022)

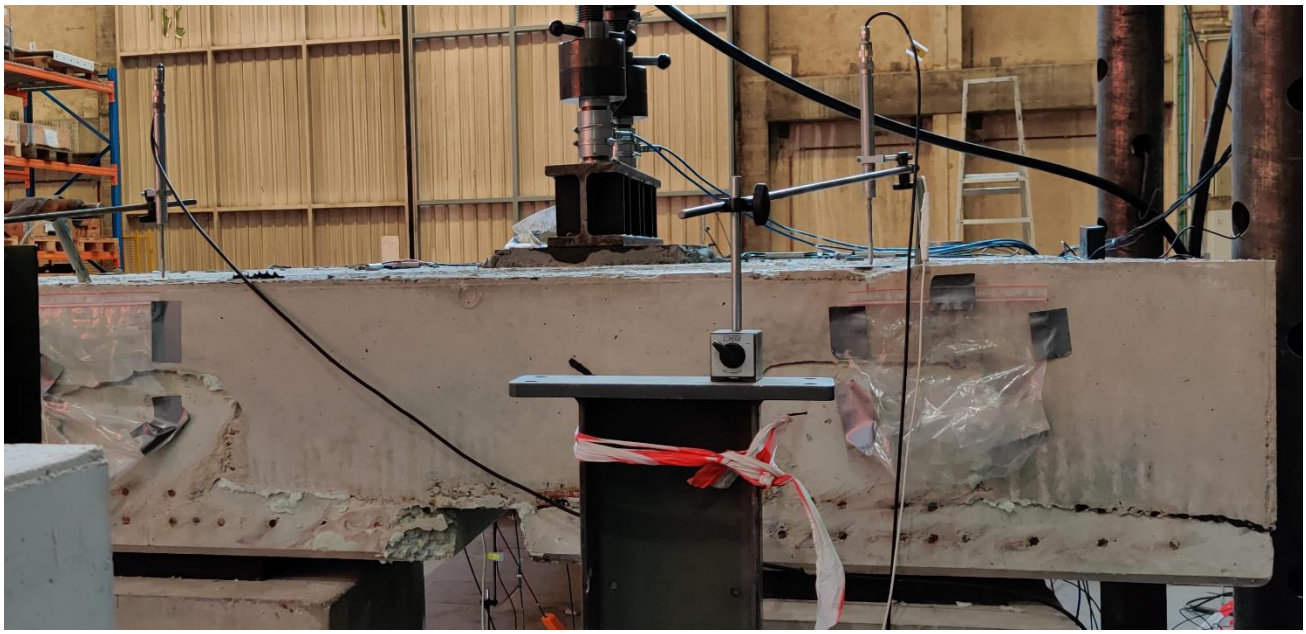

Figure 3-29: Photo taken from side D (clock side) of the test setup on 08/12/2021. Visible on the right: White fiber optic cable belonging to rebar Long 1

4 Results and analyses of FBG monitoring

This chapter describes observations, analyses, and modelling following FBG monitoring performed at multiple points in time. This includes all measurements performed before and after prestressing has been released, measurements before the tests, and measurements during the tests. As the different specimens have different casting dates and multiple moments of measuring, a condensed and simplified timeline of a specimen is shown below for clarification.

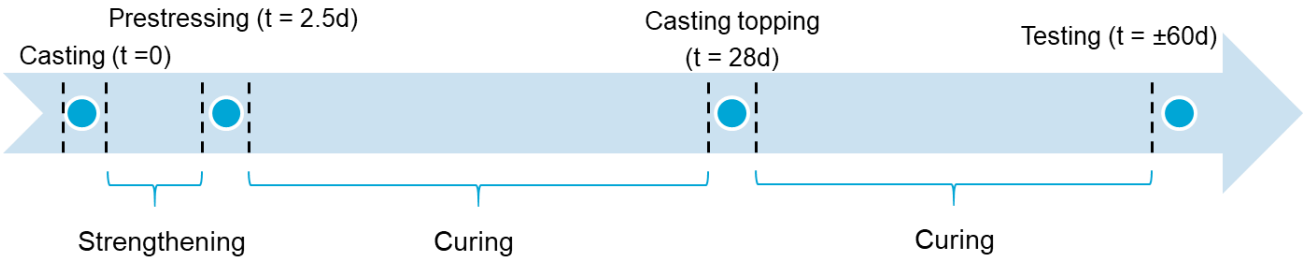

Figure 4-1: Timeline of a precast prestressed girder specimen

4.1 Prestressing losses

For the analysis on prestressing losses according to FBG monitoring, measurements are used between the moment the prestressing is released, and the moment before testing, during curing:

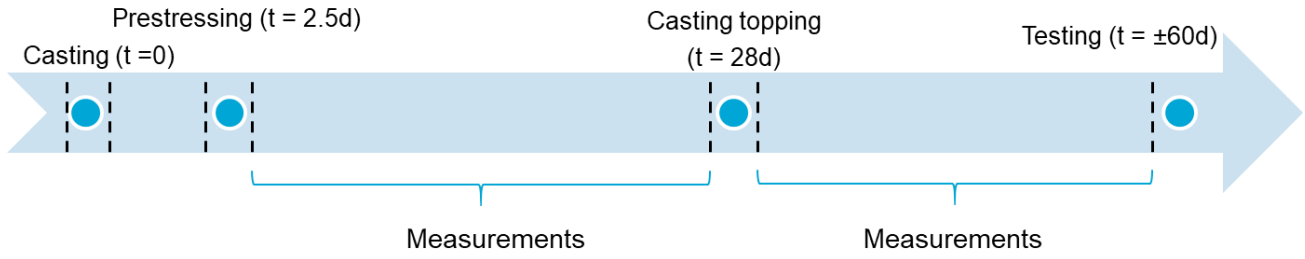

Figure 4-2: Timeline of used measurements for analysis of prestressing losses, measurements are not continuous but rather discrete points in time during curing

4.1.1 FBG measurements before bending test

For the beam tested on bending, Specimen 3, the set of FBGs embedded inside the precast prestressed girder is Short 2. This rebar is located in the middle of the span, and in the heart of the cross section, 100 mm above the bottom of the girder, and right on top of a prestressing strand. Between casting of the girder, prestressing of the strands, casting of the topping, and testing day, several measurements of the FBG have been recorded. However, due to the distance between the beams positioned at the Haitsma yard in Friesland, and Delft, there is a lack of measurements which is not optimal, but very workable still.

The raw unedited strain data can be seen in Figure 4-3. Notable in this graph is the sharp increase of strain at day 3, which is the day the prestressing has been applied, and the decrease in strain on day 32, when measurements were made before and after the topping has been cast. To refine this data into a graph that shows a change of strain over time due to shrinkage and creep only, the strain change due to the casting of the topping can be left out, this is because there is a negligible amount of creep and shrinkage happening in the precast girder between these points of

measurement. For the prestressing, however, more attention needs to be applied. Only measurements of the FBGs in the middle of the girder (Short 1, Short 2) will be used for prestressing loss analysis, because the FBGs close to the edge are undesirable, due to proximity to the edge of the beam, and thereby influenced by the transmission length.

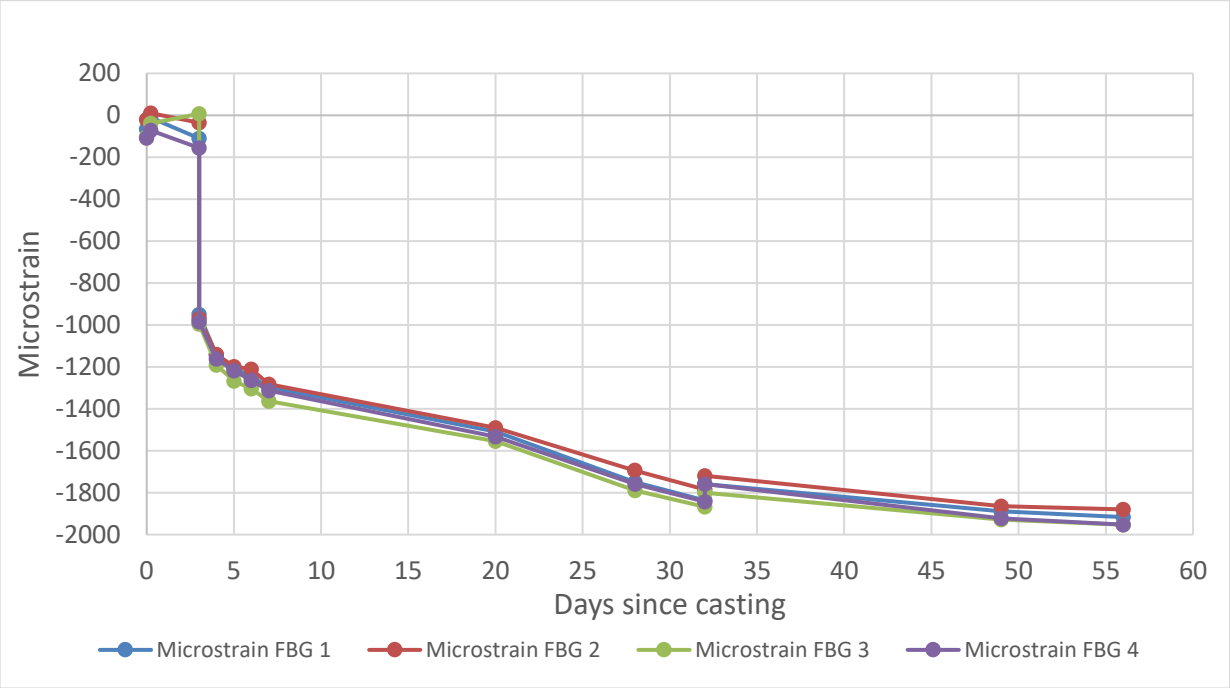

Figure 4-3: Raw strain data from Short 2 FBG measurements before testing

In this precast girder (specimen 3) specifically, the measurement of the FBGs after prestressing has been done about 2-3 hours after prestressing has been applied. This is not the strain increase occurring purely due to the release of prestressing, as there is creep occurring in the 2-3 hours after prestressing has been released. The exact quantity is hard to pinpoint, as there is no measurement directly after release of the prestressing. Therefore, laboratory tests from the Microlab are used to quantify an amount of creep that could have occurred in the time between prestressing and FBG measurements. The bar graphs below show the increase of strain between two measurements, including the unquantified creep strains. Data from both specimen 1 (Short 1) and 3 (Short 2) are shown, with their positions relative to the temperature side edge of the beam.

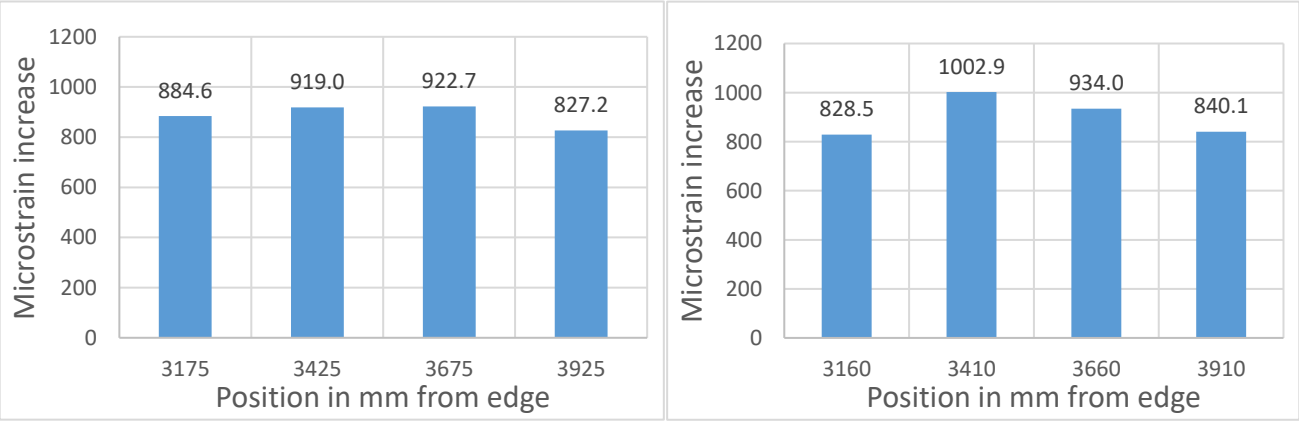

Figure 4-4: Absolute strain increase between FBG measurements right before, and 2 to 3 hours after prestressing has been applied
Left: Short 1. Right: Short 2

Data from the lab test on creep has been acquired from the Microlab, and the first three hours of creep strain after the start of the test are visible in the graph in Figure 4-5.

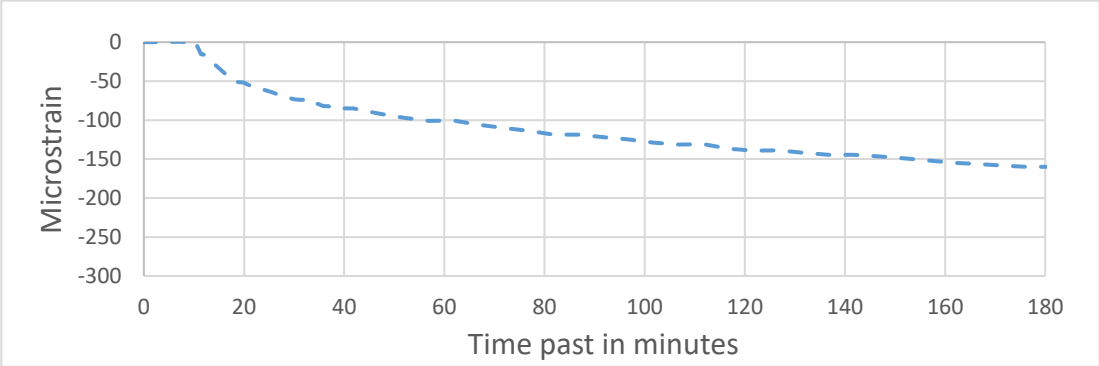

Figure 4-5: First 3 hours of creep in a lab test, pressure = 17 MPa

An important factor is that the test has been performed using 17 MPa of pressure. This is comparable enough with the pressure that the prestressing strands apply on the precast girder cross section. To go deeper into this, the prestressing force right after prestressing can be calculated using the prestressing forces, and immediate losses due to relaxation and elastic deformation, as stated in Eurocode 1992-1-1 chapters 3.3.2 (relaxation class), 5.10 (immediate prestressing losses), 10.3.2.1 (relaxation losses). Since the elastic loss is dependent on the stress at the location of the prestressing strands, which is in turn dependent on the prestressing forces, the determination of the elastic loss is an iterative process. Some assumptions have been made when information was lacking, such as the value t_{eq} a value that is added after time of tensioning in the relaxation time functions to cater for the effects of heat treatment on the prestressing losses due to relaxation. First off, the prestressing losses due to relaxation and instantaneous deformation are calculated at the moment right after prestressing is released.

4.1.2 Relaxation loss

Relaxation losses will be calculated using Chapter 3.3.2 of Eurocode 2. For class 2 strands, the value for ρ_{1000} can be assumed as 2.5% according to 3.3.2 (6). Formula 3.29 will be used to determine the relaxation loss ($\Delta\sigma_{pr}$) as a ratio of the initial prestressing stress σ_{pi} :

$$\frac{\Delta\sigma_{pr}}{\sigma_{pi}} = 0.66\,\rho_{1000}e^{9.1\mu}\left(\frac{t}{1000}\right)^{0.75(1-\mu)}10^{-5} \qquad (8)$$

Where t is the time after tensioning in hours $\mu = \sigma_{pi} / f_{pk}$ where f_{pk} is the characteristic value of the tensile strength of prestressing steel, the strands used are Y1860S7, so the f_{pk} is 1860 MPa. To calculate the relaxation loss that occurs right after prestressing, 10.3.2.1(2) states that an equivalent time t_{eq} needs to be added to the time after tensioning: t. This is to take into account the effects of heat treatment on the prestress losses due to prestressing steel relaxation. Formula 10.2 in Eurocode 2 estimates this equivalent time. A value of 16 hours is used in calculations involving this prestressing steel, and will also be used in this instance. This gives a value for the relaxation loss $\Delta\sigma_{pr}$ of 10.12 MPa, as all other values are known. Multiplying this by the total steel strand area of 16 strands x100 mm^2 gives a total prestress relaxation loss of ΔF_{pr} = 16.2 kN

4.1.3 Elastic loss

The elastic loss for pre-tensioning is due to the elastic deformation of the concrete due to the prestressing action from the tendons, as they are (gradually) released. This loss is calculated using the prestressing force right after prestressing, including relaxation losses, and the elastic loss itself. For the first calculation, elastic losses are assumed to be 0, and with iteration, the elastic loss will be approximated with convergence. The formula is as follows:

$$\Delta F_{pel} = \frac{\sigma_{c,Pm0} + \sigma_{c,eg}}{E_{cm}(t)} E_p A_p \qquad (9)$$

This uses the strain in the concrete caused by prestressing at the effective centre where the prestressing is applied, and multiplies it by the E-modulus of the prestressing steel and the total area of the prestressing steel to calculate the losses.

First off, the effective ''centre'' of the prestressing force is calculated. There are 12 strands at 55 mm from the bottom of the girder, and 4 strands at 100 mm from the bottom. This is equivalent to as if the prestressing force is applied via 16 strands at (12×55+4×100)/16 strands = 66.25 mm from the bottom of the girder. This location is used for the calculation of concrete stress at the point where the prestressing force effectively is located. Because the prestressing force is not working in the same location as the centre of gravity of the girder, this force will also generate a moment that works on the entire beam due to eccentricity. This moment will also influence the stress in the effective ''centre'' of the prestressing force at 66.25 mm (a_p) from the bottom of the girder.

The concrete at this position will shrink linear elastically due to the stress in the concrete as a result of prestressing, this will also be counteracted slightly by the stress due to the moment caused by the own weight of the girder. The concrete stress at 66.25 mm from the bottom of the girder is calculated by adding these two together. First, the stress due to own weight is calculated, this is calculated using the maximum moment due to own weight, and multiplying it with the distance of the prestressing force centre to the centre of gravity of the girder and dividing by the second moment area:

$$\sigma_{c,eg} = M_{eg}(z_{cog} - a_p)/I_{zz} \qquad (10)$$

Moment due to own weight is calculated by the basic formula for moment due to a constant load q , the load q in this case is simply the area of the girder multiplied by the volume weight of concrete, assumed to be 23 kN/m^3, the area of the girder is 156085 mm^2, so:

$$q_{eg} = 23 * \frac{156085}{10^6} = 3.59 kN/m$$

Using a span of 7 m, the moment due to own weight becomes:

$$M_{eg} = \frac{1}{8} q_{eg} L^2 = 21.99 kNm \qquad (11)$$

Now, the stress due to own weight can be calculated using above values and known values of the location of the centre of gravity from the bottom of the girder, and the second moment of area.

$$\sigma_{c,eg} = 21.99 \times 10^6 * \frac{(110 - 66.25)}{1197 \times 10^6} = 0.80 N/mm^2 = 0.80 MPa$$

The concrete stress due to eccentric prestressing is now calculated. This is done by assuming a prestressing force F_{pm0} is working the cross section at 66.25 mm from the bottom. This prestressing force takes into account the initial prestressing force minus the losses due to relaxation and the elastic loss. Due to the nature of this calculation being part of calculating the elastic loss, several iterations need to be made to converge on the actual value of elastic loss as stated before, so the first calculation will be made using the relaxation loss and the elastic loss at 0. The concrete stress due to eccentric prestressing is as follows:

$$\sigma_{c,Pm0} = -\frac{F_{Pm0}}{A_c} - F_{pm0}\left(z_{cog} - a_p\right)^2 / I_{zz} \qquad (12)$$

This first term is the stress caused by the prestressing force over the entire cross section, and the second term is the stress caused by the moment due to eccentricity. For the first iteration, the prestressing force is:

$$F_{pm0} = F_{pmax} - \Delta F_{pr} - \Delta F_{pel} \qquad (13)$$

$$F_{pm0} = 2240 - 16.2 - 0 = 2223.8\ kN$$

This gives a value to use in equation 12, giving:

$$\sigma_{c,pm0} = -\frac{2223.8 \times 10^3}{156085} - 2223.8 \times 10^3 \frac{(110 - 66.25)^2}{1197 \times 10^6} = -17.8\ MPa$$

Now all values are available to calculate the elastic loss using equation 9.

The E-modulus of the geopolymer concrete at time of prestressing (3 days after casting) is assumed to be 24000 MPa, this is a value obtained by testing in the early phases. This value can still change due to newer test results, but will suffice for the time being. E_p and A_p are the E-modulus and the area of the prestressing steel, respectively, The E-modulus is assumed to be 195000 MPa, and the steel area is known at 1600 mm^2 The first iteration using equation 9 becomes:

$$\Delta F_{pel} = abs\left(\frac{-17.8 + 0.874}{24000} \times 195000 \times 1600\right) = 221.9\ kN$$

By putting this value back into the equation for prestressing force at time 0 and iterating, the elastic loss will be found via convergence in 5 iterations:

$$\Delta F_{pel} = 200.2\ kN$$

This gives for equation 13:

$$F_{pm0} = F_{pmax} - \Delta F_{pr} - \Delta F_{pel} = 2240 - 16.2 - 200.2 = 2023.6\ kN$$

The tendon stress just after release becomes:

$$\sigma_{pm0} = \frac{F_{pm0}}{A_p} = \frac{2023.6\ kN}{1600\ mm^2} = 1265\ MPa$$

A summary of the prestressing loss calculations in table form can be seen below:

Table 3: calculations according to EC2, applied on prestressing losses right after prestressing.

Prestressing losses calculations				EC2
total initial prestressing force	$F_{p,max}$	2240	kN	5.10.2.1
elastic loss manual fill in by iteration	ΔP_{el}	200.16	kN	5.10.4
relaxation loss	ΔP_{pr}	16.19	kN	10.3.2.1
total prestressing force, after prestressing losses	**Pm0**	**2023.6**	**kN**	5.10.3
stress in steel, after prestress losses	σ_{pm0}	1264.8	MPa	
stress in concrete section		-13.0	MPa	
strain in concrete section		-540.2	με	
iteration elastic loss		-200.16	kN	
Relaxation class 2	p1000	2.50	%	3.3.2
$\mu = \sigma_{pi}/f_{pk}$ with $\sigma_{pi} = \Delta\sigma_{p,max}$= 1400 MPa		0.753		
$t = t_{eq}$		16.00	hours	10.3.2.1
$\Delta\sigma_{pr}/\Delta\sigma_{pi}$		0.0072		
$\Delta\sigma_{pr}$		10.12	N/mm2	

This results in a prestressing force of 2023.6 kN in the girder right after prestressing. Due to the position of the FBGs near the middle of the span, combined with their position in the cross section, the concrete near the FBGs experience effects from both the moment due to self-weight, and a moment caused by the eccentricity of the prestressing strands:

$$M_{eg} = \frac{1}{8} q_{eg} L^2 \quad (14)$$

$$M_{eg} = \frac{1}{8} \rho * A_c L^2 \quad (15)$$

With: ρ_d = assumed geopolymer concrete density at 23 kN/m^3
A_c = girder cross section area at 156085 mm^2
L = span at 7 m

This results in a maximum moment due to self-weight at 22 kNm (working to bend the beam downwards). The FBGs are not located in the exact centre of the span, where this maximum moment occurs, but the differences are negligible, so this value is chosen to be effective. Next up is the moment due to eccentricity of the working forces of the strands:

$$M_{ecc} = F_{Pm0} \times z_{cp} \quad (16)$$

With: F_{Pm0} = force in prestressing strands after losses at 2023.6 kN
z_{cp} = distance from centre of prestressing strands to centre of gravity at 110-66.25 = 43.75 mm

This results in a moment of -88.53 kNm (working to bend the beam upwards).
The stress at the FBG strands can now be calculated:

$$\sigma_{c,FBG} = -\frac{F_{Pm0}}{A_c} + \sum M \frac{z}{I_{zz}} \quad (17)$$

With: z = distance from FBGs to centre of gravity at 100 - 66.25 = 33.75 mm
I_{zz} = second moment of area of the precast girder around the ZZ-axis at 1197×10^6 mm^4

This results in a stress at FBG level of -13.5 N/mm^2 or MPa. In comparison, using the same calculations, the bottom of the girder at this same moment experiences a stress of -19 MPa. The centre of the prestressing strands (66.25 mm above the bottom of the girder) experiences -15.4 MPa in the middle of the span, where self-weight has the most impact, to -16.2 MPa closer to the edges of the span.

With this known, the creep tests performed at 17 MPa of pressure are an accurate representation, albeit slightly overestimated, what the occurring creep is near the prestressing strands. A value of 150 microstrain is decided to be used as the amount of creep that occurs between prestressing and the moment the FBG strains are recorded. The increase in strain due to applying the prestressing is now deducted from the FBGs strain measurements, minus the 150 microstrain in creep shrinkage. The change in strain due to casting of the topping has also been deducted, Figure 4-6 now purely shows changes in strain due to shrinkage and creep.

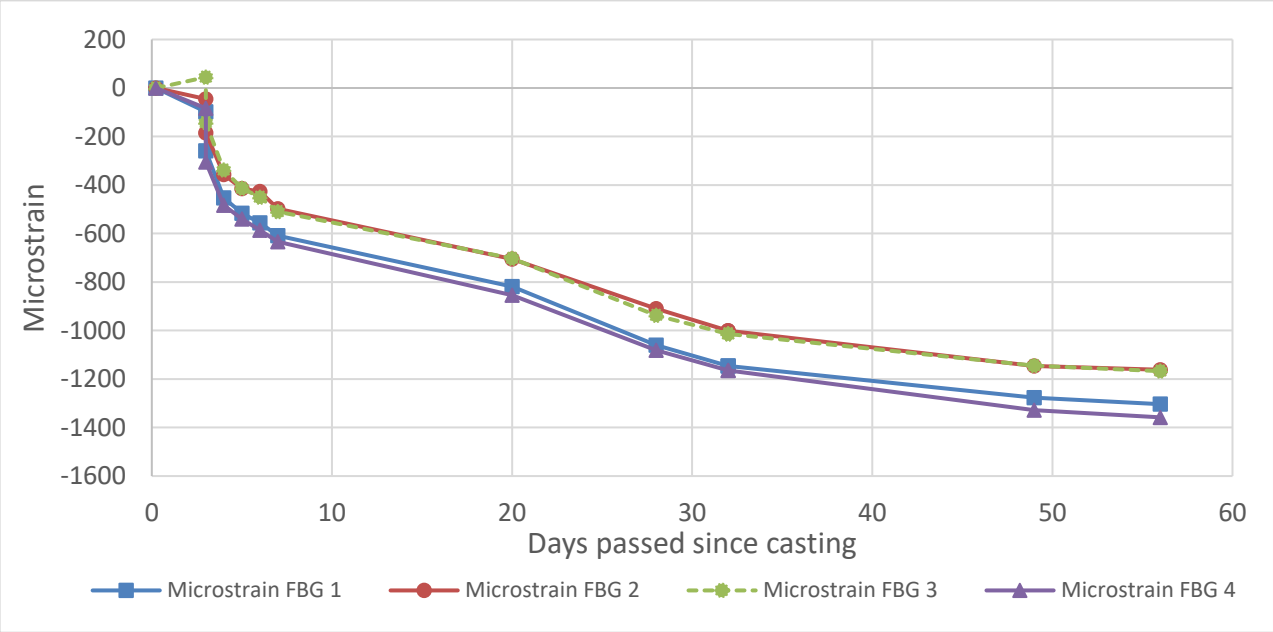

Figure 4-6: Strain change over time, as measured at the FBGs, accounted for prestressing and casting of the topping

Notable here is that the graph of FBG 3 in the first 3 days goes upwards instead of downwards. It is expected to go downwards because of the effects of autogenous shrinkage in the first 3 days. FBG 3 however, records an increase in strain. It is unknown why or how this happened, but it can be attributed to the development of the geopolymer concrete in the early stages. FBG measurements in these days are most probably affected by non-complete bond between the concrete and the rebar. Seeing as the first 3 days of shrinkage do not have an effect on the prestressing, the set of data belonging to FBG 3 is not omitted. To investigate the effects of creep and shrinkage on the prestressing losses, only the creep and shrinkage after prestressing has been applied are relevant.

The measurements before prestressing have been removed, and a new zero point has been applied. The aforementioned 150 microstrain of creep is effective from the time of prestressing (new zero point) to the first FBG measurement after prestressing. Afterwards, the changes to strain measured by the FBGs have been added up to produce a set of data that is strictly related to strain change over time. This dataset is presented in a table, and in a graph, as seen below:

Table 4: FBG Dataset of change of strain over time since prestressing has been applied

Date and comments	days since casting	**Microstrain FBG 1**	**Microstrain FBG 2**	**Microstrain FBG 3**	**Microstrain FBG 4**	**Avg.**
2021-09-20 after prestressing	3	0	0	0	0	0.0
2-3h after prestressing	3.125	-150	-150	-150	-150	-150.0
2021-09-21	4	-343	-322	-346	-328	-334.6
2021-09-22	5	-407	-380	-421	-384	-398.0
2021-09-23	6	-446	-392	-458	-431	-431.7
2021-09-24	7	-499	-463	-517	-479	-489.5
2021-10-07	20	-709	-671	-709	-699	-697.0
2021-10-15	28	-950	-875	-945	-926	-923.9
2021-10-19	32	-1037	-966	-1022	-1009	-1008.4
2021-10-19 after casting topping	32	-1037	-966	-1022	-1009	-1008.4
2021-11-05	49	-1166	-1111	-1151	-1172	-1150.1
2021-11-15 before testing	59	-1194	-1127	-1175	-1202	-1174.4

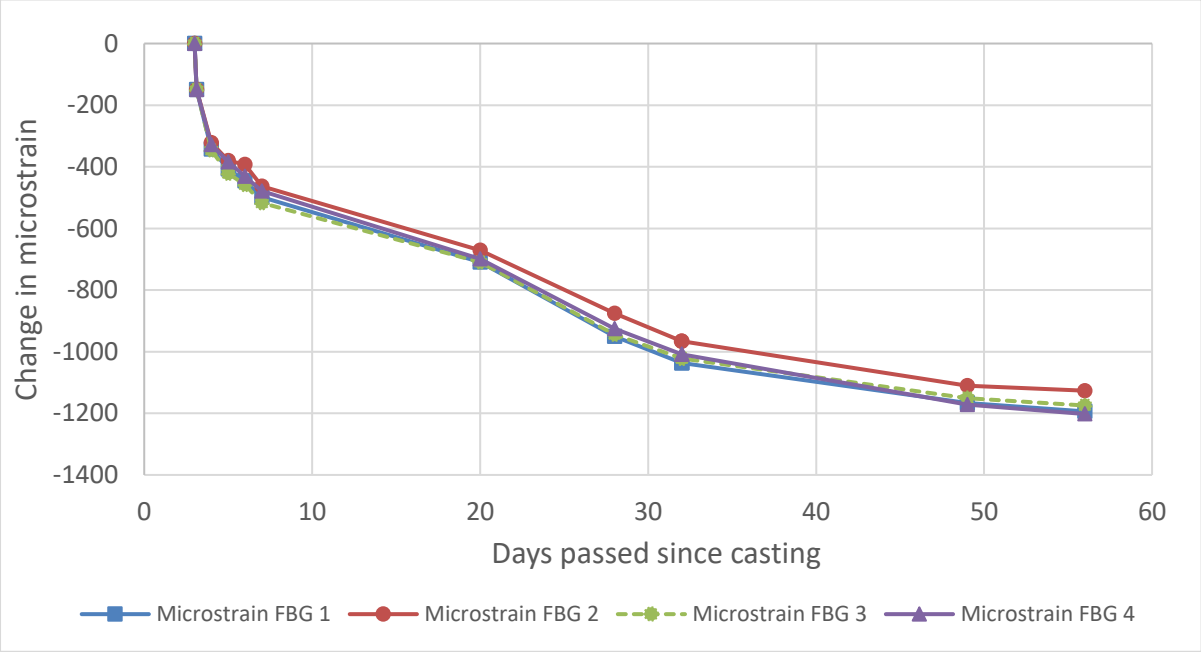

Figure 4-7: Change of strain over time in the FBGs, measurements starting at 0 at point of prestressing assuming 150 microstrain of creep occur between time of prestressing and first measurement.

4.1.4 Separation of creep and shrinkage using lab test data

To apply formula 5.46 of Eurocode 1992-1-1, these strains have to be separated into shrinkage strain and creep strain. Since there is little data available on shrinkage and creep progression of this material, especially as the FBG measurements are done in the inner core of the precast girder, where no drying occurs, assumptions have to be made.

The lab test closest resembling the FBG environment is the same test used earlier to determine the creep occurring in the first moments after prestressing has been applied. The specimen, just like the precast girder, is 3 days old when the pressure has been applied to start the creep measurements. The autogenous and drying shrinkage will also have occurred for 3 days. If assumed correctly, the conditions during the test should have been a high humidity, so the drying shrinkage should be minimal/negligible. The difference is that these prisms are a lot smaller and are subject to an overall pressure of 17 MPa versus the linear stress profile the girder has, due to eccentricity.

The first 60 days of the strain changes during the lab test can be seen in Figure 4-8. This data is also available in table form on the next page. To get an idea of the contribution of shrinkage versus the creep, the percentage of the shrinkage of the total strain is noted in a column as well. As visible, the amount of shrinkage compared to the combined time-dependent strains is consistently between 14 and 18% with a few outliers. As the conditions of this prism is similar enough to the conditions inside of the precast girder at the FBG positions, a value of 16% of the total strain change over time has been assumed to be the (autogenous) shrinkage. This is of course a rough assumption, but small errors between the portion of the shrinkage and creep of the total strain change over time are permissible. A value is just needed to start the calculation to determine the prestressing losses as seen in formula 5.46 of Eurocode 2.

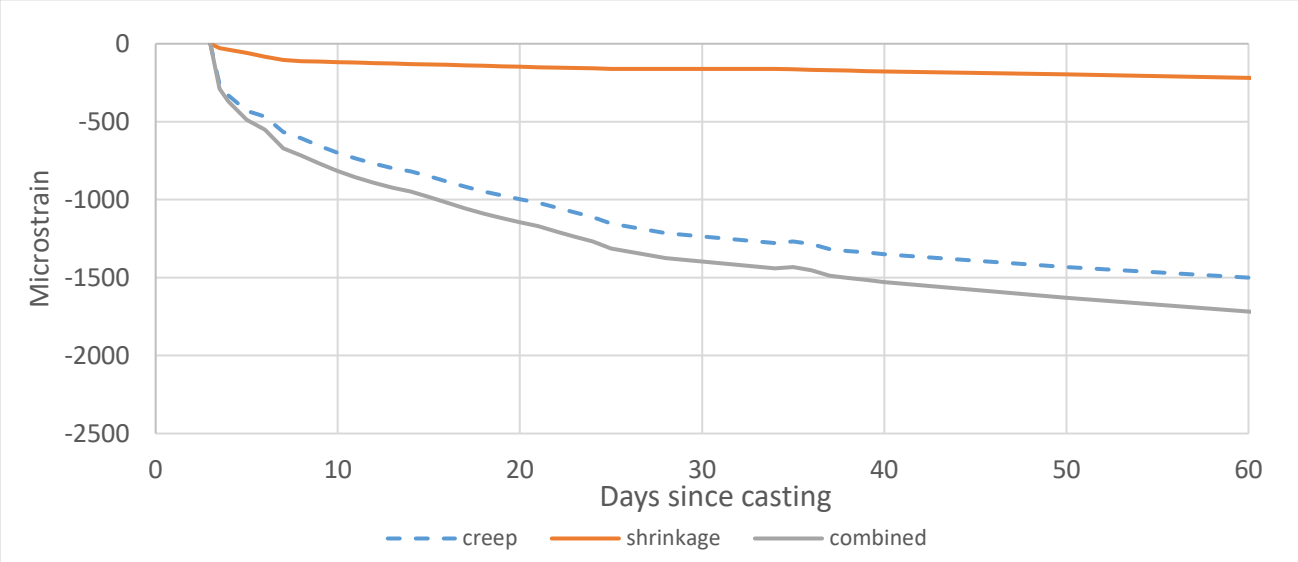

Figure 4-8: Microlab test data on geopolymer concrete prism, first 60 days of shrinkage and creep strain, tested at 17 MPa

Table 5: Microlab test data on geopolymer concrete prism, first 60 days of shrinkage and creep, tested at 17 MPa

time				
days	creep (με)	shrinkage (με)	combined (με)	shrinkage % of total
3	0	0	0	N/A
4	-265.751	-38.4067	-304.158	12.6
5	-343.058	-58.8753	-401.933	14.6
6	-373.267	-83.0787	-456.345	18.2
7	-452.335	-105.05	-557.385	18.8
8	-484.077	-111.867	-595.944	18.8
9	-523.709	-113.657	-637.365	17.8
10	-557.67	-117.637	-675.307	17.4
11	-587.835	-121.095	-708.93	17.1
12	-614.046	-124.223	-738.269	16.8
13	-636.333	-126.783	-763.116	16.6
14	-652.578	-130.023	-782.601	16.6
15	-678.096	-132.77	-810.866	16.4
16	-705.848	-135.872	-841.72	16.1
17	-732.476	-138.827	-871.303	15.9
18	-756.203	-141.181	-897.383	15.7
19	-776.958	-144.375	-921.332	15.7
20	-795.787	-147.375	-943.163	15.6
21	-814.295	-150.381	-964.676	15.6
22	-839.272	-152.583	-991.855	15.4
23	-863.829	-155.401	-1019.23	15.2
24	-887.581	-157.093	-1044.67	15.0
25	-920.549	-160.583	-1081.13	14.9
28	-968.94	-160.991	-1129.93	14.2
34	-1020.92	-161.891	-1182.81	13.7
35	-1011.97	-163.933	-1175.9	13.9
36	-1025.86	-167.377	-1193.23	14.0
37	-1052.3	-169.501	-1221.81	13.9
38	-1061.19	-172.361	-1233.55	14.0
39	-1068.78	-175.89	-1244.67	14.1
40	-1078.59	-177.621	-1256.21	14.1
45	-1113.34	-187.359	-1300.7	14.4
50	-1143.53	-197.218	-1340.74	14.7
55	-1166.74	-207.631	-1374.37	15.1
60	-1197.81	-218.239	-1416.05	15.4

Notable is that the shrinkage is consistently around 14-18% of the total measured strain as time passes.

4.1.5 Prestressing losses based on FBG measurements in bending beam (Short 2)

Following the separation of creep and shrinkage in the section before, the effects of creep and shrinkage on the prestressing forces can now be calculated using Eurocode 1992-1-1 formula 5.46.

$$\Delta P_{c+s+r} = A_p \Delta\sigma_{p,c+s+r} = A_p \frac{\varepsilon_{cs} E_p + 0{,}8\Delta\sigma_{pr} + \frac{E_p}{E_{cm}} \varphi(t,t_0).\sigma_{c,QP}}{1 + \frac{E_p}{E_{cm}} \frac{A_p}{A_c}\left(1 + \frac{A_c}{I_c} z_{cp}^2\right)[1 + 0{,}8\,\varphi(t,t_0)]} \quad (18)$$

In this formula, the prestressing losses are attributed to 3 factors: shrinkage, relaxation, and creep. The denominator remains fairly constant, except for the changes to the creep factor. The strain measured by the FBGs is split into strain due to shrinkage, and strain due to creep, using the lab test results where shrinkage seems to be consistently between 14 to 18% of the total measured strain. A value of 16% is applied to strains measured by the FBGs after prestressing to make an estimate of the creep and shrinkage that occurs in the concrete near the prestressing strands after the prestressing has been finished. This is not applied for the initial 150 microstrain of creep occurring between prestressing release and the first measurement. A summary can be seen in the table below:

Table 6: Average measured strain increases in FBG measurements and separation into shrinkage and creep

Days since casting	Average measured microstrain since prestressing	Shrinkage 16%	Creep
4	-334.6	-29.5	-305.1
5	-398.0	-39.7	-358.3
6	-431.7	-45.1	-386.6
7	-489.5	-54.3	-435.2
20	-697.0	-87.5	-609.5
28	-923.9	-123.8	-800.1
32	-1008.4	-137.3	-871.0
49	-1150.1	-160.0	-990.1
56	-1174.4	-163.9	-1010.5

On 32 days since casting, the topping has been cast. The measurements on day 49 and 56 (testing day) after casting are affected by it. Due to the increase in cross section area, the pressure caused by the prestressing strands will drop, and so will the creep coefficient. The creep coefficient is calculated using Annex B of the Eurocode 1992-1-1, as well as Eurocode 1992-1-1 Chapter 3.1.4.

The elastic modulus of the geopolymer concrete near the FBGs is not possible to measure before bending testing. The closest values for the E-modulus will be results from lab tests on samples using standard curing, which means these samples resemble the concrete near the centre of the girder, where little to no drying occurs, as this has a large impact on the E-modulus. The graph with E-modulus values can be seen in Figure 4-9, when values are needed that are between laboratory test values, they are interpolated linearly.

Table 7: Lab test on elastic modulus, standard curing

Time (days)	Elastic modulus (GPa)
	Standard curing
1	21.2
7	29.1
14	30.6
21	30.4
28	30.7
56	30.8

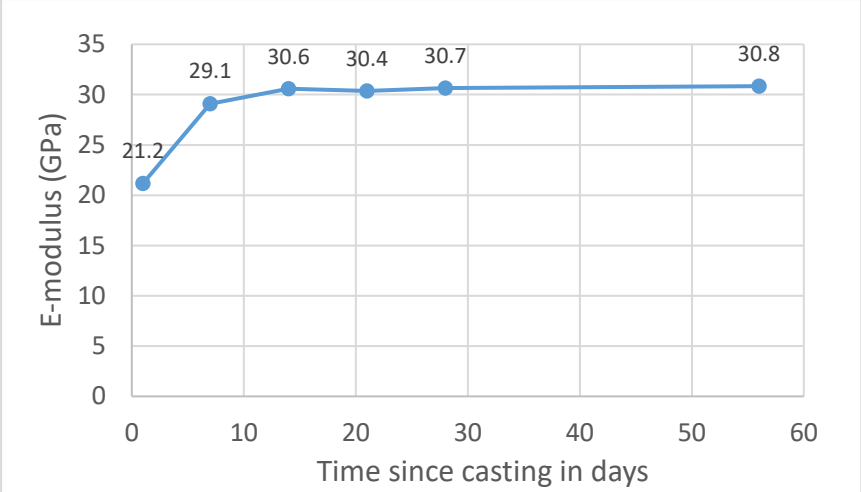

Figure 4-9: Lab test on elastic modulus, standard curing

After these considerations, the table summarizing the calculations of 5.46 is made, showing the components of the prestressing losses (s = shrinkage, c = creep, r = relaxation components)

Table 8: Components of prestressing losses following Eurocode 2 formula 5.46

Days since casting	Creep Coefficient	E_{cm}(t) (GPa)	ΔP_s (kN)	ΔP_c (kN)	ΔP_r (kN)	Denominator	total ΔP (kN)
3	0.0	23.8	0	0	0	N/A	0
4	0.52	25.1	8.8	100.6	10.2	1.042	119.7
5	0.65	26.5	11.8	118.3	10.7	1.047	140.8
6	0.73	27.8	13.4	126.8	11.2	1.048	151.5
7	0.86	29.1	16.2	142.3	11.6	1.048	170.1
20	1.26	30.4	25.9	197.6	11.9	1.049	235.4
28	1.68	30.7	36.3	248.8	14.3	1.055	299.4
32	1.82	30.7	40.2	267.4	15.6	1.064	323.1
49	1.14	30.8	47.5	304.6	17.1	1.067	369.2
56	1.33	30.8	48.4	310.7	17.4	1.067	376.5

Notable is how the creep is very large, as expected, until day 32, when the topping is cast, and the prestressing forces are distributed over the topping, as well as the girder cross section resulting in flattening out of the creep strains after day 32.

Another observation is that the (autogenous) shrinkage is lower than expected. Low drying shrinkage can be explained by the location of the FBGs on the inside of the girder, where little to no drying of the concrete occurs.

4.1.6 Conclusions

At the date of bending testing on a single girder element (Specimen 3), on the 15th of November 2021, 56 days after casting and 53 days after prestressing, an approximate prestressing loss due to creep and shrinkage of 377 kN is observed in the strands of this girder (Short 2), using strain change over time as measured by the FBGs. The strains have been separated using a ratio of 16% following data from lab tests on creep and shrinkage. This estimate is rough, but is used to get an idea of the effect of creep versus the effects of shrinkage on the prestressing forces. The creep is suggested to have the largest effect on prestressing losses with ±80% at day of testing. These losses are on top of the instantaneous losses calculated before.

In conclusion, from the moment the strands are prestressed, an approximate amount of prestressing force at 2240 kN over 16 strands is reduced to $Pm0 = 2023.6\ kN$. From there on, the effect of creep and shrinkage from the moment of prestressing until the day of testing reduce the prestressing force by another **377 kN** to arrive at a prestressing force of roughly ±1647 kN at time of testing. The total loss assuming the 16 strands are prestressed to 140 kN each, is:
2240 kN – 1647 kN = **593 kN of total prestressing losses** or 26.5%, with 216.4 kN or 9.7% attributed to instantaneous losses due to elastic deformation and relaxation, and 377 kN or 16.8% due to creep and shrinkage effects.

4.2 Transmission length

This analysis is performed using FBG data of sensors near the edge of the precast girder, Long 1 and Long 2, located in specimen 2 and 4 respectively. Data is taken right before prestressing, and after prestressing, and compared to obtain the strain change purely due to prestressing. This is then compared to current Eurocode 1992-1-1 formulas for OPC-based concretes to obtain insights of the behaviour of this geopolymer concrete in a prestressed girder regarding the transmission length.

As mentioned in the introduction, the prestressing force that is transferred from the tendons to the concrete needs a certain distance to develop. This is because the bond between the strands and the concrete is the limiting factor. The bond stress between the strands and concrete can only reach a certain value. The forces are then transferred from the strands to the concrete via the surface of the strands that is connected to the concrete. From the edge of the concrete member where the strands are cut off, the tensile forces transferred to the concrete will increase linearly as the strand goes further in to the concrete, starting from 0. This tensile force keeps increasing until the prestressing force is fully transferred to the concrete. The distance from the edge of the beam until the point where prestressing force is fully transferred is called the transmission length.

4.2.1 Transmission length according to Eurocode 1992-1-1

For investigation into the transmission length of the geopolymer concrete girder, the theoretical transmission length is calculated first, using Eurocode 2. Eurocode 2 formulas in Chapter 8.10.2.2 estimate the transmission length for regular concretes that are prestressed using pre-tensioned tendons. However, these formulas assume existing regularly used concretes. It is unknown if these formulas will yield correct values for the transmission length and bond stress in this girder.

To investigate potential differences, the bond stress and transmission length will be calculated for the prestressed girder assuming a regular C45/55 concrete. The resulting values will then be compared to FBG data in 2 prestressed girders equipped with FBG sensors near the edge: Specimen 2 and 4. By measuring the strains in 5 locations along the rebar, the progression of the strain increasing as the rebar goes further away from the edge of the concrete beam can be recorded. Since the strain in a rebar can be directly related to the strain in the concrete surrounding it, the development of the force transferred to the concrete from the pre-tensioned tendons can be tracked. This can then be used to investigate the bond stress between the tendons and the geopolymer concrete, and the acting transmission length.

The theoretical transmission length and bond stress calculated using regular C45/55 concrete parameters will then be compared with data from the geopolymer concrete beams. Comparing bond stress and transmission length following the formulas to the in-situ measurements gives an insight on the applicability of the formulas on this SCGC mixture as applied in the girders.

Strain data collected directly after prestressing is used for this analysis. This limits the effects of shrinkage and creep that occurs between prestressing and the strain measurements. Calculations will be performed assuming the time passed since prestressing = 0 hours for time-dependent values in the formulas. The findings and differences will then be discussed. First off, the bond stress and transmission length of a regular C45/55 concrete will be calculated using Eurocode 2 Chapter 8.10.2.2. The tendons used are B500B 7-wire strands, the same as in the actual beams, they have a nominal diameter of 12.9 mm, and an area of 100 mm^2 per strand. Class 2 assumed for relaxation calculations. The strands are strength class Y1860S7 (or FeP1860).

The formula for bond stress (formula 8.15) is stated in Chapter 8.10.2.2 (1) and is as follows:

$$f_{bpt} = \eta_{p1}\eta_1 f_{ctd}(t) \quad (19)$$

With:

η_{p1} is a coefficient that takes into account the type of tendon used and the bond situation at release, a value of 3.2 is used for 3 and 7-wire strands
η_1 is 1.0 for good bond conditions, which will be assumed to be the case going forward
$f_{ctd}(t)$ is the design tensile value of concrete strength at release and is equal to:
$\alpha_{ct} * 0.7 * f_{ctm}(t)/\gamma_c$, with:

$$f_{ctm}(t) = \left(\beta_{cc}(t)\right)^{\alpha} f_{ctm} \; (Eurocode\ 2\ formula\ 3.4) \quad (20)$$

With: α = 1, and $\beta_{cc}(t) = \exp\left(s\left[1 - \left(\frac{28}{t}\right)^{0.5}\right]\right)$

Using Eurocode 2 formula 3.1, $\beta_{cc}(t)$ can be calculated using:

$$f_{cm}(t) = \beta_{cc}(t) f_{cm} \quad (21)$$

With $f_{cm}(t)$ = $f_{ck}(t) + 8$, where $f_{ck}(t)$ is the characteristic strength of the concrete at time of tendon release, in calculations, a value of 30 MPa is used. This gives $f_{cm}(t)$ = 38 MPa
The used geopolymer concrete is rated as a C45/55, which means the characteristic value of the concrete compressive strength is valued at 45 MPa, using table 3.1 in EC 2, a value for the mean compressive strength f_{cm} can be found at 53 MPa. The formula becomes:

$$f_{cm}(t) = \beta_{cc}(t) f_{cm} \; or \; \beta_{cc}(t) = \frac{f_{cm}(t)}{f_{cm}} = \frac{38}{53} = 0.717 \quad (22)$$

This value for $\beta_{cc}(t)$ can be inserted into the previous equation, using EC table 3.1 for f_{ctm}:

$$f_{ctm}(t) = \left(\beta_{cc}(t)\right)^{\alpha} f_{ctm} = 0.717 \times 3.8 = 2.72\ MPa$$

Now the design concrete tensile strength at time of tendon release $f_{ctd}(t)$ can be calculated:

$$f_{ctd}(t) = 0.7\alpha_{ct}\frac{f_{ctm}(t)}{\gamma_c} \quad (23)$$

With α_{ct} as the value stated in the National Annex, where 1.0 is the recommended value and γ_c is the partial safety factor for concrete at a value of 1.5
This gives $f_{ctd}(t) = 1.27\ MPa$
Now that this is known, this value can be inserted in the formula for bond stress:

$$f_{bpt} = \eta_{p1}\eta_1 f_{ctd}(t) \quad (24)$$

As stated before, a value for η_{p1} of 3.2 will be used, as 7-wire strands are used as the tendons, and η_1 is assumed to be 1.0, for good bond conditions. Bond stress becomes:

$$f_{bpt} = \eta_{p1}\eta_1 f_{ctd}(t) = 3.2 * 1 * 1.27 = 4.06\ MPa$$

With the bond stress known, formula 8.16 can be used to determine the transmission length:

$$l_{pt} = \alpha_1 \alpha_2\ \phi\ \sigma_{pm0}/f_{bpt} \qquad (25)$$

Where:

α_1 = 1.0 for gradual release and 1.25 for sudden release
α_2 = 0.19 for 3 and 7-wire strands
ϕ is the nominal diameter of the tendon, which is 12.9 mm
σ_{pm0} is the tendon stress just after release

For the tendon stress just after release, additional calculations must be made to account for prestressing losses, namely the immediate losses due to instantaneous deformation of the concrete (EC 2 Chapter 5.10.5.1), and relaxation loss of the pre-tensioning tendons (EC 2 Chapter 3.3.2 (7)).
To start with, initial prestressing force for the applied strands is found in documents to be 140 kN per strand. The initial prestressing stress is obtained by dividing this force by the area per strand (100 mm^2), giving an initial prestressing stress of 1400 MPa (σ_{pi})
With 16 strands, this means the initial, and at the same time, maximum prestressing force is:

$$F_{pi} = F_{pmax} = 16 \times 140\ kN = 2240\ kN \qquad (26)$$

Using the relaxation loss and the elastic loss as calculated in Eurocode 2, Chapter 3.1.2 and 3.1.3, the prestressing force is calculated. This gives:

$$F_{pm0} = F_{pmax} - \Delta F_{pr} - \Delta F_{pel} = 2240 - 16.2 - 200.2 = 2023.6\ kN$$

The tendon stress just after release becomes:

$$\sigma_{pm0} = \frac{F_{pm0}}{A_p} = \frac{2023.6\ kN}{1600\ mm^2} = 1265\ MPa$$

Now all values are known to calculate the transmission length using equation 25.
The formula for the transmission length can now be filled in:

$$l_{pt} = \alpha_1 \alpha_2 \phi \frac{\sigma_{pm0}}{f_{bpt}} = \ 1.0 \times 0.19 \times 12.9 \times \frac{1265}{4.06} = 763\ mm$$

This value for the transmission length is an estimation based on assumptions for regular concretes. Since the geopolymer concrete has different mechanical and material properties than regular concrete, the resulting transmission length can be different from measurements and observations made in the 2 girders.

4.2.2 FBG measurements

2.5 days after the concrete has been casted, the prestressing tendons are released. Measurements of the FBGs in 2 girders have been made right after prestressing. According to documentation, the span of the girder is 7 m. The positions of the FBGs will need to be determined, in relation to the respective distances from the edge of the beam. This is because transmission length is measured from where the tendons are applied: the edge of the beam.

The distances of each FBG to the edge are shown in Table 2. Relevant values are shown for specimen 2, the precast girder that is going to be used in a mock deck (Long 1), and specimen 4, the beam to be tested in a shear test (Long 2). The measurements done on the FBGs right after prestressing are shown in Figure 4-10, which shows the strain values vs the FBG position in the beam from the edge for both the Long 1, and Long 2 set of FBGs.

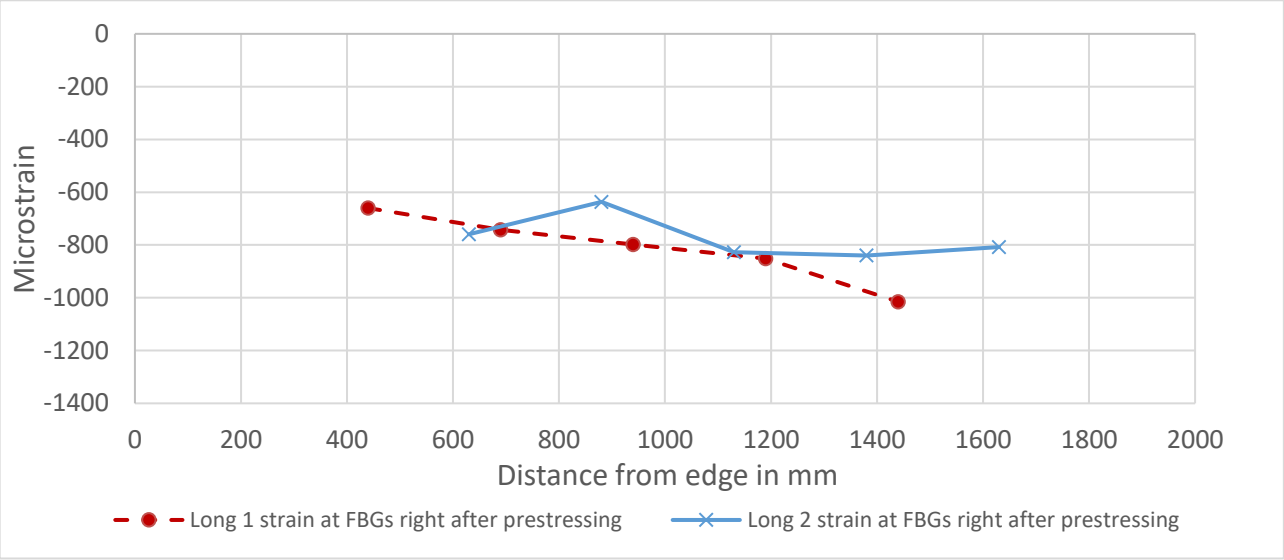

Figure 4-10: strain measurements performed on Long 1 and Long 2 after prestressing plotted along distance from the edge

To compare the measurements of the FBGs with calculations done to estimate the transmission length, the strain in the FBGs are compared with the theoretical strain of the concrete at the height of the FBG sensors. The FBG sensors are located in a bar of reinforcement placed at 100 mm from the bottom of the girder. This rebar should have the same stresses as the concrete at 100 mm from the bottom. The concrete is only affected by the prestressing force, and the moment due to its own weight. Because the moment is a parabolic function over the length of the girder, each FBG will have a different theoretical stress.

The effect of the transmission length also needs to be taken into account for FBGs located within 763 mm from the edge, as they will not have the full effect of the prestressing force. The prestressing stress right after release σ_{pm0} has a maximum value of 1264 MPa and will start at 0 MPa at the edge, and increases linearly to 1264 MPa at 763 mm from the edge. This is of course with the assumptions and calculations done before.

The effect of the own weight is a moment that is variable over the span of the girder. This moment can be summarized as a parabolic function that starts at 0 kNm at span = 0 m, this moment will reach a peak of M_{eg} = 21.99 kNm at halfspan, and ends at a moment of 0 kNm again at the other support. The parabolic function for the moment due to own weight at distance x from the support is determined to be (with x in mm and moment in kNm):

$$M_{eg}(x) = -1.795 \times 10^{-6}(x - 3500)^2 + 21.99 \quad (27)$$

This moment causes a different amount of stress across the height of the girder:

$$\sigma_{c,eg} = M_{eg}(x) \times z/I_{zz} \quad (28)$$

With z = distance from the centre of gravity, and I_{zz} = second moment of area of the girder. Because every FBG is located at 100 mm above the bottom of the girder, the distance from the centre of gravity is constant, at 110 mm-100 mm = 10 mm. The formula for stress due to own weight, with second moment of area = 1197×10^6 mm^4 becomes:

$$\sigma_{c,eg} = M_{eg}(x) \times 10/1197$$

This calculates the stress in concrete due to own weight at distance x from the support, at the height where the FBGs are located in the girder in N/mm^2 or MPa. Since the total length of the girders about 7350 mm, it is assumed the girder edge is positioned at 175 mm from the support on both sides.

The table including positions of FBGs in relation to the edge can now be filled in with positions related to the support, to calculate the stress due to own weight. Finally, the total stress will be determined by adding up the stress caused by prestressing at time = 0, which includes the compressive effect, and the stress caused by the moment that occurs due to eccentricity.

$$\sigma_{c,FBG} = \sigma_{ceg} + \sigma_{cpi,55} \quad (29)$$

With $\sigma_{cpi,100}$ being the concrete stress at 100 mm above the bottom of the girder, with initial prestressing levels: F_{pm0}

$$\sigma_{cpi,100} = -\frac{F_{pm0}}{A_p} - F_{pm0} \times \frac{\left(z_{cog} - 100\right)^2}{I_{zz}} \quad (30)$$

The maximum level of this concrete stress due to prestressing is reached when the transmission length is reached, meaning that the prestressing force is fully transmitted to the concrete over the transmission length, from the edge. FBGs that are located within the transmission length, will have the same stress as the concrete at that level. Since the stress increase is linear until the transmission length is reached, the concrete stress due to prestressing at these FBGs can simply be calculated by dividing the location of the FBG from the edge of the girder, by the transmission length. This fraction can then be multiplied with the maximum concrete stress due to prestressing, which occurs from the transmission length onwards, to obtain the stress at the FBGs for girder Long 1 and Long 2.

Now that the theoretical stresses due to own weight and prestressing at the FBGs are known, the strains can be calculated by dividing the stresses by the elastic modulus of the concrete. This can be done as the rebar has the same strain as the concrete at that level, as long as the concrete is uncracked, assuming an elastic modulus for the concrete of 24000 MPa at time of prestressing:

$$\epsilon_c(x) = \sigma_c(x)/E_c \quad (31)$$

To compare these theoretic values with the measurements of the FBG, some unknown factors must be accounted for, since the measurement includes strain due to shrinkage and creep. To minimize the effect of shrinkage, the difference in strain measured is taken from a measurement right before prestressing, and a measurement right after prestressing. However, measurements done after prestressing were done in roughly 2 or 3 hours after prestressing has been applied. This does minimize the effects of shrinkage in that time, but in these few hours before the measurement, the effects of creep caused by this prestressing force is not negligible.

In lab tests, done by members of the Microlab of TU Delft. The creep has been tested on samples with a stress of 17 MPa as seen in Figure 4-5. Since this is the only experimental data that is applicable to the FBG measurements, these creep test results are applied to the FBG data to compensate for creep that occurs in the few hours between prestressing and measuring. With the data from the lab tests, a value of 150 microstrain is chosen to be sufficient to compensate for the creep.

Due to the characteristics of the precast girder, however, another set of compensations has to be made. This is due to the fact that FBGs overlap with cross sections where concrete area is missing. This is because there are gaps every 250 mm in the length of the girder, to allow for shear reinforcements to pass through. These gaps can be seen clearly in the formwork before casting in Figure 4-11. A cross section of the girder at the location of the gap can be seen in Figure 4-12 with the red outline. It has a slight inclination while moving towards the middle of the cross section, which can also be seen from the picture. At the cross section with a gap, the concrete cross sectional area changes, along with the second moment of area, and the centre of gravity of the section. This all has an effect on the stresses and thus, the strains measured by FBGs that are overlapping the locations of these gaps.

Figure 4-11: Picture of the precast girder formwork prior to casting

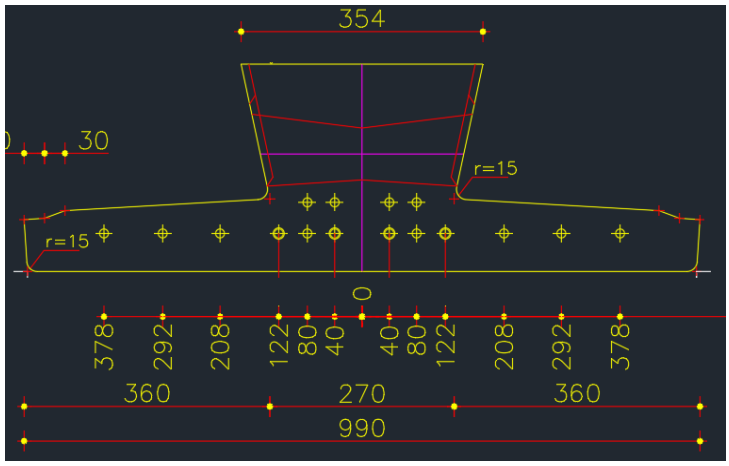

Figure 4-12: Cross section of the girder as visible in AutoCAD (units in mm)

Hand calculations have been performed, calculating the new centre of gravity to be 97 mm from the bottom of the girder, from 110 mm of the complete cross section. The cross sectional area decreases from 156085 mm^2 to approximately 129×10^3 mm^2. Lastly, the second moment of area decreases from 1197×10^6 mm^4 to approximately 1050×10^6 mm^4. The sensors of Long 1 are coinciding with the gaps, so these measurements must be compensated for slightly. Firstly, the stress in the entire cross section goes up, due to less concrete area to divide the prestressing force over. Secondly, the stress caused by moments change due to a change of location of centre of gravity, and the change in second moment of area.

The calculations have found the impact of these gaps to be about 85 microstrain at FBG level (100 mm from the bottom of the girder), which is about 15% higher than the stresses and strains at the same FBG level but without the gaps. This effect is smaller near the edge of the beam due to the effect of transmission length on the stress development in the girder. This is more difficult to approximate, because the actual transmission length is yet unknown. The current approximation is to assume a linearly increasing effect from 0 at the edge, to 100% when the theoretical transmission length of 763 mm is reached. The same has been applied to the creep effects on the measurements. This results in the following graph, showing the difference between measurements done right before, and right after casting, with adjustment for the gap, as seen in Figure 4-13:

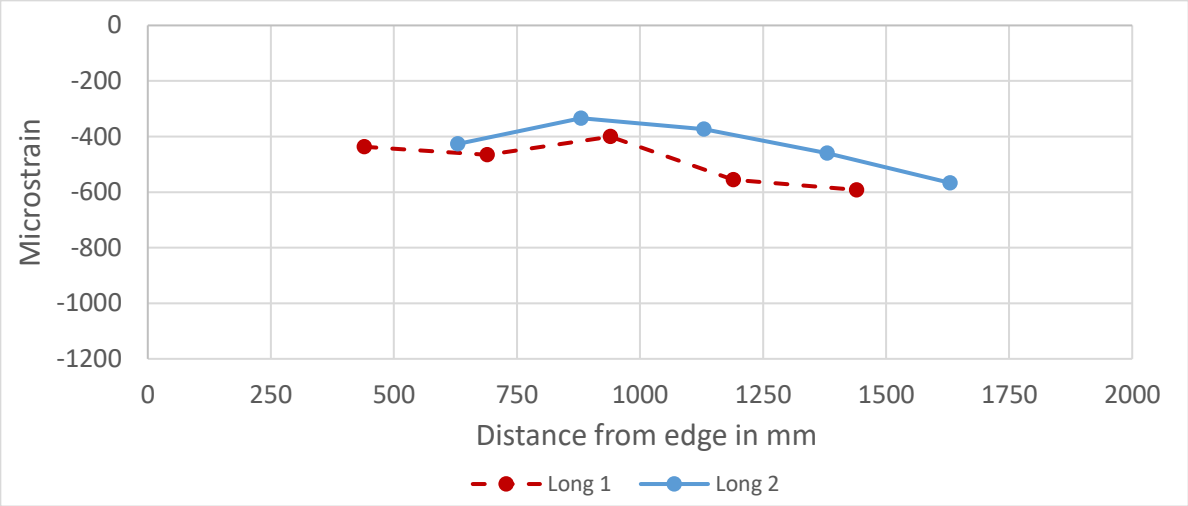

Figure 4-13: Measured FBG strains in Long 1 and Long 2 due to prestressing forces, adjusted for gaps and creep

4.2.3 Bending girder data points

To further analyse the data collected on transmission length, the measurements of the shear beams (Long 1, Long 2) are compared with measurements from 2 sets of FBGs that are inserted into different girders, intended to be tested in bending: Short 1, Short 2. These FBGs are located near the middle of the girder span, this allows for measurements without the influence of transmission length, as the distance from the measuring points to the edge of the beam far exceeds the (theoretical) transmission length.

A short summary of the results following FBG measurements on rebars Short 1 and Short 2 is shown, based on calculations following only the effect of prestressing stress, calculated the same as the shear girder FBGs. Both Short 1 and Short 2 FBGs intersect with gap locations, and the measurements are adjusted appropriately. Similarly, the FBG measurements have been adjusted for 150 microstrain of creep. In Figure 4-14 is a graph showing the difference of the measurements after prestressing, and the measurements before prestressing.

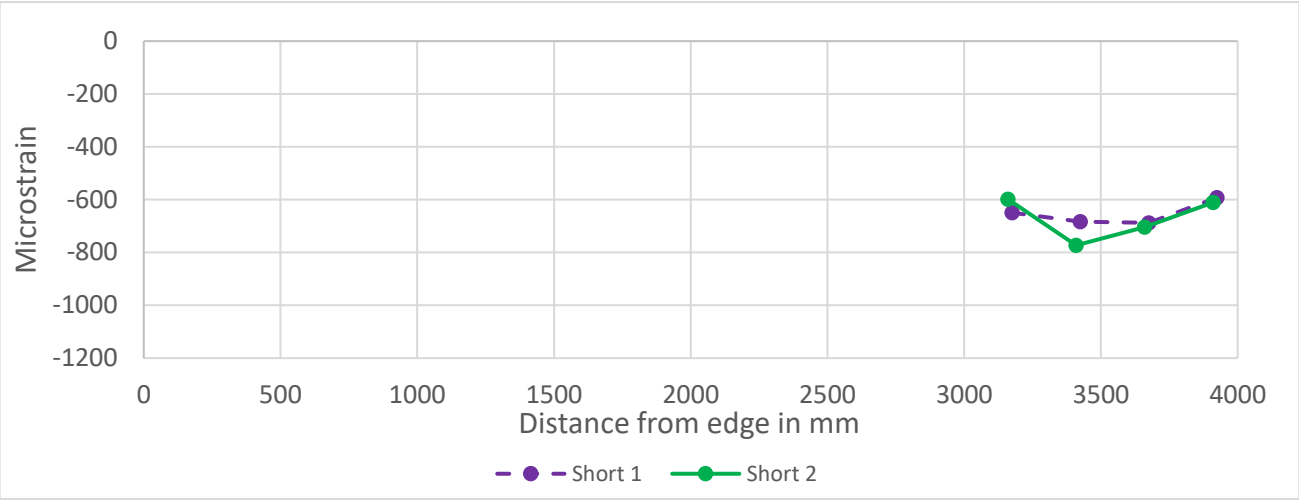

Figure 4-14: FBG measurements from Short 1 and Short 2, due to prestressing only, adjusted for creep and gaps

4.2.4 Theoretical predictions

Now that all data points are gathered, they can be inserted into a single graph to compare. A plot can also be made, following the calculations on expected strain in the concrete at 100 mm above the bottom of the girder. This expected strain will include the effects of prestressing and the effect of own weight.

For locations that are within the transmission length, the strain is assumed to be linearly increasing from 0% at the edge, to 100% at a distance away from the edge, equalling the transmission length. Notable is how 4 strands are unbonded for the first 1000 mm, the theoretical prediction line has been adjusted for these strands, that only start contributing from 1000 mm from the edge. The first 1000 mm, 12 out of 16 strands will be active and thus, only 3/4th of the prestressing is active. The results are visible in Figure 4-15.

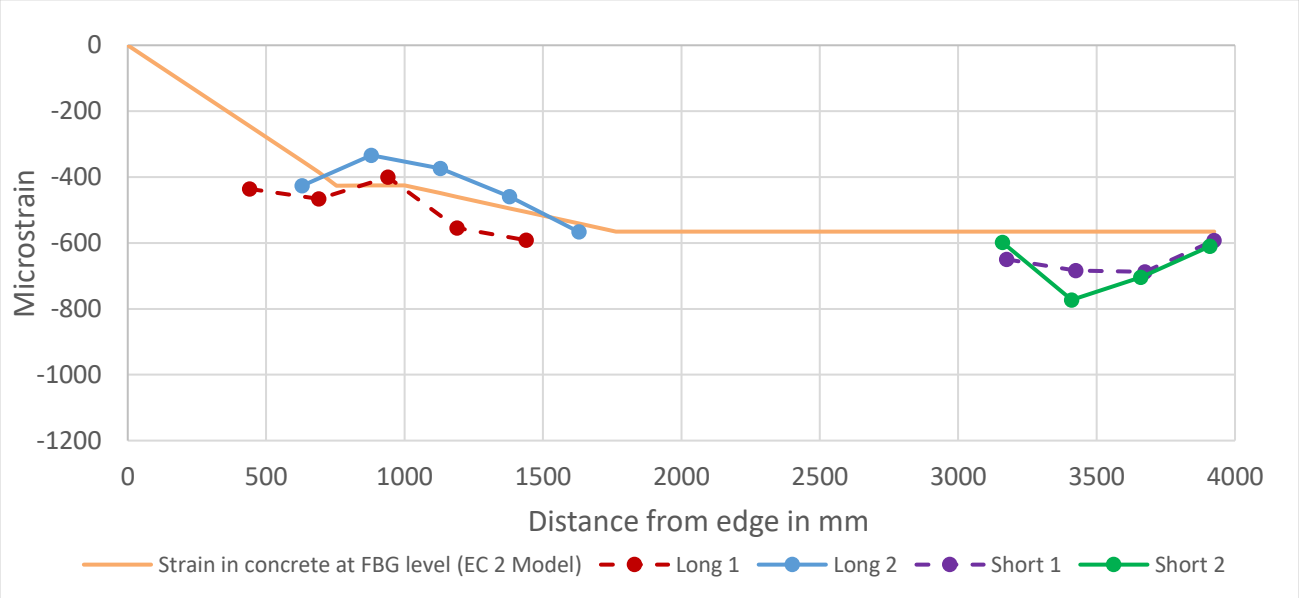

Figure 4-15: Strain increase in precast girders due to prestressing only, plotted versus the prediction following Eurocode calculations. Eurocode calculations adjusted for gaps, all data adjusted for creep and gaps.

The measurements regarding change of strain over time has also been processed with the creep effect in the prestressing measurement and gaps in the girders. This is to check for any large inconsistencies in changes of strain that could have occurred during curing that could impact the transmission length. The increases in strain look to be in line with what is expected as visible in Figure 4-16 and Figure 4-17. None of the strain increases are inconsistent, and can be attributed to the occurring creep. Strain measurements closer to the edge experience less strain developing over time, as these have less compressive stresses transferred from the steel, as expected.

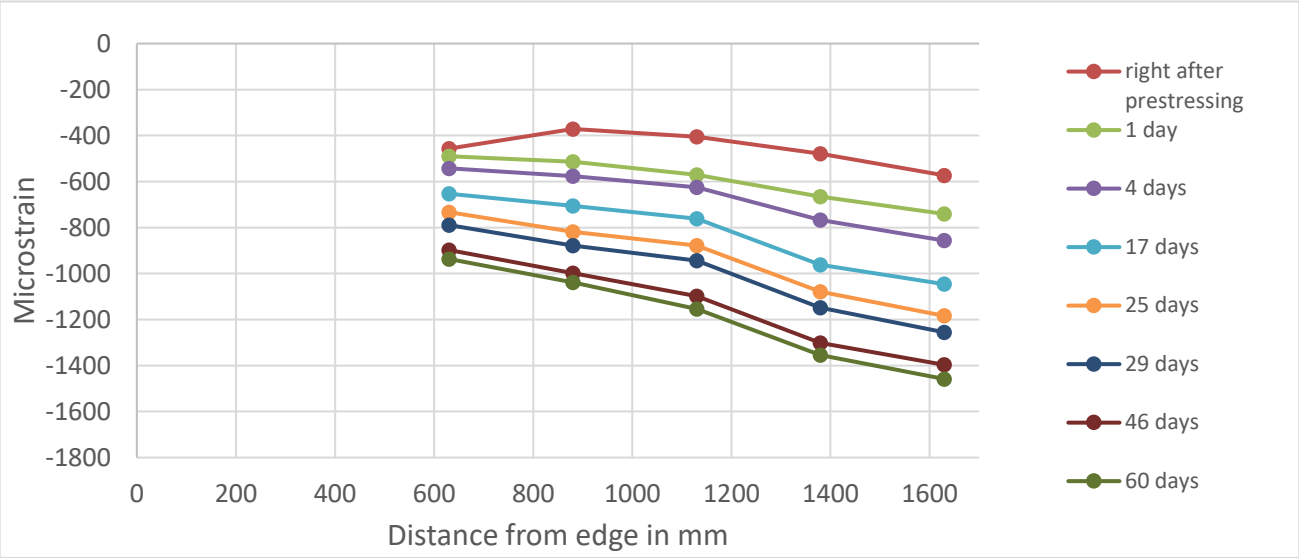

Figure 4-16: Measured strains in Long 1 rebar after prestressing. Creep effect between prestressing and moment of measurements, and gap effect have been accounted for

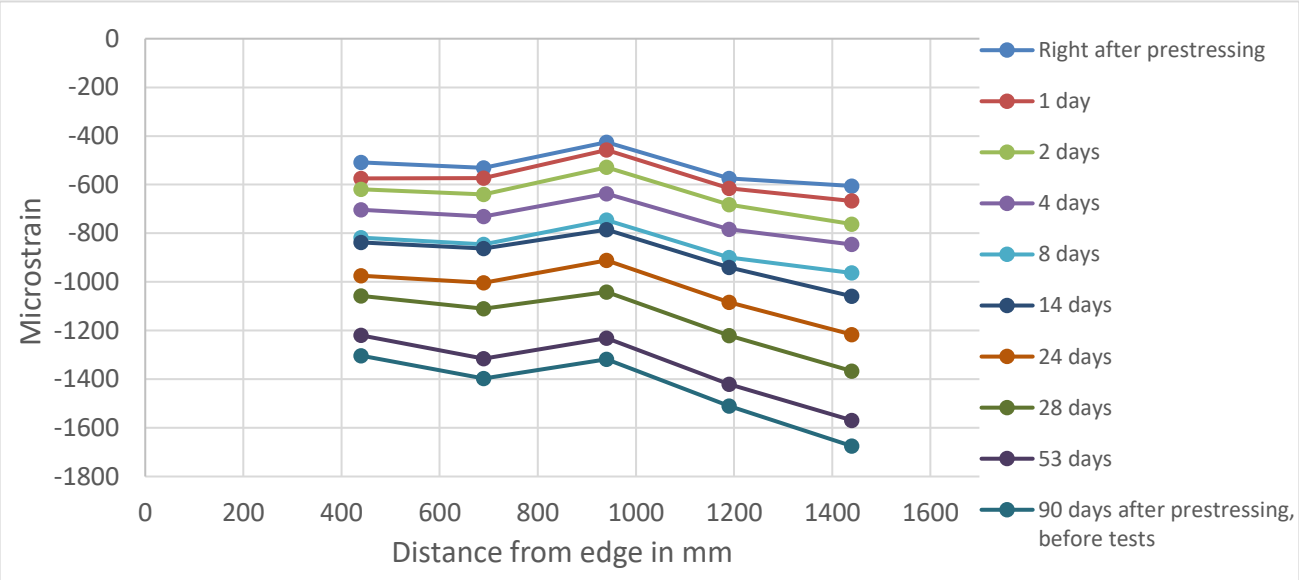

Figure 4-17: Measured strains in Long 2 rebar after prestressing. Creep effect between prestressing and moment of measurements, and gap effect have been accounted for

4.2.5 Discussion

As can be seen from the combined graphs in Figure 4-15, the measured transmission lengths in Long 1 and Long 2 seem following the prediction line. Nothing concrete can be said from the apparent transmission length from the measurements, but it seems to be trending to be equal or larger than the transmission length as calculated by Eurocode 2 with combinations of assumptions.

The difference in measurements versus theory can be explained partially by these assumptions. Formula 8.16 in Eurocode 2 determines the transmission length, also equation 25 in this document:

$$l_{pt} = \alpha_1 \alpha_2 \, \phi \, \sigma_{pm0} / f_{bpt}$$

Where:

α_1 = 1.0 for gradual release and 1.25 for sudden release
α_2 = 0.19 for 3 and 7-wire strands
ϕ is the nominal diameter of the tendon, which is 12.9 mm
σ_{pm0} is the tendon stress just after release
f_{bpt} is the bond stress

The bond stress is calculated using a formula that is normally used for OPC- based concretes to be 4.06 N/mm^2, TU Delft Microlab has done tests on the bond stress on 1-day old specimens and 28-days old specimens. The results are in Figure 3-16. The assumed bond stress of 4.06 N/mm^2 at time of prestressing (2.5 days old) is not far away from the experimental values. The pull-out test data in combination with the results of the transmission length analysis using the bond stress as calculated by EC2 methods suggests that the occurring bond stress in this SCGC mixture is similar to bond stresses of OPC based concretes.

However, more data is needed in the longitudinal axis of the girder, as the measured strain in the sensors at the edge of the girder does not seem to flatten out when comparing to the strain measured by sensors in the middle of the girder span. The apparent transmission length could be similar to OPC-based concretes or larger.

Eurocode 2 does not take into account an effect of self-compacting concretes or light-weight concretes, this geopolymer concrete mixture being part of the former. Self-compacting concretes have shown to have a higher transmission length when compared to more conventional types of concrete. (Peterman, 2007). To add to that, silica fume contents in concrete have a significant influence into the rigidity of the connection between concrete and steel. (Derkowski & Dyba, 2017). There is a lot of explanations that can account for the apparent difference of transmission length in these geopolymer concrete girders when compared to Eurocode 2 calculations of transmission length in more conventional concrete types.

Additional sensors in the Long 1 and Long 2 set of FBGs, and a longer rebar could have provided more insight in the development of strain as the measurements go further inside the girder. The analysis has also been performed using data from two girders, more samples can help in gaining more knowledge into the apparent transmission length in structural elements made of this SCGC mixture.

4.3 Flexural testing

4.3.1 General

The flexural test (4-point bending) has been performed on specimen 3, 56 days after casting. The loading and unloading speeds are 10 kN/minute load control at the beginning and separated into three phases: The first phase sees loading until an average load of 10 kN per piston (load F), and unloading for the initial checks. There are no FBG measurements during this. The second phase sees loading from 0 to 130 kN and back to 0, with pauses at 10 kN, 40 kN, 70 kN, 100 kN and 117 kN for measurements. The setup is then unloaded to 0 kN before phase 3. This sees loading until 130 kN without stops, and then loading until 280 kN under load control, with stops at 160 kN, 190 kN, 220 kN and 250 kN. Between 280 kN and 330 kN, displacement control with a load speed of 2 mm/minute has been applied. Finally, from 330 kN until ±390 kN, which was the end of the piston stroke at 125 mm, a load speed of 4 mm/minute was applied.

The load vs time graphs of phase 2 and 3 can be seen in Figure 4-18 and Figure 4-19, featuring the synchronised FBG measurements. Notable is that some data is missing, this is due to pausing the FBG measurements in the lengthy breaks in the loading procedure. In some cases, the communication was not optimal, so some data is missing, during loading from 100 to 117 kN for example.

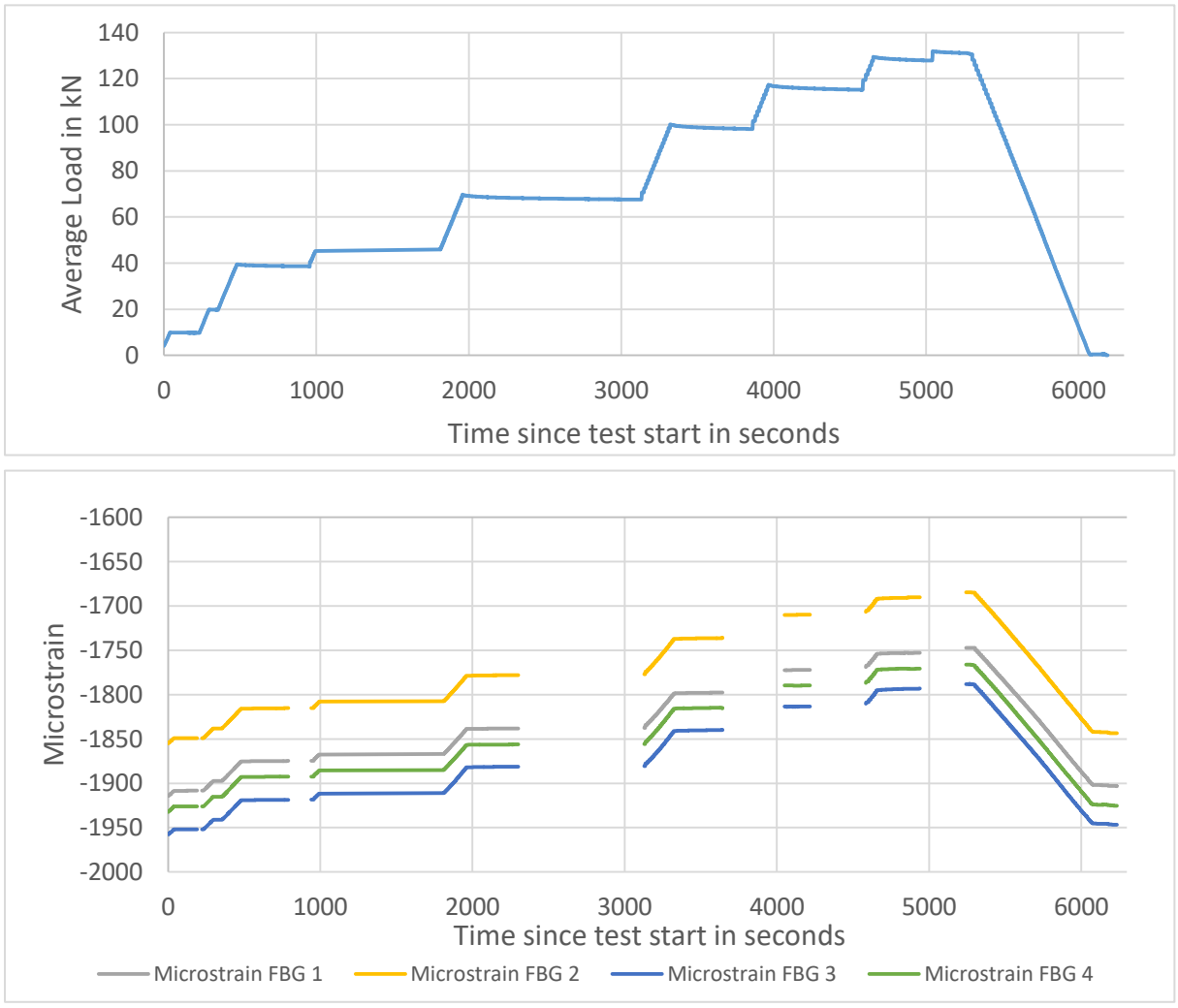

Figure 4-18: Flexural test phase 2 graphs. Top: Load vs. Time graph. Bottom: Short 2 FBG data

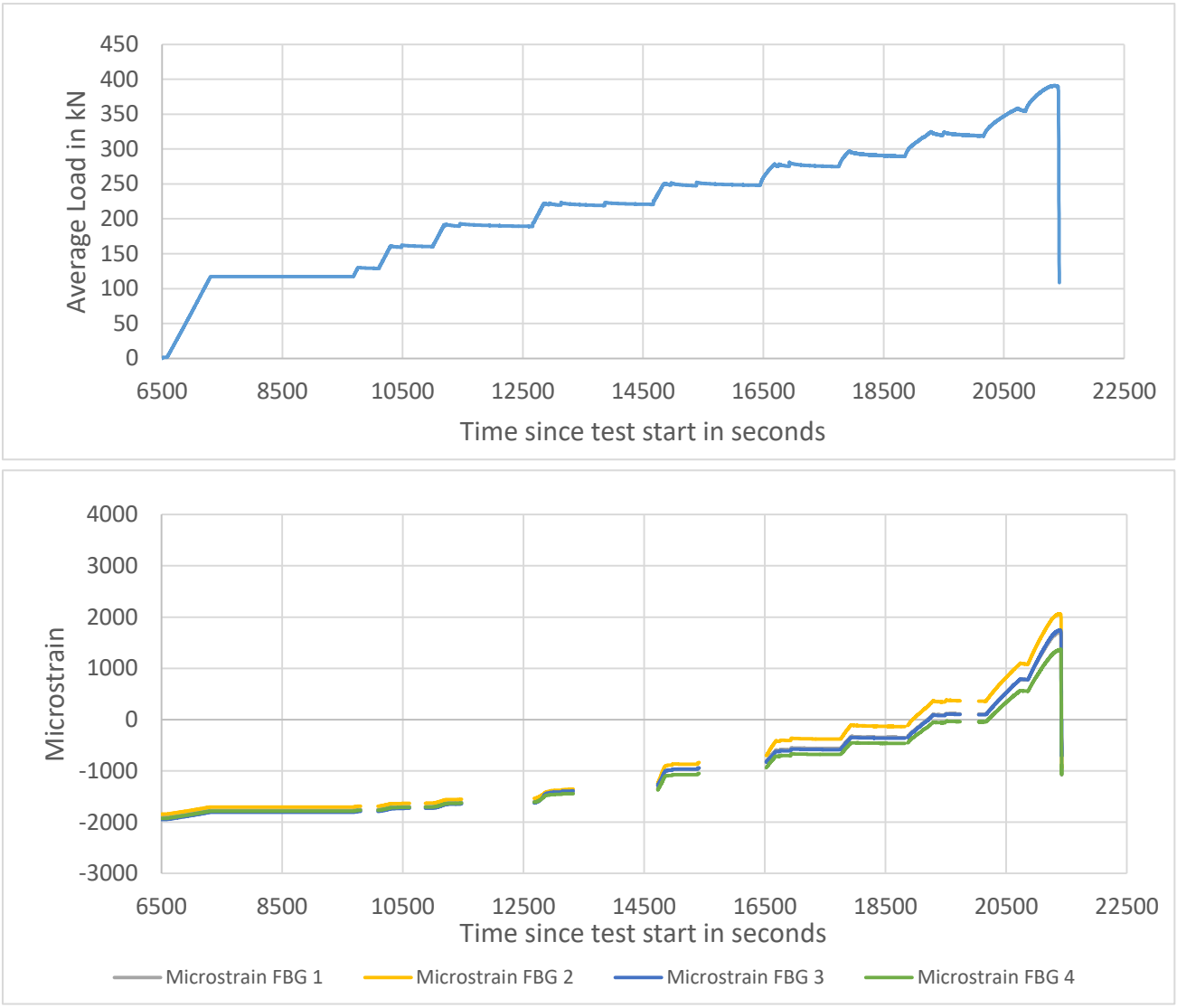

Figure 4-19: Flexural test phase 3 graphs. Top: Load vs. Time graph. Bottom: Short 2 FBG data

During the later stages of phase 3, at 250 kN and above, the choice was made to run the FBG measurements continuously at 250 Hz, with a break at 320 kN due to adjusting the measuring windows. As mentioned before, the test was halted at ±390 kN of piston load, because the maximum stroke was reached. The FBG measurements at the end are the result of the rapid unloading as seen in the load vs. time graph, as FBG measurements went haywire due to the change in strain being too large to track in the measuring window. Since the first (minor) crack has been spotted at 117 kN, and minimal cracking occurs between 117 kN and 130 kN. The data of the first 120 kN of loading in both phase 2 and 3 have been used for linear calculations, such as the in-situ E-modulus as presented in Chapter 4.3.3. The data beyond this point is used in a nonlinear analysis regarding expected strain that is measured in the rebar by FBGs, compared to the actual data, in Chapter 4.3.6.

Before these analyses can be performed. The apparent E-modulus of the concrete near the FBGs has to be determined. This can be done by fitting the FBG data during the linear stage of the test, before any significant cracking happens, to a linear model, relating the increase in force to an increase of strain. In the linear phase, the strains measured by FBGs is still equal to the strain in the concrete around it. The initial cracking also do not affect the FBG measurements by much, as there are no significant jumps seen in the measurements when the first cracks were reported at 117 kN and 130 kN.

But first, the effect of the composite concrete cross section is evaluated, the second moment of area of the composite cross section is needed to analyse the in-situ E-modulus.

4.3.2 Girder composite cross section E-modulus, second moment of area

The entire cross section is divided into the precast girder, and the cast-in-situ topping. Since these two concretes have a different E-modulus at time of testing, this has to be taken into account when calculating/estimating the second moment of area in the entire section.

The precast girder is 59 days old, and the topping is 30 days old at time of the flexural test. First off, the precast girder is made at Haitsma Beton using the TU Delft SCGC mixture. Tests done by Microlab on this mixture have samples of this mixture heat cure at 25°C for one day, moisture cure at 20°C and 95% relative humidity for 7, 14 or 28 days before getting exposed to drying conditions at 20°C and 55% relative humidity, as seen in Figure 3-14. Results have an upper bound of around 30 GPa for samples that are kept in moisture curing conditions, and a lower bound of around 22-23 GPa for samples exposed to drying after 7 days of curing. The precast girder itself is wrapped with a wet burlap cloth and sealed for 14 days after casting. Therefore, an upper bound of 30 GPa is assumed, while a lower bound of 25.5 GPa is assumed, following the test results for samples with drying conditions starting after 14 days of curing.

The E-modulus of the topping, which is a ready-mix geopolymer concrete (C30/37) is experimentally tested by J.E. Paredes Pineda in a Master Thesis (Pineda, 2022) Prisms of 100x100x400 mm are collected and tested at TU Delft. Plots summarizing the test results are shown in Figure 3-15. During this experiment, seven samples of the concrete are subjected to different curing conditions. The most relevant is the curing regime of sealing for 14 days and then subjected to drying conditions. At an age of 30 days, this sample has an E-modulus of approximately 26 GPa. When considering the lower bound E-modulus of the precast girder at 25.5 GPa and 26 GPa for the cast topping. They are assumed to be equal enough to not have a significant impact on the second moment of area of the combined section, as the ratio between the girder and the topping is equal to 1.02, which is close enough to 1.0. The unmodified combined section has a total area of 453.3×10^3 mm^2 and a second moment of area of 652×10^6 mm^4. For the upper bound of the girder E-modulus at 30GPa, the ratio is as follows: $n = E_{topping}/\ E_{girder}$ = 26/30 = 0.87.

In the concrete cross section, the width of the topping is transformed using the factor n = 0.87. Slices of the topping concrete are transformed by multiplying the width by 0.87. The cross section is then rebuilt and analysed for new geometry properties, the details can be found in Appendix C.

After the cross section has been transformed, the total concrete area is around 4.12×10^5 mm^2. The second moment of area is 600×10^6 mm^4, which is 9% lower than the second moment of area with equal E-modulus for topping and girder. The centre of gravity also shifts down by 5 mm: from 214 mm to 209 mm from the bottom of the girder, this has an effect on the stress distributions.

4.3.3 E-modulus

To approximate the apparent E-modulus of the geopolymer concrete near the FBG positions, the linear parts of the bending test were used, as the effect of cracks is either not present at all, or minimal at a force below 120 kN. The measured change in strain in the FBGs are fitted against an expected change in strain following a certain change in load. The approximations are done for both cross sections. First with the unchanged cross section following: $E_{topping} = E_{girder}$. The second set of approximations will assume $n = 0.87$:

$$\Delta\sigma = \frac{\Delta M \times z}{I_{zz}} = \frac{\Delta F \times 2300mm \times z}{I_{zz}} \quad (32)$$

Using the linear relation between stress, strain and E-modulus, the equation becomes:

$$\Delta\epsilon = \frac{\Delta\sigma}{E} = \frac{\frac{\Delta F \times 2300mm \times z}{I_{zz}}}{E} \quad (33)$$

The formulas above have been used to calculate the change of stress at the location of the FBGs, following a change in moment, caused by the external force. This is plotted on the vertical axis. The strain, or in this case, microstrain will be plotted on the horizontal axis. The measurements will be plotted in the same graph with an expected change in strain following a static E-modulus.

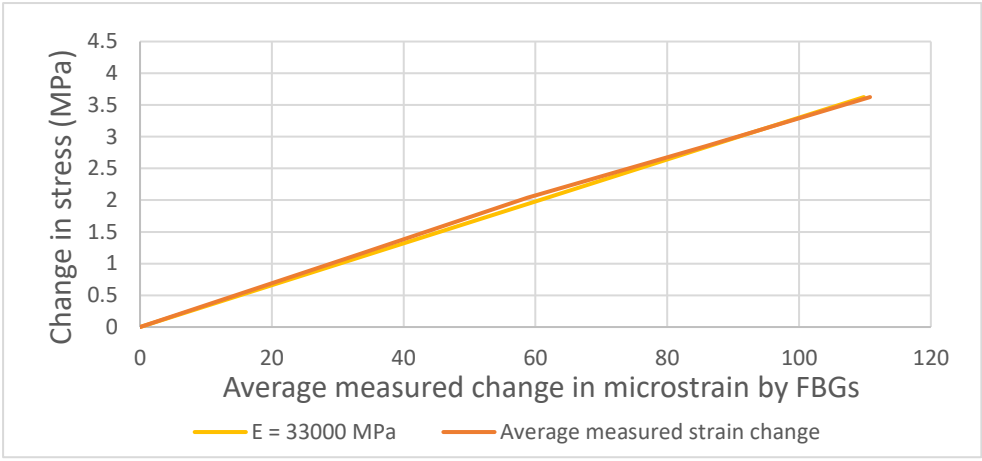

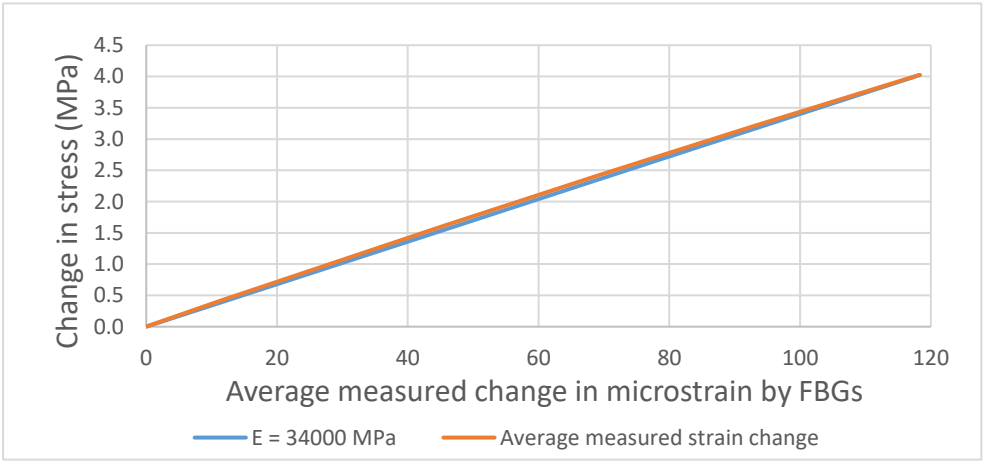

Figure 4-20: Strain measurements vs Stress increase during Flexural tests, fitted with E-moduli.
Top: Phase 2 of flexural test with a 33 GPa E-modulus fit. Bottom: Phase 3 with a 34 GPa E-modulus fit

The bending test was done in separate phases. The second phase sees the force increase from 0 to 130 kN with several pauses in between to account for measurements of other projects. The third phase sees a direct force increase from 0 to 130 kN following unloading of the first stint.

The graph of the second phase has a missing part compared to the third phase. The reason is that the first 10 kN of measurements are not accurate enough, as the external force was applied before the FBG measurements started. This should not impact the approximations by much, as the change in stress is plotted against the change in strains rather than absolute values. In phase 2, the base measurement is an external force of 10 kN, rather than 0 kN, and the last measurement to compare the change in force to, is at 120 kN. That is why the graph of the third phase has an extension.

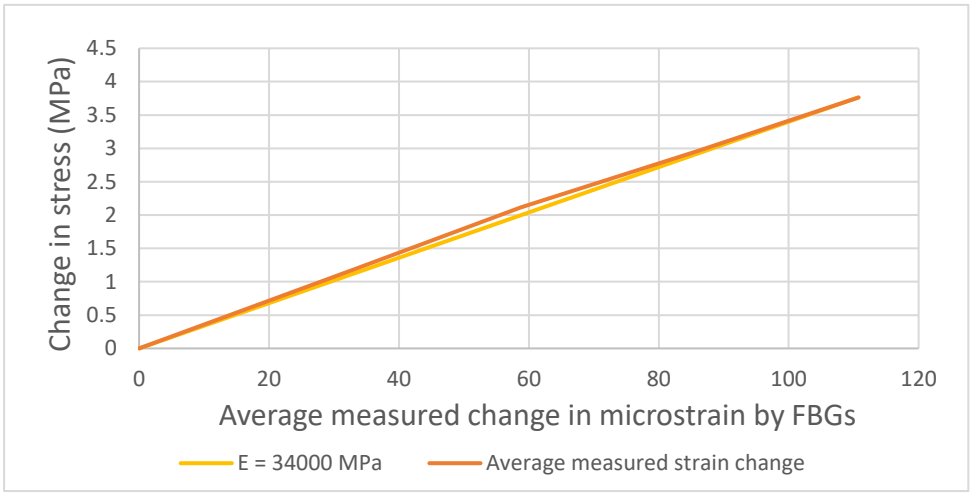

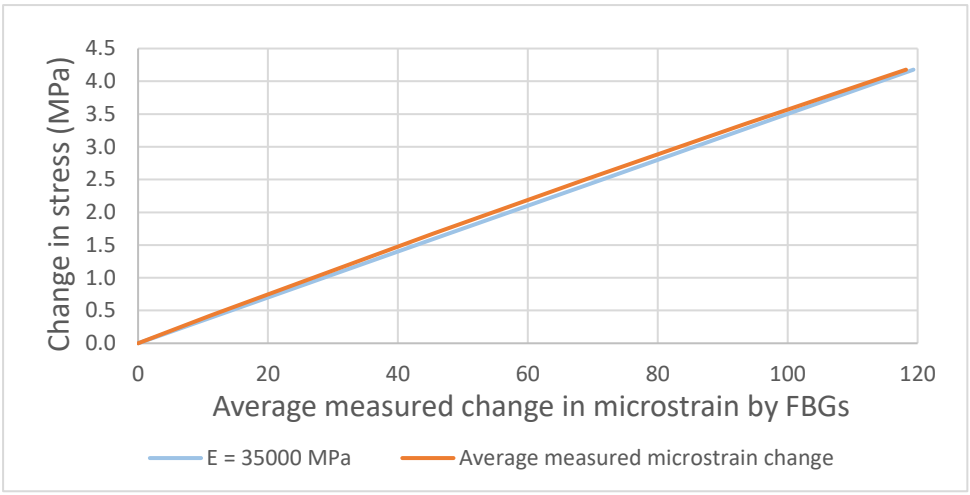

Figure 4-21: Strain measurements vs Stress increase during Flexural tests, applied using the modified cross section. Top: Phase 2 of flexural test with a 34 GPa E-modulus fit. Bottom: Phase 3 with a 35 GPa E-modulus fit

With the assumption of $E_{topping} = E_{girder}$, the range of elastic modulus is between 33 GPa and 34 GPa. This process is now repeated, but for $E_{topping} = 0.87E_{girder}$, this changes both the centre of gravity of the beam for the calculation of the change in stresses, and the second moment of area of the beam. The best E-modulus fits are presented in Figure 4-21. A range of elastic modulus between 34 and 35 GPa is measured in the FBG. This is with the assumption that $E_{topping} = 0.87E_{girder}$.

Combining the results of all fitted E-moduli, the range of 33 to 35 GPa is highly likely to be effective in the concrete near the FBGs. This experimental range in E-moduli is now compared with values from lab tested samples. This range of 33 to 35 GPa is above the range tested in the initial lab tests done by Haitsma. As seen in Figure 4-22, the range of E-modulus depends on the curing method used, ranging from 23 GPa where a specimen is exposed to drying conditions, to 31 GPa for a specimen that is cured without drying.

There is a difference in the result of the FBG measurements during the bending test and early lab tests. One of the reasons could be the aggregates used in the different setups. The girder has been made using crushed aggregates, whereas the initial lab tests were performed on a concrete using pebble aggregate. The composition of the aggregates of the topping are unknown.

For comparison, the Eurocode 1992-1-1 formula for approximating the E-modulus in OPC concretes is used. Eurocode 1992-1-1 Chapter 3.1.3 uses this formula for E-modulus, the girder is a C45/55 geopolymer concrete which results in a modulus of elasticity at age of 28 days of 36.3 GPa:

$$E_{cm} = 22(f_{cm}/10)^{0.3} = 22 \times \left(\frac{53}{10}\right)^{0.3} = 36.3\ GPa \quad (34)$$

This formula is generally used for OPC concretes. As expected, it overestimates the elastic modulus when applied to this geopolymer concrete mixture.

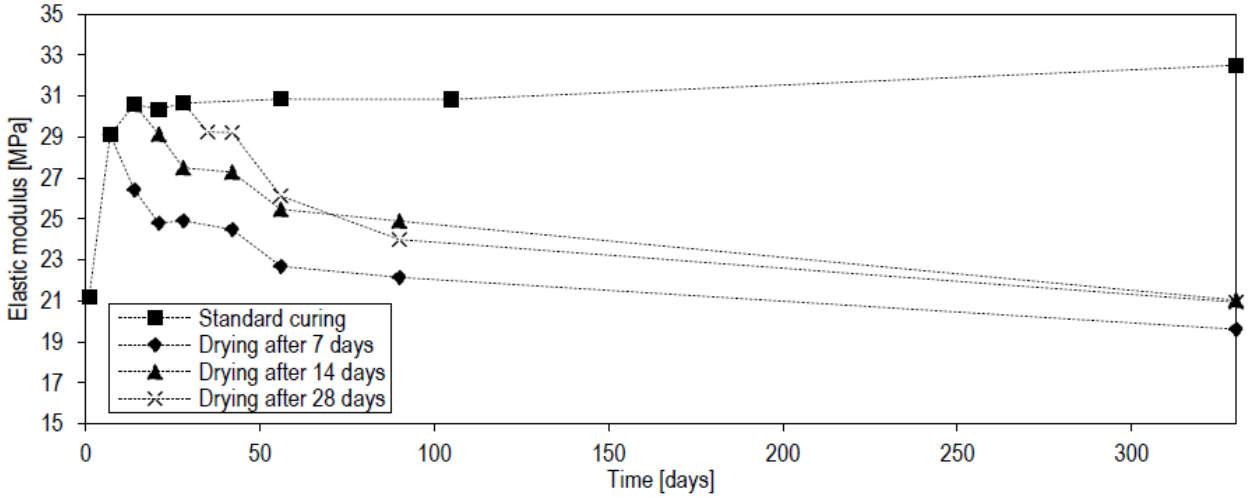

Figure 4-22: Lab tests performed by Haitsma Beton on the change of E-modulus over time of the SCGC mixture (Pineda, 2022)

The range of 33 GPa to 35 GPa calculated following the FBG measurements does seem possible. Comparing to the different lab tests, the higher E-modulus near the FBGs can be attributed to several factors. As mentioned before, the usage of pebble aggregates versus crushed aggregates can impact the E-modulus of concrete. Also, concrete in the core of the girder, where the FBGs are located, experience a limited amount of drying effects, resulting in a higher perceived E-modulus compared to concrete that is exposed to a drying environment.

In the analyses regarding the FBG measurements of the bending test, an E-modulus of 35 GPa will be assumed for calculations in combination with a lower second moment of area (6004 $\times 10^6$ mm^4), and a lower location of the centre of gravity, following the assumption that the ready-mix geopolymer concrete topping has a lower E-modulus compared to the precast girder due to being exposed to drying conditions after 14 days. For the behaviour of the entire girder, data from the LVDT used at midspan can be applied to estimate the apparent elastic modulus of the composite girder. The LVDT measures the deflection at midspan, and can be seen in the figure below, during the linear elastic stage of the flexural test:

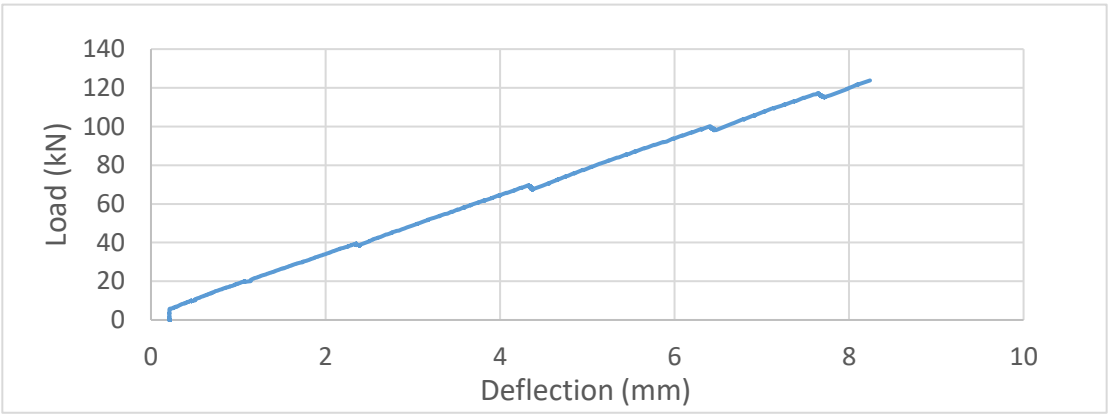

Figure 4-23: Deflection midspan measured by LVDT during linear elastic stage of 4-point bending test

At a piston force of 121.68 kN, a deflection of 8.1 mm was measured. The formula for deflection of a beam is applied from beam theory:

$$w(x) = \frac{F \times a}{6EI} \times (3Lx - 3x^2 - a^2) \qquad (a \leq x \leq L - a) \qquad (35)$$

The test setup has a span L of 7 m, and the distance from the applied force to the support a is 2.3 m, the location of interest is midspan, 3.5 m from the support. Simplifying the formula for deflection at midspan, the E-modulus can be approximated.
This is done using both scenarios of $n = 0.87$ and $n = 1.0$.

$$deflection\ midspan = w\left(x = \frac{1}{2}L\right) = \frac{F * a}{24EI} \times (3L^2 - 4a^2) \qquad (36)$$

The values for the second moment of area of both scenarios are inserted to obtain the following values for the E-modulus:

For $n = 1.0$, I = 6.52×10^9 mm^4: E = 27.8 GPa
For $n = 0.87$, I = 6.0×10^9 mm^4: E = 30.2 GPa

These results are lower than the E-modulus as estimated by FBG measurements as expected. The overall behaviour of the girder is affected by the lower E-modulus due to drying of concrete, whereas the concrete near the FBGs seems to have minimal deterioration of the E-modulus.

4.3.4 Estimation of cracking load

Using the previously estimated prestressing losses, the cracking moment during the flexural test can be approximated. The stress in the bottom fiber of the girder at midspan during the four-point bending test is evaluated using the following parameters/data:

Average concrete tensile strength f_{ctm} = 2.4 N/mm^2
Prestressing force remaining at time of testing = $F_{p,test}$ = 1647 kN
Total area of concrete cross section = A_c = 453292 mm^2
Self weight spreader beam HEM600 = 280 kg/m ×1 m wide (roughly) ×9.81 m/s^2 = 2.75 kN
Self weight girder = $q = A_c \times \rho$ = 10.43 kN/m, using ρ = 23 kN/m^3 (assumption)
Maximum moment due to selfweight = in middle at $\frac{1}{8}ql^2\ with\ span\ l = 7\ m$ = 63.8 kNm
Moment in middle section due to spreader beam = 2.75 kN × 2.3 m = 6.3 kNm

The second moment of area and centre of gravity of the composite cross section depends of the ratio n that is assumed. Both the regular cross section and transformed cross section are checked for cracking load in 2 scenarios. Scenario 1 is for For $n = 1.0$, scenario 2 is for For $n = 0.87$. The stress in the bottom fiber due to the axial component of prestressing, and the eccentricity is calculated using z_{cog} = 214 mm, A_c =453.3×10^3 mm^2 and I_{zz} =652×10^6 mm^4 for scenario 1, where the cross section is not transformed, and z_{cog}= 214 mm, A_c = 412×10^3 mm^2 and I_{zz} =600×10^6 mm^4 for scenario 2.

$$\sigma_{bot,p} = -P_{test} \times \frac{1000}{A_c} - (F_{p,test} \times 1000 \times (z_{cog} - 66.25) \times z, cog))/\, I_{zz} \quad (37)$$

The weight of the spreader beam, the self weight of the girder, and the applied piston force contribute towards the tensile stresses that occur in the bottom fiber. This results in the following formula to approximate the piston force needed to crack the girder, using the distance between the working line of the piston force and support = 2.3 m, units of the moments is in kNm:

$$F_{piston} = \left(\left[\sigma_{bot,p} - f_{ctm} \right] \times \frac{I_{zz}}{z_{cog}} - \frac{M,eg + M,spreader}{10^6} \right) / \, 2.3/10^6 \quad (38)$$

This results in F_{piston} = 155.2 kN for scenario 1, and F_{piston} = 147 kN for scenario 2. The resulting piston forces are both higher than the observed cracking load of 117 kN, where the first minor crack was spotted. This could be due to multiple factors, including underestimation of prestressing losses, overestimation of the tensile strength, and the inhomogeneous behaviour of concrete in general, where the weakest point in the area of interest crack first. However, this is only up to a certain extent, as multiple new cracks were reported at 130 kN.

The most likely major contributor is the effects of drying. The cracking load estimations are based on measurements of the FBGs, these are representative of concrete in the core of the girder, where effects due to drying are limited. The location of the first crack, at the bottom of the girder, is subject to drying conditions and is most likely to experience a higher level of drying shrinkage, on top of a decrease of the elastic modulus due to drying. This leads to a lower initial cracking force than expected.

For more insights into the behaviour of uncracked concrete, a linear analysis is performed to estimate the strains that occur at FBG level, and compared with the collected strain data.

4.3.5 Linear calculations on uncracked section

During the first part of the flexural test on the singular girder with the FBG sensors belonging to Short 2, measurements have been obtained and processed. The measured strains increase, as the load applied on the girder increases. To validate the data, a linear model has been created using the following assumptions:

- Second moment of area = 6.0×10^9 mm4
- Prestressing loss = 377 kN
- E-modulus at time of testing at FBGs = 35 GPa

For a non-cracked section, stresses in the cross-section originate from the following:

- Moment due to own weight and external force
- Prestressing forces, axial
- Prestressing moment due to eccentricity

The only variable in these stresses is the moment due to the external force, this follows from the increase in external force due to the loading jacks. Since the centre of the force is located at 2.3 m from the supports on both sides, the moment created by the force is equal to the force multiplied by the arm of 2.3 m. And because all FBGs are located in the active field of the constant moment, as created by the four point bending test, these stresses and moments combine to create a stress distribution over the height of the section as seen in Figure 4-24:

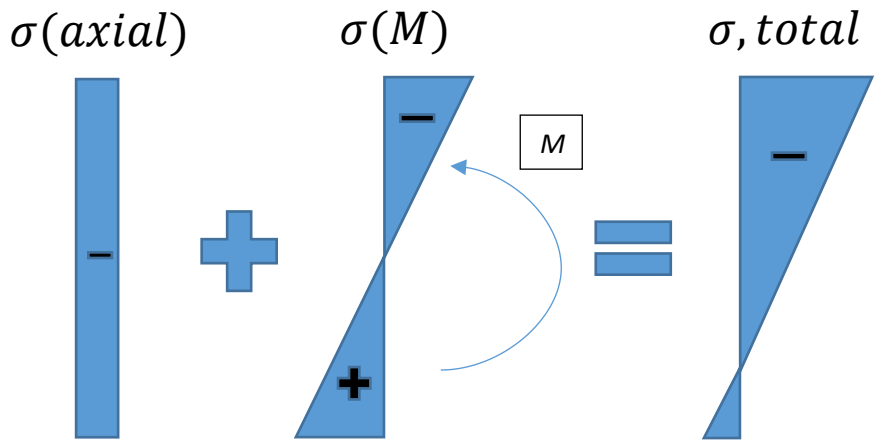

Figure 4-24: Example stress distribution following axial stress + stress due to bending moment

This stress distribution is converted to a strain distribution by dividing by the E-modulus. Since the position of the FBG in the girder is known, and the strain in any point of the section can be calculated following aforementioned methods, the data obtained by the FBGs combined with the load over time data can now be compared with the expected strain.

As visible in Figure 4-25, the FBG measurements at some point, start diverging from the linear model. This is as expected, since the first minor crack in the girder was reported at 117 kN of force, and more cracks started appearing around 130 kN of force. The diverging FBG strains are attributed to the cracking of the girder under the load. As the concrete cracks, the strain measured by the FBGs also increases. Cracked concrete cannot transfer tensile stresses, thus increasing the stress in the rest of the section. These increases stresses in turn lead to increased strains in the section and in the measurements. The separation points of the plots is around 150 kN, where the effect of cracks is noticeable in the results, indicating that the FBG sensors are capable of detecting occurring cracks. This is a higher load than the aforementioned 117 kN and 130 kN where cracks started to appear in the bottom of the girder. This can be attributed to the location of the FBGs, 100 mm from the bottom of the beam, where cracks have not yet propagated to. A nonlinear model is needed to estimate and calculate the increases in strain in the section, as the force further increases.

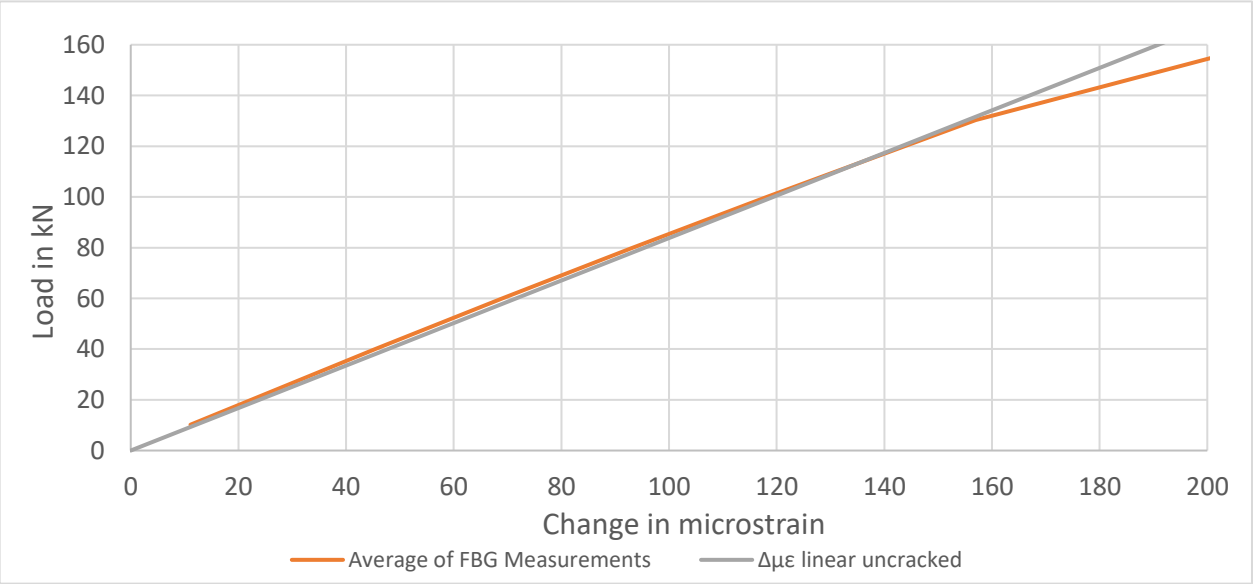

Figure 4-25: Comparison of FBG measurements vs theoretical linear model regarding increase of strain due to applied load in four-point bending test, assumed E-modulus = 35 GPa

4.3.6 Nonlinear calculations on cracked section

The analysis has been performed according to the approach as outlined in a paper by Robert F. Mast (Mast, 1998). The approach is simplified and shown below:
Step 1: Forces and moments in the section are known. The prestressing force and the external moments in this case. The external moment is comprised of the moment due to the force from the jacks, and the moment due to the effect of the own weight

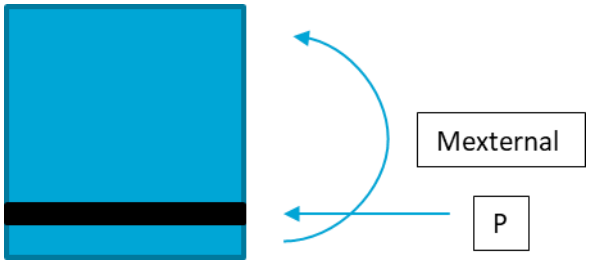

Figure 4-26: Forces and moments working on a section, steel prestressing strands are shown in black (side view)

Step 2: The height of the cracked section, and thus, the location of the neutral axis is unknown. The neutral axis location is guessed:

Figure 4-27: Cross section with the guessed location of the neutral axis: distance C. Prestressing strands are not shown for simplicity, for strand locations, see Figure 3-6

Step 3: For this assumed neutral axis position, all concrete below the neutral axis is assumed as cracked, and can therefore not transfer any stresses. The area of the prestressing strands in transformed to equivalent area of concrete using the ratio n of E-moduli to multiply the area of the steel by:

$$n = Esteel/Econcrete \quad (39)$$

Step 4: The new centre of gravity (c.o.g.) is calculated, following the removal of all concrete in the cross section below the neutral axis, and the transformation of the steel into equivalent area of concrete.

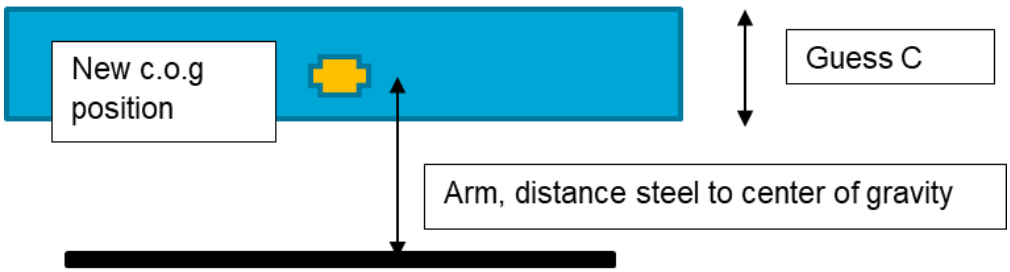

Figure 4-28: Cross section after concrete in tension is removed, and steel section area is transformed to equivalent area of concrete

Step 5: This new cross section creates a new stress distribution. The second moment of area of the new section is calculated, as well as the new stress distribution. The location where the prestressing force is applied in Figure 4-26 is relocated to the centre of gravity, this adds a moment which is added with the external moment in Figure 4-26. The total moment active is now the internal moment.

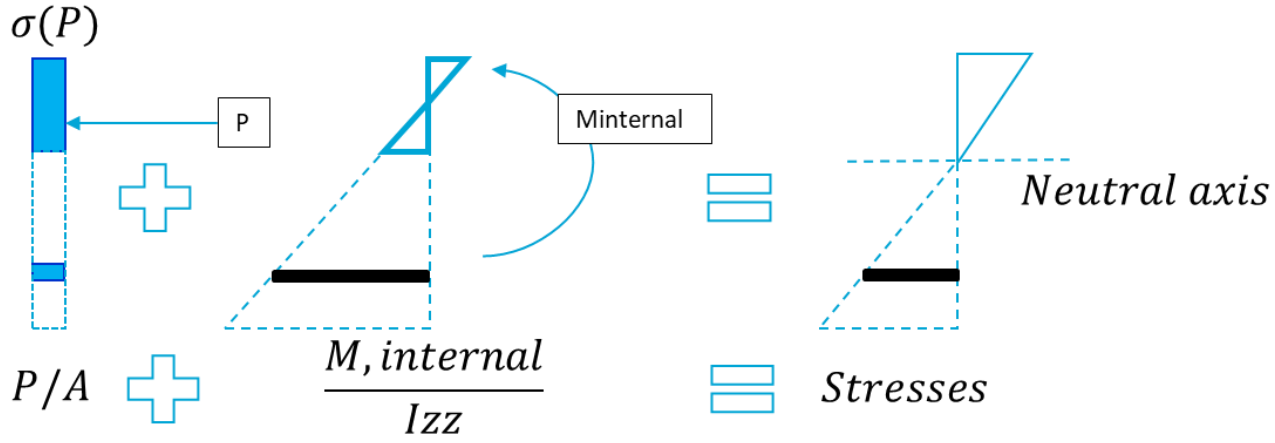

Figure 4-29: New stress distribution of the section, following addition of stress caused by axial stress, and stress by internal moment

Step 6: After the new stress distribution is calculated, a neutral axis can be located in the distribution. This is simply the spot where there is 0 stress. This location is compared to the initial guess for the location of the neutral axis in step 2. Naturally, the first guess is most likely to be wrong, and the calculation has to be performed again, using a different guess for the neutral axis location. This reiteration has to be performed constantly, until the result of the neutral axis calculation is equal to the guess. This is a converging iterative process.

When the neutral axis guess complies with the result, the stress at 100 mm from the bottom of the girder is taken, which is the same height as the location of the FBG-embedded rebar. The assumption is that this rebar measures the strain in the concrete, due to the rebar being bonded to the concrete around it. The stress is divided by the E-modulus of the concrete (35 GPa) to obtain the strain at FBG height. This method has been modelled in an Excel file and applied on the girder cross section following several values of the piston force in the flexural test until the maximum of 390 kN of single piston load. The result of this is visible in the figure below:

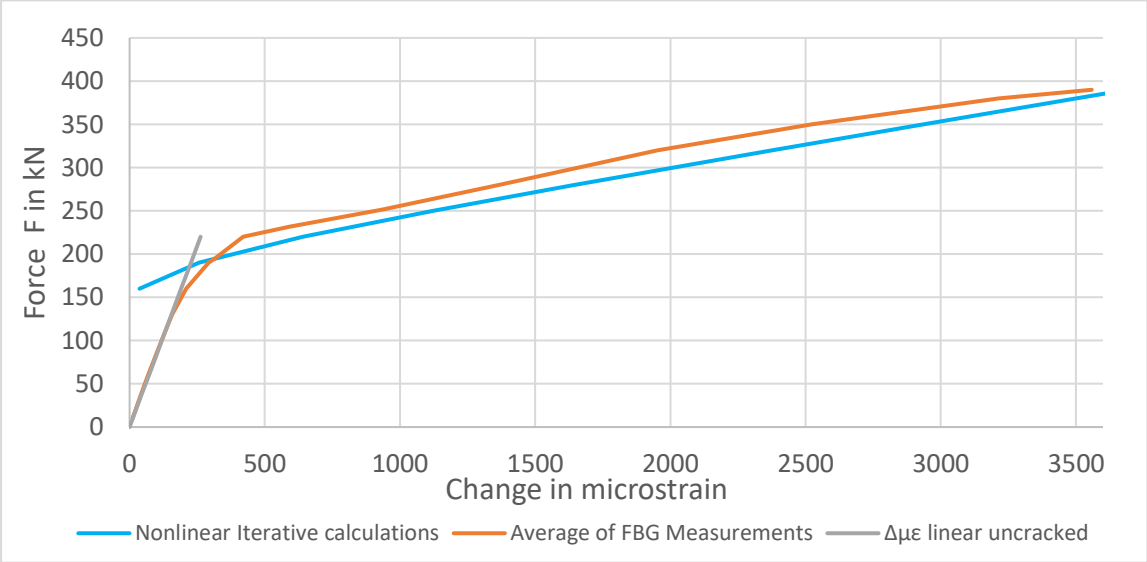

Figure 4-30: Nonlinear cracked cross section calculations for strain at FBG level versus FBG measurements assuming an E-modulus of 35 GPa for the concrete. Included is the linear calculation as also seen in Figure 4-25

Notable things about the results of this analysis is that it seems to replicate the expected strains versus the measured strains well, although the calculated strains are higher than the measured strains for the same force, until the maximum force of 380 kN is reached. Another observation is the gap seen between 150 and 200 kN. This is the zone where cracks start to develop and propagate in the girder. Both the linear model and the nonlinear model have inaccuracies in this cracking stage. The inaccuracy of the nonlinear model in this cracking stage can be attributed to the assumption that all concrete below the neutral axis cannot contribute to the distribution of stress. In real-life, however, this is not the case, as concrete can transfer tensile stresses, although limited, until the tensile cracking point is reached.

During the flexural test, a setup was also present to apply DIC (Digital Image Correlation) to detect cracking at the surface of the girder. However, as the FBG sensors were located in the core of the girder, DIC results could not be used to reference with FBG measurements to estimate the location of cracks. This is because the propagation of cracks from the surface to the location of the FBGs cannot assumed to be a straight line, resulting in uncertainties.

4.4 Shear test

4.4.1 General

The shear test is performed on specimen 4 at 60 days after casting of the prestressed girder. The load setup can be seen in Figure 3-26. Like the flexural test, this test has 3 phases of loading, loads are written in load per jack, as there were 2 jacks. The first phase sees loading until 10 kN and back to 0, this for the setup verification and eventual adjustments, FBGs are not actively measuring for this phase. Phase 2 sees the load increase from 0 to 160 kN of force, using 10 kN/minute force control. Pauses were scheduled in at 10, 40, 70, 100 and 130 kN for various measurements, before unloading back to 10 kN. Phase 3 loads the girder up to 160 kN, before loading to 300 kN with stops at 200 and 250 kN for measurements. After a lengthy break with the load at 300 kN, phase 4 loads the girder until failure, using displacement control at 0.5 mm/minute, before swapping to 1 mm/minute until failure.

For phase 2, it was chosen to once again, only let the interrogator collect data during loading and unloading of the girder. Pauses in loading during testing were made to allow measurements of different instruments to occur. The pauses in loading are clearly visible in the graphs, as pausing the applied load for extended amounts of time can result in creep effects occurring. There are no other notable observations made during phase 2 as seen in Figure 4-31. The sensors are clearly showing linear behaviour, sensors closer to the support experience less bending moments, and thus, show less strain due to the applied force. As FBG 4 and 5 are underneath the spreader beam, these FBGs experience near equal bending moments, resulting in strain measurements close to each other.

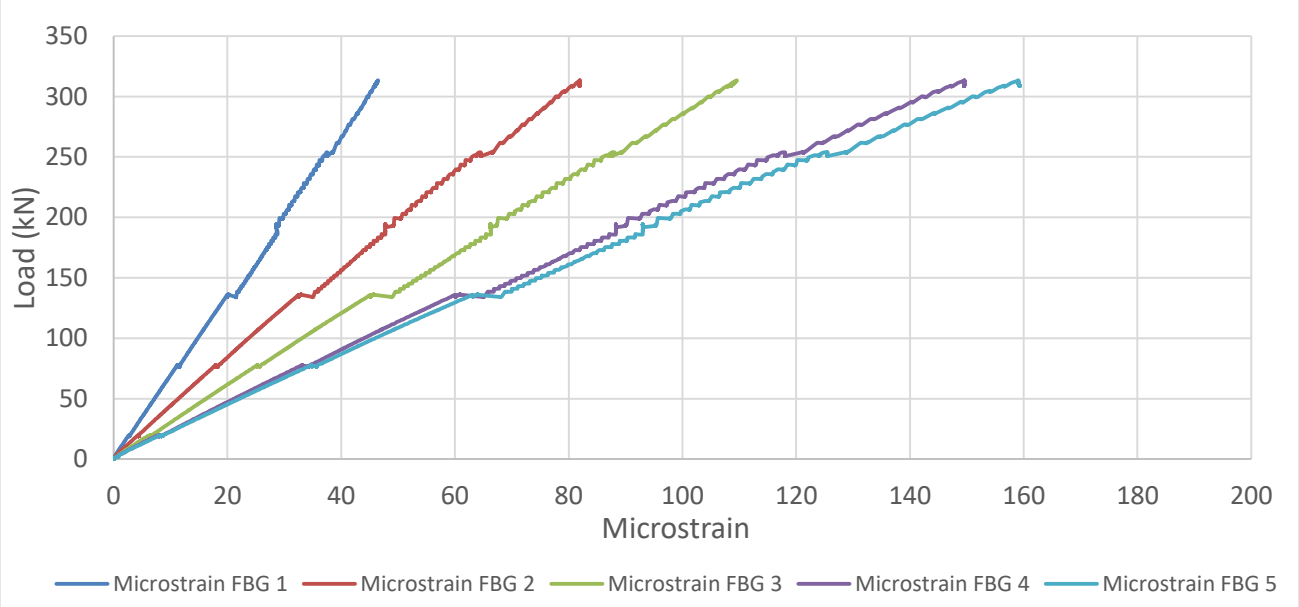

Figure 4-31: Shear test phase 2 FBG strain increase vs load increase

Phase 3 sees continuous FBG measurements made, with a small pause at around 300 kN of force to change the windows, to allow for enough room for a large change in the reflected wavelength curve. Notable in phase 3 is the nonlinear behaviour of the measured strains at 400 kN and above, starting from the lower numbered FBGs: 1, 2, and 3, which are located closer to the edge. Between phase 3 and 4, at 600 kN of total load, the windows are changed again in the interrogator software to prepare for phase 4, where the girder is loaded until failure.

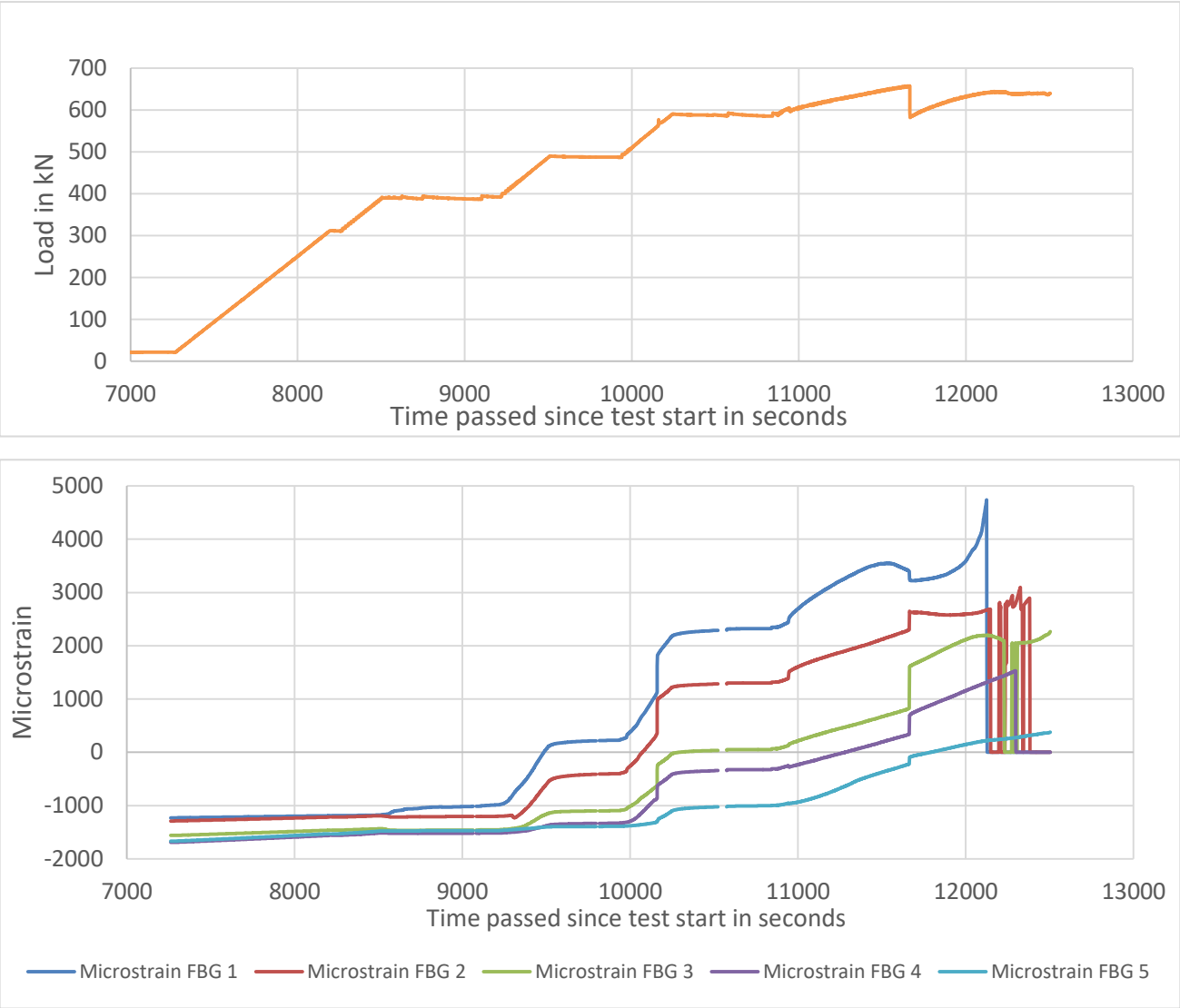

Figure 4-32: Shear test phases 3&4 graphs. Top: Load vs. time graph.

Bottom: Long 2 raw FBG data over time

Also notable is the rapid change of strain in multiple sensors, occurring at 563 kN. This is most likely due to the occurrence of tendon slip, as sounds were also observed during this loading period that can be linked to this. In phase 4, another two jumps in measured strains occur, at 605 kN and at 658 kN. The latter occurs as the same time as a rapid decrease in load. Near the end of the measurements, the strains measured in FBGs 1, 2, 3 and 4 can be seen moving erratically. This could have several reasons, including: exceeding the strain range of the FBGs, failure of the epoxy that binds the FBG to the steel rebar strain. The failure of the girder is attributed to a mixed mode failure: A shear failure, and a failure due to debonding of the topping with the precast girder and tendon slip.

4.4.2 Tendon slip

The FBG measurements show three possible points in the test where tendon slip could have occurred: at 563 kN, 605 kN, and 658 kN. The mechanism behind this will be shortly explained, with the possible benefit the FBG measurements bring. The occurrences of the tendon slip events can be linked to the anchorage of tendons for the ultimate limit state. Chapter 8.10.2.3 of EC2 has been

applied for this analysis. The concrete tensile stress exceeds the tensile strength in these moments during the shear test, as there were already multiple cracks present at 400 kN of total force.

The tendon force is now calculated, including the effect of shear according to Eurocode 2 Chapter 6.2.3 (7). This is the additional tensile force in the longitudinal reinforcement, including the prestressing strands, due to shear forces:

$$\Delta F_{td} = 0.5\, V_{Ed}(\cot\theta - \cot\alpha) \qquad (40)$$

With: V_{Ed} = Shear force

θ = Angle between the concrete compression strut and the beam axis perpendicular to the shear force

α = Angle between the shear reinforcement and the beam axis perpendicular to the shear force

An assumption has to be made for the angle of the concrete compression strut in a strut and tie model of the composite girder in the test setup. The distance between the top end of the shear reinforcement in the topping (66 mm from the top) and the centre of the prestressing strands in the precast girder will be used as the total height of the simple strut and tie model. With the total height of the composite girder at 420 mm, the height of the strut and tie model is ±288 mm, which is a rough assumption as to how the model works in the actual girder. The distance from the centre of the applied force to the close support is 1200 mm. But in a strut and tie model, the angle between the compressive strut and the horizontal axis can only deviate between a certain range, as recommended by formula 6.7N in EC2. The strut can therefore not span the entire diagonal between the support and the location of the force. The strut and tie model can be divided into 2, or 3 parts, shown in the figure below, with compressive struts in blue, and tensile ties in red, both of these angles of θ satisfy the range specified in formula 6.7N of EC2.

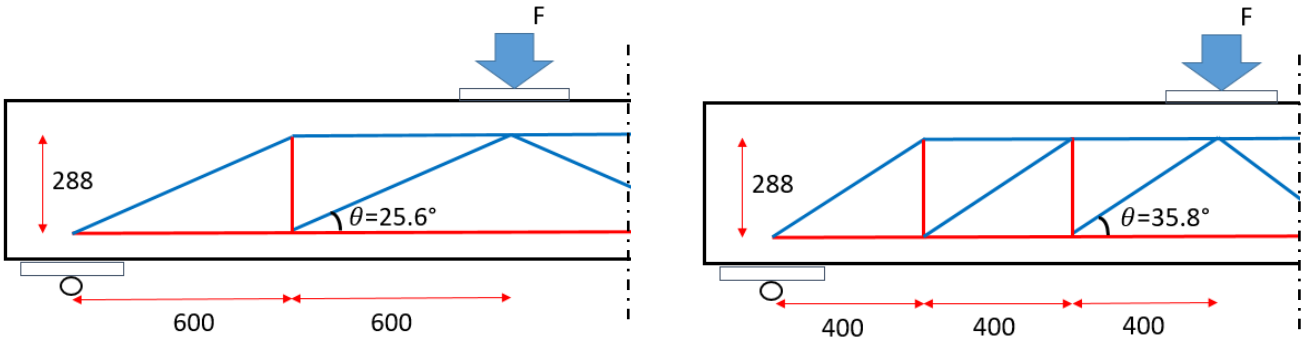

Figure 4-33: Strut and tie models of the shear test beam. Left: case 1: 600

The angle α in this girder is 90 degrees, because the transverse reinforcement is perpendicular to the beam axis. Since the cotangent of 90 degrees does not exist, a value very close to 90 can be taken, resulting in $\cot\alpha = 0$. The shear force in the short end of the beam is equal to 5.8 divided by 7, times the force, because of the location of the external force relative to the supports. The first of the possible tendon slip moment is selected: 563 kN of force, giving a shear force V_{Ed} of 466.5 kN.

Putting the values into equation 40 gives an additional tensile force ΔF_{td} of 487 kN for case 1, and 323 kN for case 2. This has to be added to the tendon force in the cracked section. The location under the load will be used for this analysis. The nonlinear model used in Chapter 4.3.6 will be used again, to approximate the stress in the tendons.

Using equation 27, the moment due to own weight is determined to be 12.5 kNm. This is inserted in the model, including an external moment of 1.2 meter × 563 kN × (5.8/7), keeping all other parameters the same, as the girder is mostly the same as the girder tested in bending. This results in the location of the neutral axis at 156.2 mm from the top of the girder, and a total tensile force in the steel of 1898 kN. Giving a total steel force in case 1 of: 2384 kN, and in case 2: 2220 kN.

Adding this tensile force to the force due to shear, and dividing by the tendon area of 1600 mm^2 gives a total tensile stress σ_{pd} in the tendons for case 1: 1490 N/mm^2, case 2: 1388 N/mm^2. These tensile stresses are compared to the anchorage capacity, as there needs to be sufficient capacity to deal with these stresses, or premature failure occurs. The bond strength for anchorage in the ultimate limit state is given in formula 8.20 in EC2:

$$f_{bpd} = \eta_{p2}\,\eta_1\,f_{ctd} \qquad (41)$$

With: η_{p2} = 1.2 for 7-wire strands
η_1 = 1.0 for good bond conditions, or 0.7 otherwise, 1.0 is assumed
f_{ctd} = design tensile strength of the concrete, determined at 1.27 N/mm^2

Note how the formula does not take into account the amount of time passed since the concrete reached the rated strength. In practice, concrete continues to gain strength beyond 28 days after casting. This design tensile strength is also an assumption, and may not be correct for this concrete type. This results in f_{bpd} = 1.524 N/mm^2
The total anchorage length for anchoring a tendon with stress σ_{pd} is given by EC2 formula 8.21:

$$l_{bpd} = l_{pt2} + \alpha_2\phi(\sigma_{pd} - \sigma_{pm\infty})/f_{bpd} \qquad (42)$$

With: l_{pt2} = upper design value of transmission length = 1.2×763 = 916 mm (EC2 8.18)
α_2 = 0.19 for 7-wire strands
$\sigma_{pm\infty}$ = prestress after all losses: 1647 kN divided by the steel area (Chapter 4.3), not quite infinite, but applicable because this is the approximation of the prestressing force left at time of testing.

This results in a total anchorage length for case 1 of 1490 mm, and case 2: 1363 mm. The edge of the girder extends slightly beyond the support, by roughly 170-175 mm. The distance between the edge of the girder and the point of loading is ±1375 mm, and is barely enough to anchor the additional tendon stress due to flexural cracking in case 2, but not enough for case 1. This analysis is built on previous and new assumptions and is not expected to be accurate, ordinary reinforcement in the precast girder (longitudinal), 4 Ø10 has been ignored in this calculation due to complexity, and the upper design value of transmission length is most likely undervalued due to lack of measurements, on top of the existence of several flexural-shear cracks during testing.

However, this gives an insight into the mechanics that could be behind the tendon slip events: the extra stress in the tendons due to flexural cracking needs to be anchored in concrete by usage of a flexural bond length, consisting of the difference between the maximal tendon stress σ_{pd}, and the remaining prestressing stress. The total anchorage length consists of the sum of this flexural bond length and the transmission length. If there is not enough concrete to transfer these forces from the tendons: the transmission length and the flexural bond length overlap, this results in the tendon stresses not being able to be transferred, resulting in earlier failures. (Geßner, 2017)

4.5 Mock-deck tests

4.5.1 First test, general

The first test performed on the mock-deck since the cyclic loading test has been concluded is a static load test located in the middle of the slab (flexural critical position). This has been performed 49 days after casting of the topping. The load protocol is as follows, using a force control of 10 kN per minute: The first phase sees loading until a total load of 20 kN, and unloading for the initial checks. There are no FBG measurements during this. The load is then increased from 20 kN to the observed cracking load, in this case it was 460 kN, with stops at 40 kN, 160 kN, 200 kN, 280 kN and 400 kN to allow for several other measurement setups to gather data. During these breaks, the measurements of the FBGs have been halted as well. The second phase sees unloading from 460 kN back to 20 kN without stops. Phase 3 sees reloading until 460 kN without stops, and then loading until 1000 kN under displacement control (0.5 min/mm), with stops at 460 kN, 640 kN, 800 kN and 960 kN. The load vs time graphs can be seen in the figure below, featuring the synchronised FBG measurements of the Short 1 rebar, which is located in the middle girder of the mock-deck.

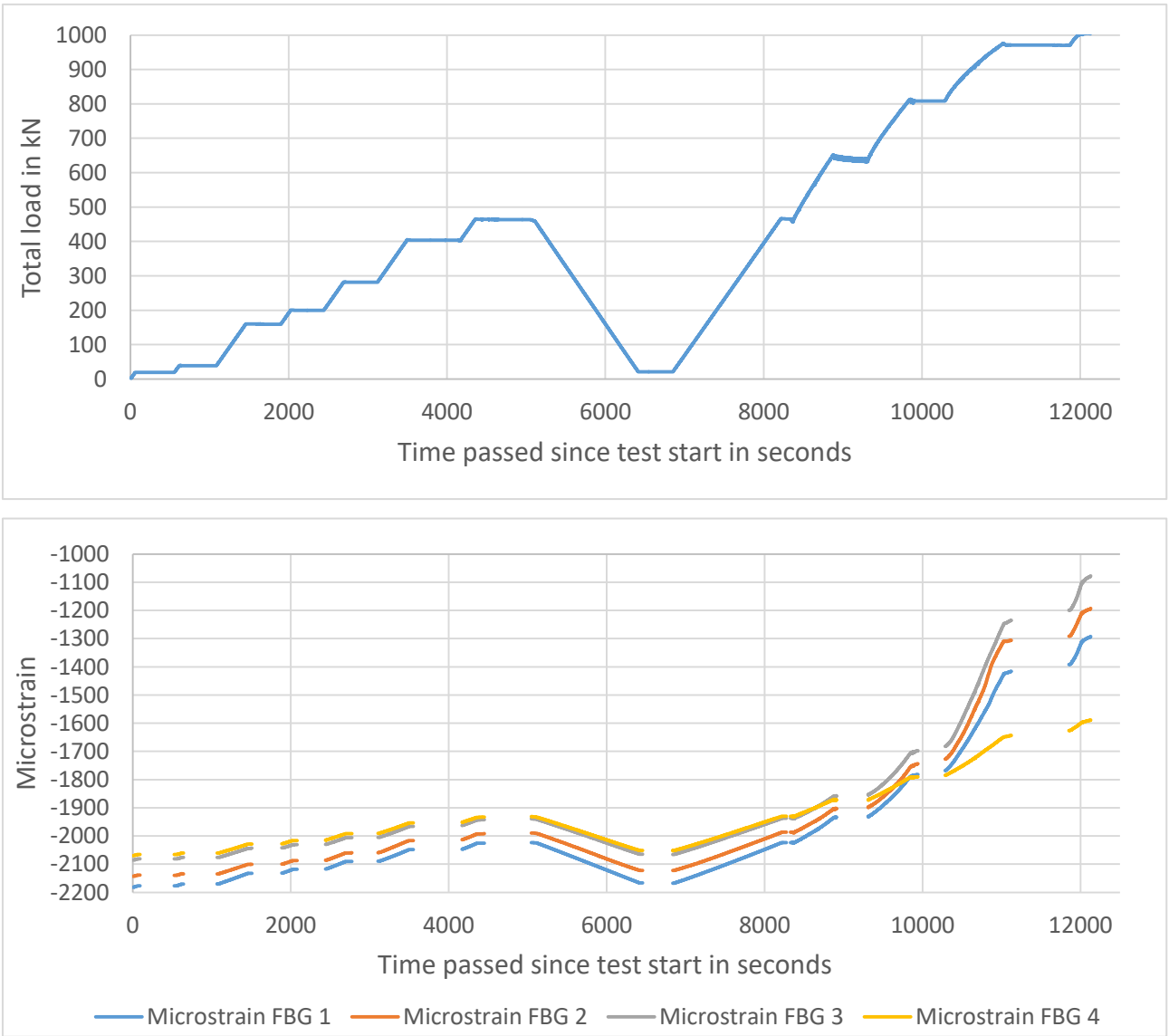

Figure 4-34: Mock-deck flexural test graphs. Top: Load vs. Time graph. Bottom: Short 1 FBG data

Notable is the large break in measurements at 960 kN. Holding the load for a long time at such a high load will incur creep effects, these are visible in the graph by the jumps of roughly 35 microstrain in FBG 3, for example, at the end of the test. As the different sensors have different starting points of measuring, the data is zeroed at the beginning of phase 3: 20 kN of load. This done to compare the measurements of the FBGs in an easier way. This graph can be seen in the figure below:

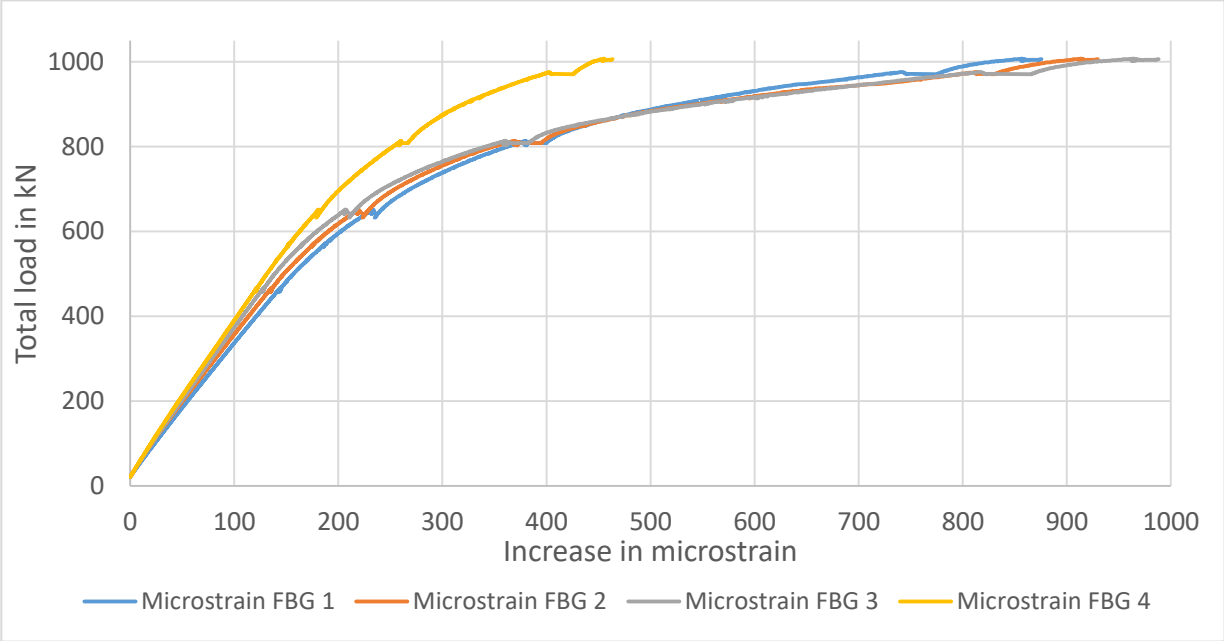

Figure 4-35: Increase in measured strain in phase 3 of the slab flexural test, FBG data zeroed at 20 kN of load

4.5.1.1 Linear beam model

To start off, a linear beam model is applied to obtain an expected change in strain for the change in load and compared to the linear phase of testing, as seen in Figure 4-36. The same process has been used as in Chapter 3.3.5, with a change in cross sectional properties and load position. Several simplifications are made: The point load is simulated in the model as a line load across the entire width, similar to the flexural load test performed on specimens 3 and 4. Also, the E-modulus is assumed to be a consistent 35000 MPa for the entire cross section.

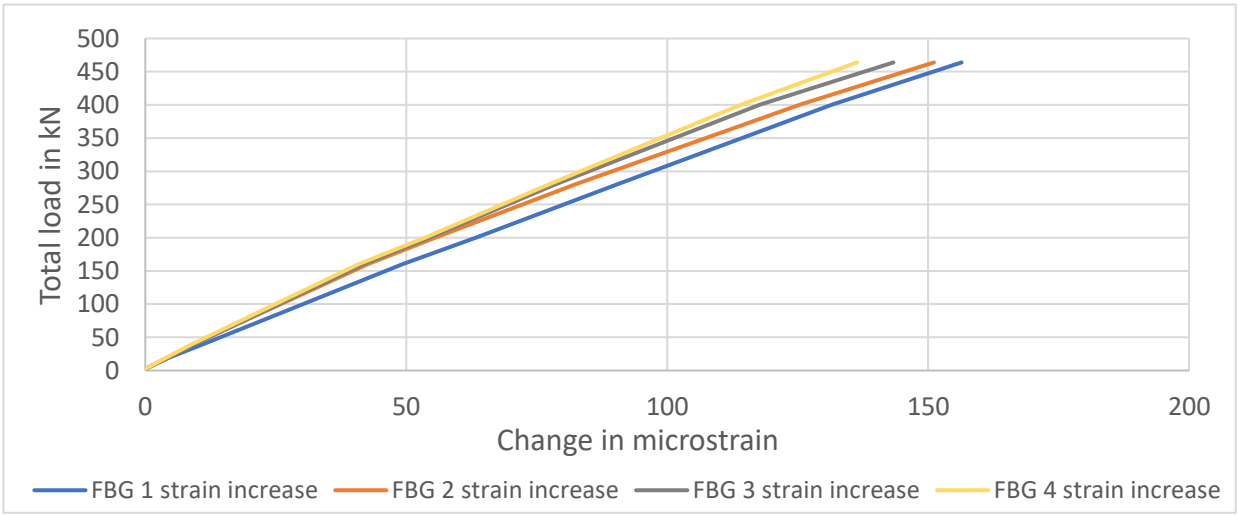

Figure 4-36: Change in microstrain vs load during phase 1 of flexural slab testing

In actuality, this is most likely lower, as the outer edges of the topping have been exposed to drying conditions since testing.

The original AutoCAD model has been obtained, and a cross section of the mock-deck in the middle of the span is used to approximate the cross section properties of the mock-deck: A total area of approximately 1.32×10^6 mm^2, and a second moment of area of $\pm19.1\times10^9$ mm^4. Its centre of gravity lies at 212 mm from the bottom of the slab, meaning the FBG ''fiber'' is positioned at 112 mm from the centre of gravity. Using these properties and the linear relation of stress, strain and E-modulus, the expected strain using the beam model following the load is plotted in the same plot as Figure 4-36:

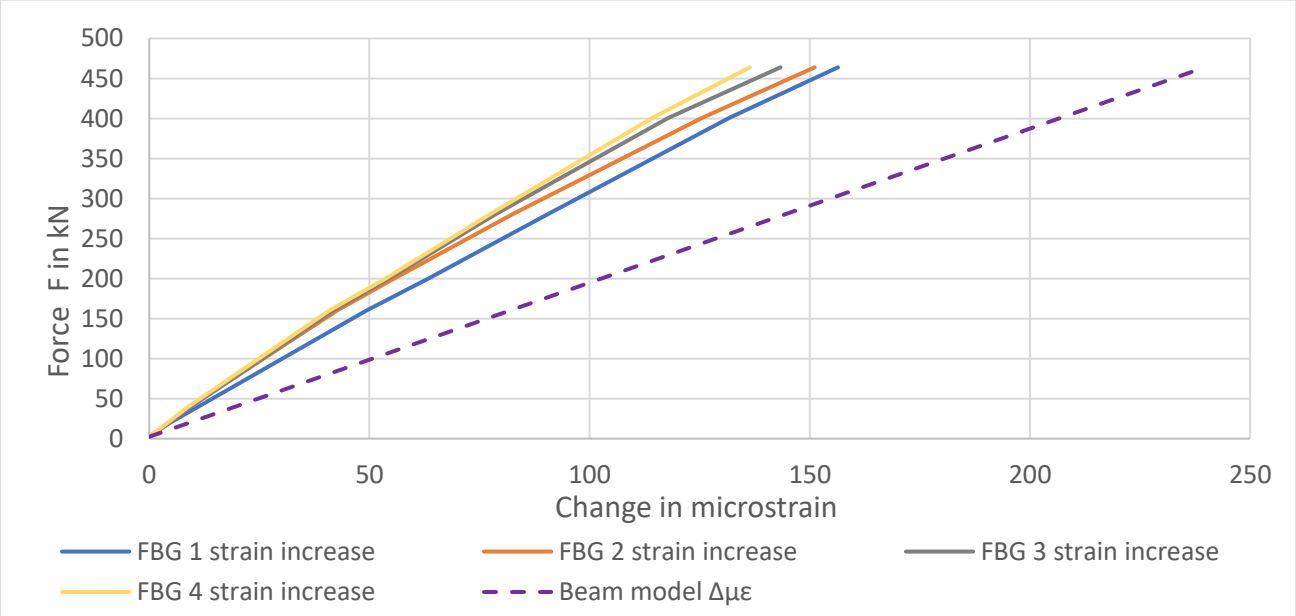

Figure 4-37: FBG measured increases in strains due to piston force, strain increase at FBG fiber using beam model

As visible in Figure 4-37, the beam model overestimates the change in strain at the FBG fiber, compared to the FBG measured strains. This is not as expected, since this beam model simplifies the point load to a load that is spread across the entire width of the beam. In reality, the middle girder should take a larger percentage of the load, compared to the girders at the side of the slab. The beam model overestimates the strain by ±60%. Another model to predict the behaviour of the slab has been used in the next chapter.

4.5.1.2 Model following Guyon-Massonnet method

This method follows from analyses on orthotropic slab behaviour by Guyon in 1946, and extended by Massonnet in 1950. Orthotropic behaviour of the slab is described by this method using the slab geometry, material stiffness, flexural rigidity and torsional rigidity. Following this, concentrated loads can be distributed over an effective width. In this use case, the concentrated load is distributed over the width of the mock-deck. Following this, the expected strain change at FBG height is calculated and compared to FBG measurements during the linear uncracked phase of loading, using the contribution of the distributed concentrated load for the middle girder.

For this, the principal lateral distribution coefficients K have to be determined for different locations across the width of the beam. This is done by using graphs that give values for K at specific positions, following a value for lateral distribution α, which physically represents the torsional stiffness relative to the flexural stiffness in the slab. For isotropic plates or slab bridges, this value is

1. This can be applied to this slab due to its close resemblance. Another value needed is θ_2 determined from this formula:

$$\theta_2 = \frac{b}{l} \sqrt[4]{\frac{\rho_x}{\rho_y}} \quad (43)$$

With: b = half of the slab width = 1590 mm
l = span = 7 m
ρ_x = average bending stiffness per unit width around local x-axis
ρ_y = average bending stiffness per unit width around local y-axis

$$\rho_x = \frac{EI_x}{b1} \quad (44)$$

$$\rho_y = \frac{EI_y}{a1} \quad (45)$$

With: $b1$ = width of the middle singular girder = 990 mm
$a1$ = span = 7 m
I_x = Second moment of area around local x-axis = 19.1×10^9 mm^4
I_y = Second moment of area around local y-axis, middle girder: $I_y = \frac{1}{12}bh^3$
$I_y = \frac{1}{12}bh^3 = \frac{1}{12} \times 7000 \times 420^3 = 4.322\times10^{10}$ mm^4
E = elastic modulus, assumed at 35000 MPa for the entire section to reduce complexity

This results in ρ_x = 6.965×10^{11} Nmm^2/mm, ρ_y= 2.161×10^{11} Nmm^2/mm, and θ_2= 0.305.

Using this and the graphs from the method, the following values for K are obtained at values for b, which stands for half the width of a slab at 1590 mm, seen in Table 9, where the values can be seen in respective to the location in the girder, using a local horizontal coordinate system with the origin coinciding with the middle of the width of the slab (x = 0). This is all assuming a concentrated load applied in the middle.

Table 9: Values for principal lateral distribution coefficient K, across the entire width of the mock-deck

x	-b	0.75b	0.5b	-0.31b	-0.25b	0	0.25b	0.31b	0.5b	0.75b	b
K	0.85	0.95	0.98	1.036	1.05	1.12	1.05	1.036	0.98	0.95	0.85

This is also represented in graph form:

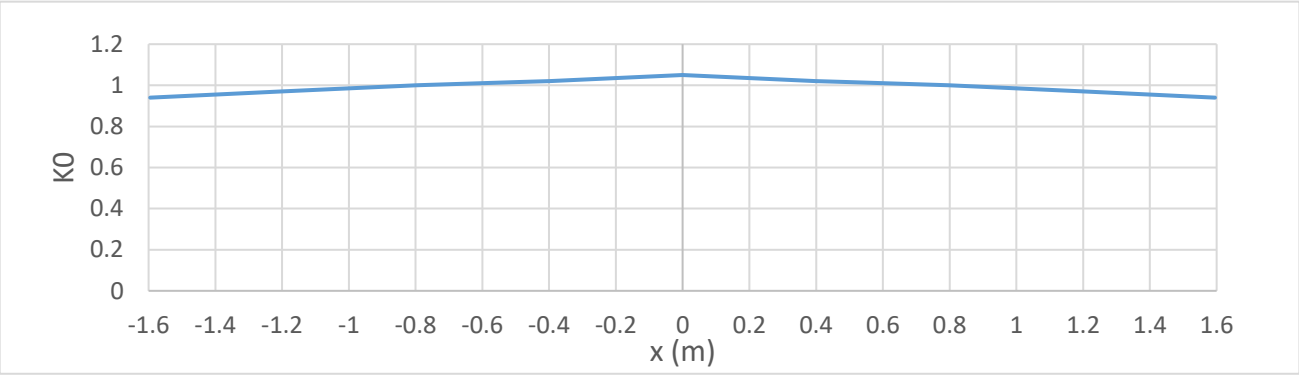

Figure 4-38: Values for lateral distributions coefficient K0 across the width of the mock-deck

The value for K is interpolated at x =0.31b, this is the edge of the middle precast girder. Following this, the integral under the plot for K is determined for the middle girder at -0.495 < x < 0.495 and the rest of the slab. The middle girder is found to take 32.14% of the distributed concentrated load, whereas the rest takes 67.86%. Now to calculate the expected strain change due to the concentrated load ΔF: The middle 990 mm girder + topping combo has a second moment of area of 6.1×10^9 mm^4 with a centre of gravity at 210 mm from the bottom. FBGs are positioned 110 mm below this centre of gravity. The formula used for strain change is as follows:

$$\Delta\epsilon = \frac{\Delta M \times z}{Izz}/E \qquad (46)$$

With $\Delta M = \Delta F \times (3500\ mm - 400\ mm)$, with the 400 mm accounted for because of the edge of the metal plate with a total length of 800 mm. The highest moment occurs below the metal plate. And z = 110 mm. Assuming a consistent 35000 MPa for the E-modulus.
The increase in microstrain, due to the increase in load is calculated for the G-M method, using:

$$\Delta\epsilon(G-M\ method) = \frac{\Delta F\ (kN) \times 1000 \times 3100 \times 32.14\% \times 110}{6.1\ \times 10^9}/35000$$

Using the values for concentrated load from the test, a strain diagram can be plotted in the same plot as Figure 4-37:

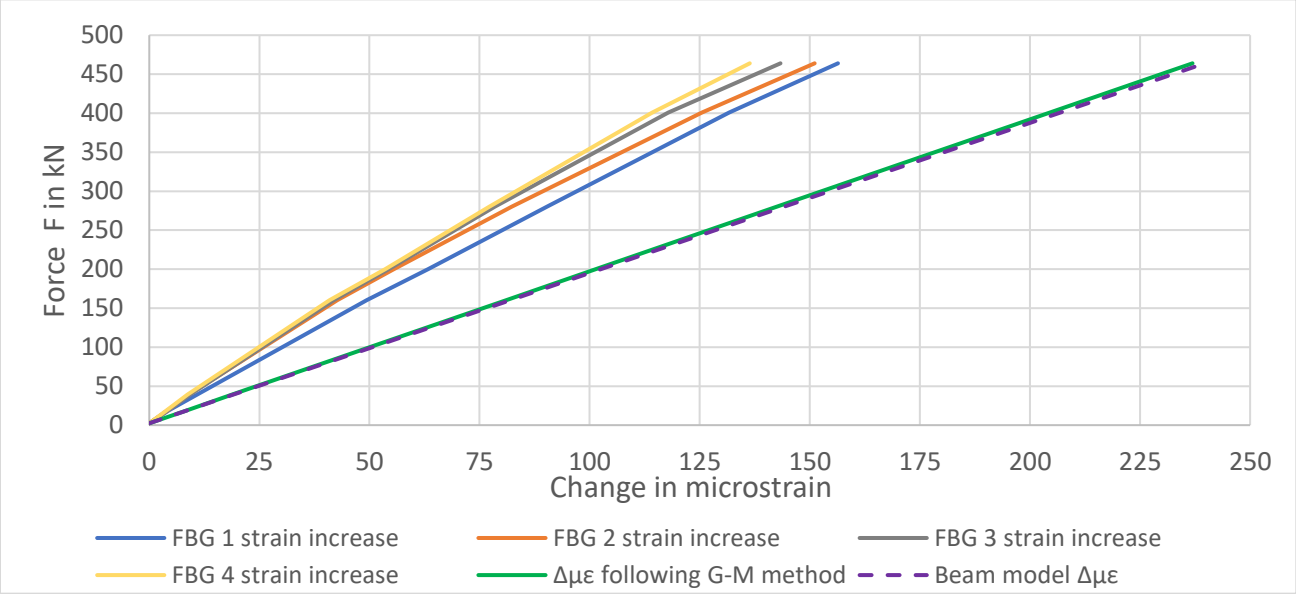

Figure 4-39: Measured strains in FBGs during phase 1 of slab test 1, with expected strains following a simple beam model, and a model following the Guyon-Massonnet method

The expected strain following the model using the Guyon-Massonnet method also overestimates the strain, which was expected. This can be explained by following: A high value of α, and low value of θ_2, the high transverse stiffness results in the distribution of the concentrated load in such a way that it produces a rather flat graph of the value for K across the width of the slab. For higher values of θ_2, the middle girder would take a larger portion of the load than it currently does. However, the middle girder receiving more load would only overestimate the strain even further. The model is very close to the strains following a beam model, and is slightly lower, this can be attributed to the slightly higher centre of gravity used in the beam model.

4.5.1.3 Additional comparisons and validations

For a comparison, the data collected by the LVDT strain gauges, located externally at the bottom of the slab near the load point, is plotted against expected strains occurring in the bottom fiber of the slab, using the beam model. The position of the two LVDTs located in the middle of the slab, 17F and 18F are visible in Figure 4-40, with the dotted rectangle representing the metal plate that distributes the piston loads. (Matthys, Proia, Sun, Ghorbani, & Krajnovic, 2022)

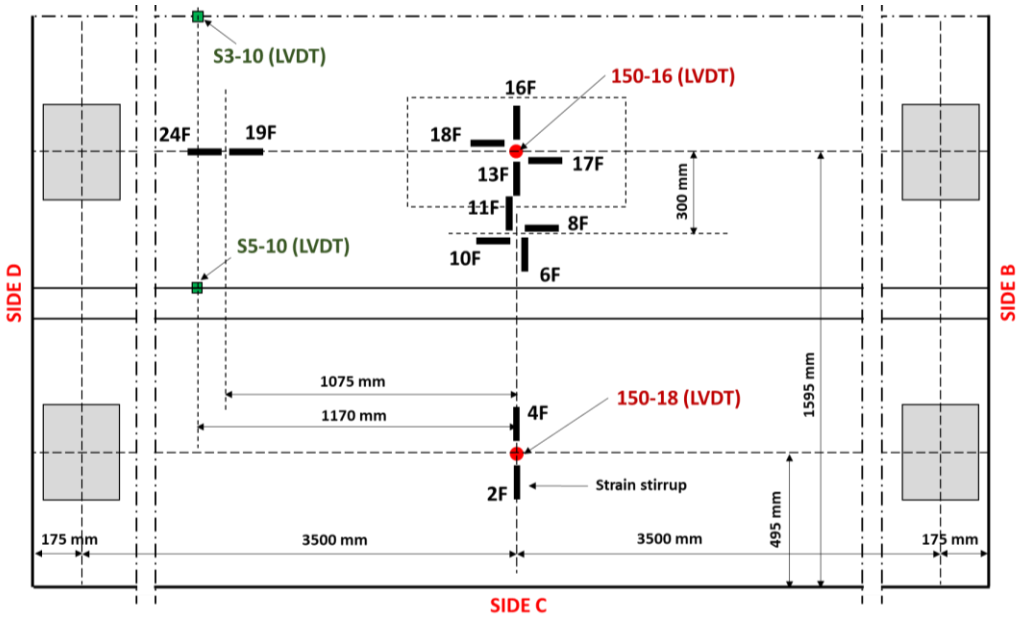

Figure 4-40: Location of LVDTs located at the bottom (soffit) of the mock-deck (Matthys, Proia, Sun, Ghorbani, & Krajnovic, 2022)

The strains at FBG level following calculations using the beam model are simply scaled to estimate the expected strains in the bottom fiber of the girder by dividing by the distance between FBG fiber and centre of gravity, and multiplying by 210 mm as seen in Figure 4-41. The strain measured by the LVDTs confirm the strains as measured by the FBGs, as the beam model overestimates the strain in the bottom fiber by ±64% at 464 kN, compared to the strains measured by LVDTs. This is similar to the gap between FBG measurements and the models used in Figure 4-39, validating the FBG sensors as internal strain sensors at ±100 mm from the bottom of the cross section.

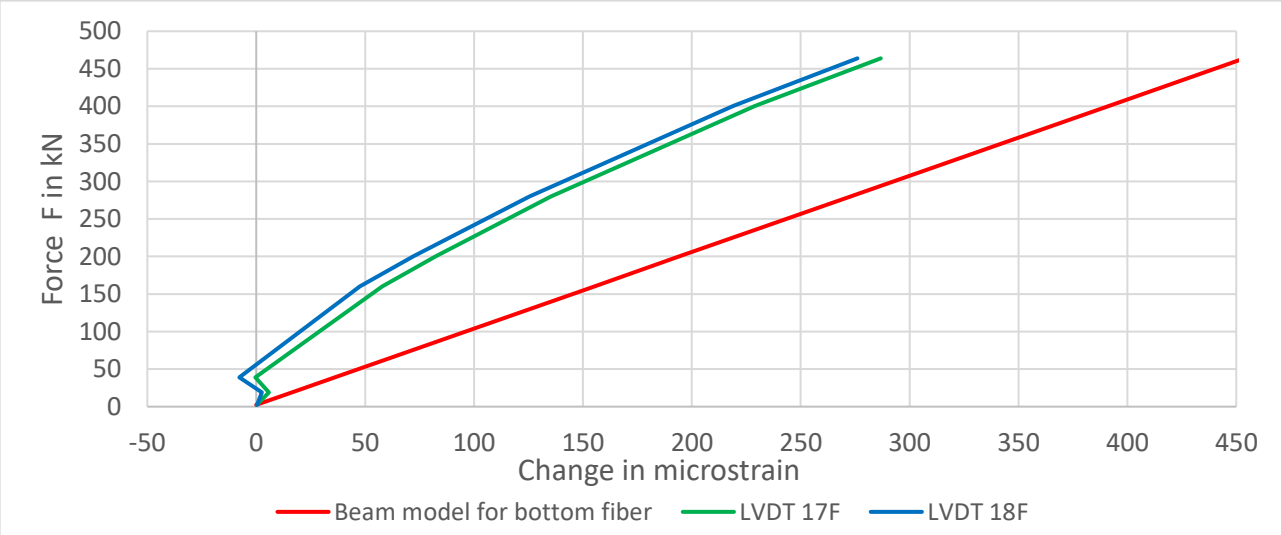

Figure 4-41: Strains as measured by LVDTs located underneath the loading point vs beam model for expected strains in bottom fiber

For an additional comparison, the deflection of the slab is compared with a value resulting from a beam model calculation. As seen in Figure 4-40, LVDT 150-16 is located at the load patch, this LVDT recorded a deflection of 6.490 mm at a load of 463.68 kN, which was still within the linear portion of the load test. Using a simply supported beam model as seen in the figure below, the deflection in the middle is as follows, simplifying the load patch to a point load F applied in the middle of the span:

$$w(midspan) = \frac{FL^3}{48EI} = \frac{463.68 \times 10^3 \times 7000^3}{48 \times 35000 \times 19.1 \times 10^9} = 4.95mm \quad (47)$$

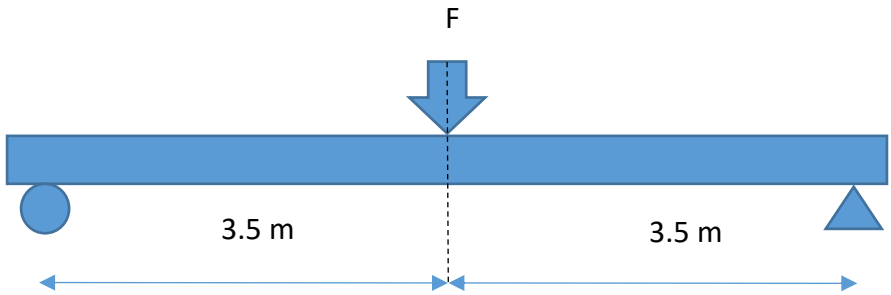

Figure 4-42: Schematic of the simply supported beam model.

The recorded deflection is ±31% higher than the deflection following the model. This is as expected, as the force applied on the real life slab is not spread across the width of the slab, unlike the model, resulting in a higher deflection. However, this is not in line with the comparisons of the FBG and LVDT measurements with strain estimations based on the beam model and the Guyon-Massonnet method. The FBG and LVDT measurements suggest a much stiffer response of the slab than the already conservative models predict, whereas the deflection appears to be higher than estimated with the simply supported beam model.

4.5.2 Second test

The second test performed on the mock-deck since the cyclic loading test has been concluded is a static load test located in the critical position for shear. This has been performed 58 days after casting of the topping. The load protocol is as follows, using a force control of 10 kN per minute: The first phase sees loading until a total load of 20 kN, and unloading for the initial checks. There are no FBG measurements during this. The load is then increased from 20 kN until 760 kN, with stops at 40 kN, 160 kN, 280 kN, 340 kN, 400 kN, 460 kN, 580 kN, 640 kN, and 700 kN to allow for several other measurement setups to gather data. Again, during these breaks, FBG measurements are not running. Phase 2 sees unloading from 760 kN to 20 kN without stops. Phase 3 reloads to 760 kN without stops. After this, there is further loading until 1000 kN using 0.5 min/mm displacement control, with stops at 800 kN, 880 kN and 990 kN. The load vs time graph and FBG measurements are shown in the figures below.

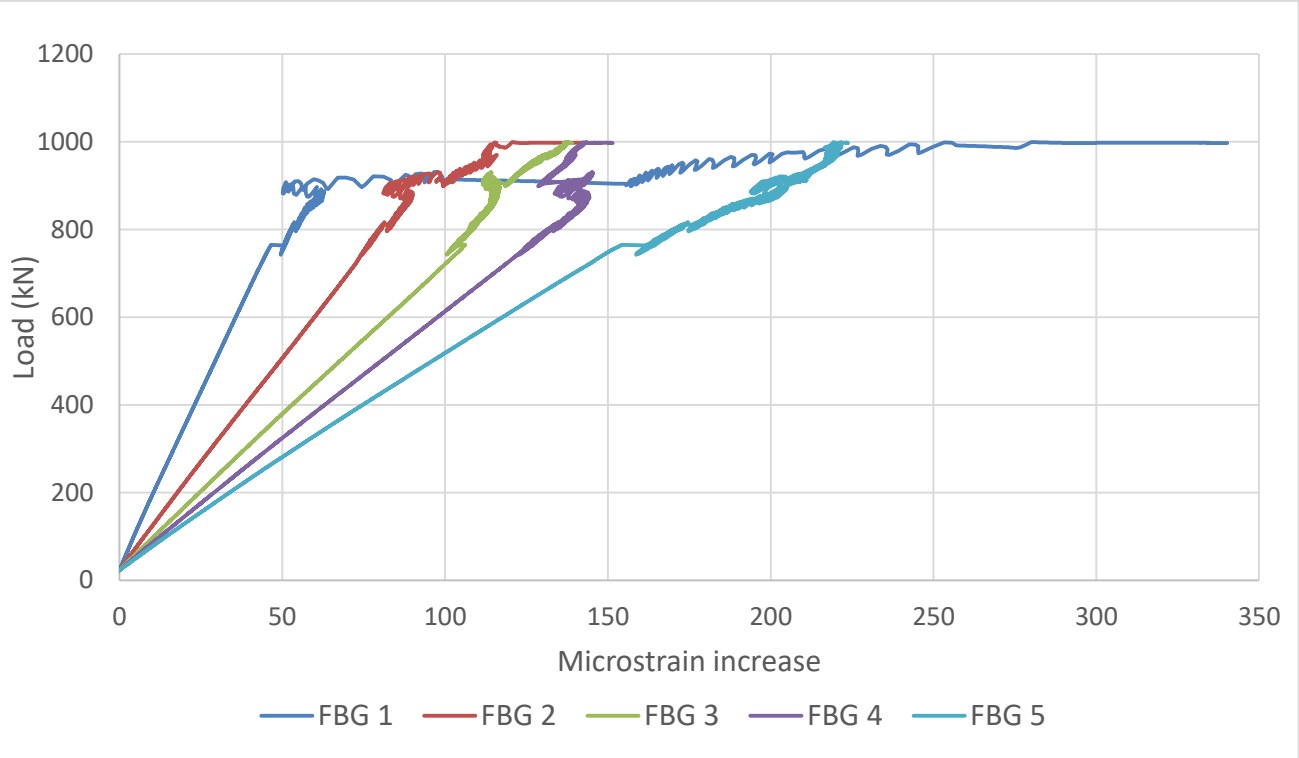

Figure 4-43: FBG measured strains during the second test performed on the mock-deck

As visible, measurements at a total force 760 kN and below appear to be linear, indicating no cracks affecting the FBGs. This changes at 800 kN and above, where FBG 1, positioned closest to the edge, experiences a larger strain change when compared to the other FBGs. The loading jacks, however, exhibited unstable loads above 800 kN. This can be seen using the FBG measurements between 800 and ±930 kN of loading. The original measurements are shown in Figure 4-43a, while Figure 4-43b sees the strains zeroed at 800 kN, and plotting the change in strain with the load data.

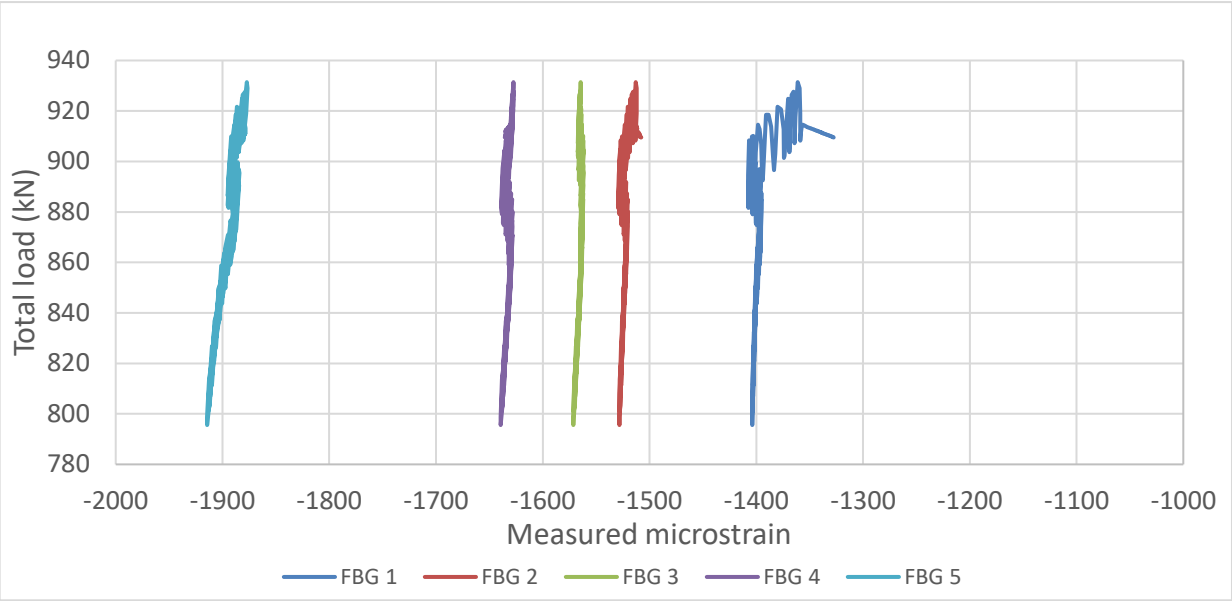

Figure 4-44a: Strains as measured by the FBGs during test 2 on the mock-deck, between 800 and 920 kN of total load

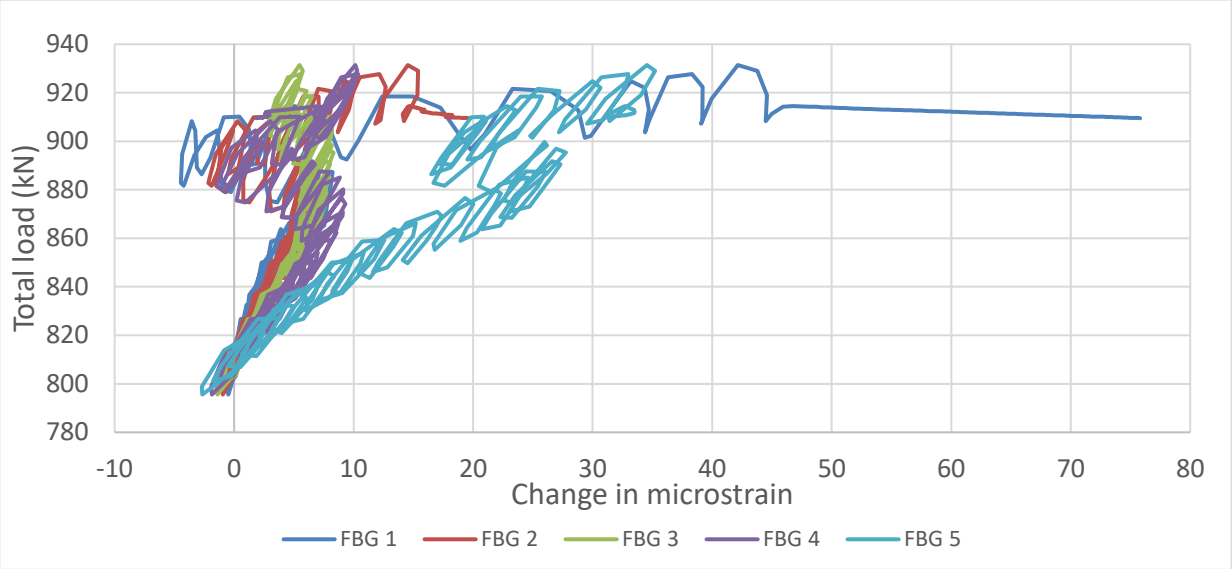

Figure 3-43b: Strain change as measured by the FBGs during test 2 on the mock-deck, between 800 and 920 kN of total load

The test is performed until the maximum total load of the pistons has been reached at 1000 kN. Once again, the strains are zeroed at the beginning of the measurement at ±904 kN, as visible in Figure 4-44b. This is done to indicate the relatively high strain changes seen in FBG 1, compared to the other strains. This nonlinear behaviour can be attributed to proximity of a nearby crack. The location of this FBG, at 46 cm from the edge also means the tendons are only able to deliver a fraction of the compressive stresses from prestressing to the concrete at this point, resulting in an earlier occurrence of tensile stresses and thus, earlier occurrence of cracks in this section of the slab.

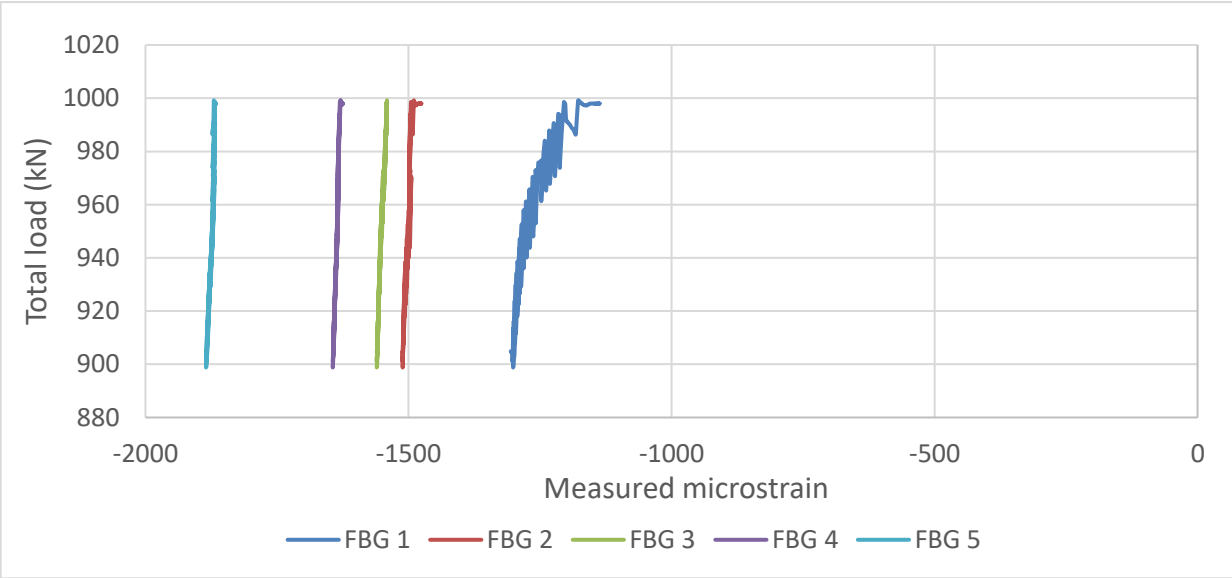

Figure 4-45a: Strains as measured by the FBGs during test 2 on the mock-deck, between 800 and 1000 kN of total load

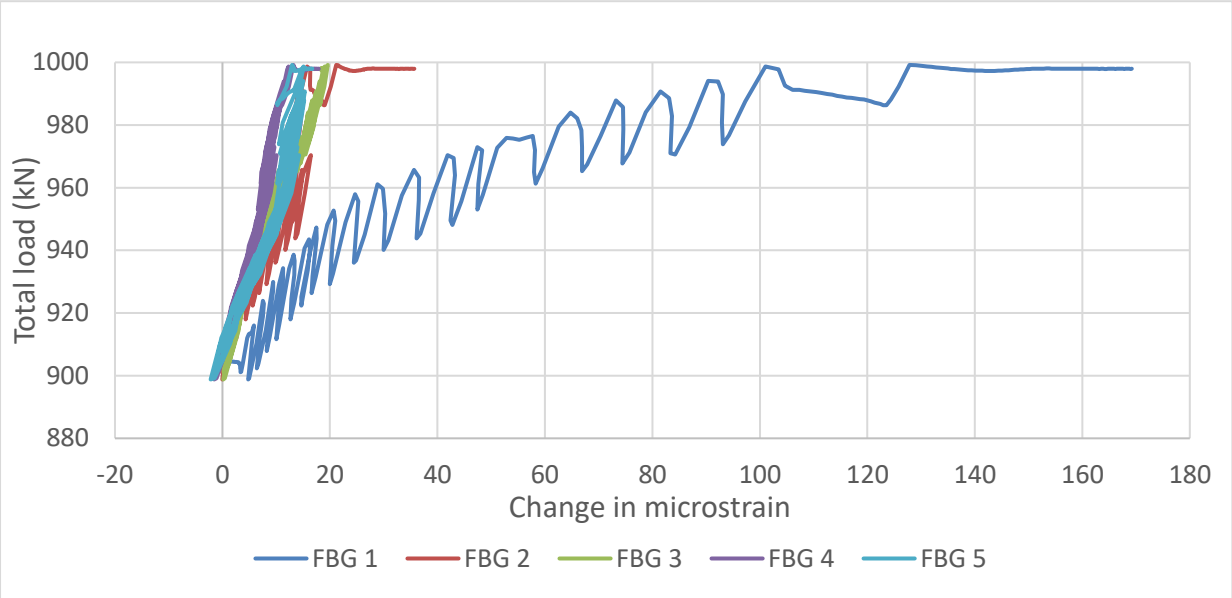

Figure 3-44b: Strain change as measured by the FBGs during test 2 on the mock-deck, between ±904 and 1000 kN of total load

5 Discussion, conclusion and recommendations

During this study, FBG fiber optic strain sensors that are embedded in a steel rebar are applied inside precast prestressed geopolymer concrete girders. Data is collected and evaluated to obtain more knowledge about the properties of the SCGC mixture as applied in structural elements, and the deployment of in-situ FBG fiber optic strain sensors. First, the results are summarised and discussed in the next section, including evaluations and limitations of the study. After this, conclusions regarding the research questions and results are drawn, and recommendations are discussed.

5.1 Discussion of results

The analyses suggest that the applied FBG strain sensors can provide accurate strain data from the inside of a geopolymer concrete structural member. The strain data is evaluated by referencing data obtained from laboratory tests on smaller specimens using the same concrete mixture, analytical methods, methods from Eurocode 2, and strain measurements from LVDTs during load testing.

The prestressing losses of the tendons inside the precast girders are estimated in Chapter 4.1 using FBG strain data obtained during curing. Using an analytical model, the cracking moment during flexural testing is estimated at ±150 to 160 kN using these prestressing losses. During the flexural test, the first crack initiation was observed at 117 kN, which is ±25% lower than expected.

A major factor is most likely the susceptibility of this concrete to drying. FBG measurements are representative of concrete in the core of the girder. The concrete at the core of the girder experiences limited effects of drying due to the distance to the surface of the cross section that is exposed to drying conditions. Concrete at the bottom of the girder cross section, where the initial crack occurred, is exposed to a drying environment to a much larger degree. This results in higher drying shrinkage, and a lowering of the elastic modulus. This in turn, leads to a lower cracking load than expected using predictions based on the FBG measurements. This shows that the cross section location of the FBG sensors in the concrete girder is important to take into account when evaluating and interpreting the strain data.

The transmission length of the tendons inside of the precast girder is investigated using comparisons with EC2 analytical methods in Chapter 4.2. The measurements used for this analysis are the measurements performed right before the release of prestressing, and right after prestressing. This is done to minimize the effect of creep and shrinkage on the measured strains. In addition to this, some, but not all FBG sensors were located in the same cross section as the gaps that are present for the topping reinforcements to pass through. This has an effect on the strain measurements due to less concrete in the cross section. This has been accounted for in the analysis, but could lead to inaccuracies due to assumptions.

The results of the transmission length analysis indicate that the transmission length of the prestressed precast SCGC girder is comparable with the transmission length of OPC-based concretes following calculations using EC2. This is in line with expectations following literature regarding the bond strength of geopolymer concretes in comparison with OPC-based concretes, and bond strength resulting from pull-out tests. However, a bigger sample size and more measuring points in the longitudinal axis are needed to give more insight of the progression of strains in the SCGC girder.

The data obtained during the flexural test has been validated, and analysed in different ways in Chapter 4.3. First off, the in-situ elastic modulus of the concrete is estimated by checking the linear relation between stress and strain during the lower load phases of the test. A range of 33 to 35 GPa was obtained to be the in-situ E-modulus. This E-modulus range is within the range of expectations, albeit on the high end, following lab-tests performed on samples of this SCGC mixture that has limited

exposure to drying conditions. Midspan deflection measurements have been used to estimate the apparent E-modulus of the entire cross section and found to be between 28 and 30 GPa. Considering this result, and the susceptibility of this concrete to drying, the in-situ E-modulus range is plausible.

Analytical models have been created to validate the strains as measured by the FBGs during the flexural test. The measured strains seem to follow these conventional prediction methods during both the uncracked phase and the cracked phase.

The strain measurements during the flexural test suggest that the FBGs are able to detect the presence of nearby cracks. As the load keeps increasing during the flexural test, the measured strains diverge from strains following the linear elastic model. This indicates that the concrete around the FBG sensors are experiencing a higher amount strain. This can be attributed to the effect of nearby cracked concrete. As the cracked concrete near the bottom of the girder cannot transfer tensile forces, the remaining uncracked concrete below the neutral axis, steel tendons and reinforcements have to transfer a larger force. This in turn, results into a higher stress and (measured) strain.

This behaviour is also modelled in the nonlinear model. This model has validated the FBG results, showing a comparable amount of strain during load testing. The measurements suggest that the FBGs are capable of detecting nonlinear strain at a lower load than expected from the models, resulting in a small transitional gap between the two models, compared to FBG measurements.

Regarding the position of the FBGs in the cross section of the girder, as the FBG sensors are located in the core of the girder, too deep into the structure, surface level crack detection such as DIC (Digital Image Correlation) is found to be not applicable to cross reference with the FBG data to accurately determine crack positions during the flexural test. This is because the crack propagation from the surface to the FBG locations in the core cannot be assumed as a straight continuous line.

The data obtained during the shear test has been evaluated in Chapter 4.4. Possible moments of tendon slip are visible in the measurements, as sudden major strain changes occurred. Tendon slip can be related to problems in the capacity of the tendons to anchor the occurring tensile forces due to the external load. A simple analysis has been performed regarding the total anchorage length at the possible moments of tendon slip, using a strut-and-tie model, and Eurocode 2 Chapter 8.10.2.3. The analysis is inconclusive for the first event, but since the other events occur at higher loads, the approximated total anchorage length of the tendons is not enough to transfer the tensile forces to the concrete, and likely a factor that contributes in the possible bond slip events. This analysis can be improved by applying the entire concrete section and effect of steel reinforcement bars.

The data obtained during the first test on the mock-deck has been evaluated in Chapter 4.5. The strain measurement during the linear load phase of the test has been compared with strains following a beam model, and a model according to the method of Guyon-Massonnet. Both models overestimate the strain, compared to data from the FBGs. LVDT data from sensors on the bottom side of the slab have been used to validate the FBG data, showing the same difference between model and measurements, suggesting a stiffer behaviour of the slab than expected.

Another comparison is made using the deflection near the load patch, comparing it to a deflection estimated with a simply supported beam model. This showed that the deflection measured is higher than estimated, suggesting behaviour of the slab that is less stiff than a beam model, which is more in line with expectations following a concentrated load on the center of the slab, but contrary to the LVDT and FBG strain data comparisons made earlier.

From the strain measurements during the second load test on the mock-deck, it is visible that the FBG positioned closest to the edge experiences the earliest nonlinearity. This position is within the transmission length, where the prestressing force has yet to fully develop. This most likely caused this location to be the earliest to experience tension, resulting in the earliest formation of cracks and crack propagation, as visible in the measured nonlinear strain.

In general, the results indicate that the rebar integrated FBG fiber optic strain sensors can be used to gain in-situ strain data of the prestressed girder, and the mock-deck. Its successful application to gain data on the SCGC mixture as applied in a real world setting suggest that this monitoring method can be used in a larger scale geopolymer concrete structure, such as the proposed bridge deck, to aid in monitoring (in-situ) strain data and possible crack detection.

5.2 Conclusions

This thesis aimed to study the behaviour of precast prestressed geopolymer concrete structural elements with the use of rebar-integrated FBG fiber optic sensors installed in the precast girder. The main research question was: **How can FBG fiber optic sensors be used to monitor and assess the structural behaviour of a geopolymer concrete structural member?**

Strain data obtained from the FBG fiber optics have been obtained during in different stages of the construction and load testing to study the behaviour of the geopolymer concrete structural elements in a real world setting. The main findings resulting from the study are presented below.

1. Results suggest that the FBG strain measurements in the first two days after casting the geopolymer concrete are not accurate. This is due to inconsistent strain changes observed in the FBG measurements in the first two days after casting.

2. The location of the FBG-integrated rebar in the girder cross section is concluded to be a major influence on the measured strain and the derived material properties, when compared to expected values following lab tests. The sensors are located in the core of the cross section, which measure strains of concrete that has limited exposure to drying conditions, whereas concrete near the surfaces experience a larger effect of drying.

3. Results from the transmission length analysis suggest that the transmission length of the prestressed precast SCGC girder is comparable with the transmission length of OPC-based concretes following calculations using EC2. However, more samples and more data is needed in the longitudinal axis of the girder to gain more knowledge about this behaviour.

4. Following a linear analysis on FBG data from the flexural test on the beam consisting of a SCGC precast prestressed girder and a ready-mix geopolymer concrete topping, it is suggested that the geopolymer concrete in the core of the precast girder has an E-modulus range of ±33 to 35 GPa at 56 days after casting.

5. The results of the flexural test measurements suggest that the internal FBG sensors are able to detect the presence of nearby cracks. This is perceivable as a nonlinear strain increase versus the increase in load during flexural load testing.

6. FBG data collected indicate limited damage to the mock-deck following the cyclic load test. From the first static load test after the cyclic load test, strain data from FBGs and bottom side LVDTs are in agreement with eachother and suggest stiffer behaviour of the slab, when compared to strains resulting from a beam model and a model using the Guyon-Massonnet method. As these models are already conservative, the difference in strain is not able to be explained currently, other than possible issues in the used models.

7. The deflection of the slab near the load patch as measured by LVDTs has been compared with a deflection following a simply supported beam model and found to be larger. This is more in line with the expectation of a point load on a slab, but is opposite to the findings of the FBG and LVDT strain data in the previous point.

Overall, the data that the (rebar-integrated) FBG strain sensors can be of great use towards the larger task of bringing geopolymer concrete structures to a real life application. In-situ FBG strain data of the precast prestressed girders provide additional information into the application of this SCGC mixture in larger scale structural elements. This data is a useful addition to the data gained through conventional methods, and results from lab testing. FBG monitoring can provide accurate strain data from the core of structural elements, giving an insight of the behaviour during curing and (destructive) testing that is otherwise difficult to obtain. In general, the results suggest that this monitoring method can be used in a larger scale geopolymer concrete structure, such as the proposed bridge deck, to aid in monitoring (in-situ) strain data and possible crack detection.

5.3 Recommendations

For monitoring using the rebar-integrated FBG fiber optic system, it is recommended to evaluate the position inside of the cross section depending on its function. For early crack detection, a position closer to the expected crack location is advised, as the position used in this study is too far away to detect early cracks that were occurring in the bottom of the girder. The location in the middle of the cross section also resulted in inability to use DIC results to determine the effect of cracks in the strains measured by the FBGs. A position closer to the edge where DIC monitoring is going to occur will allow the ability to connect the data.

A position near the edge of the girder cross section will also allow data collection of geopolymer concrete that has been exposed to drying conditions. The FBG-integrated rebars applied in this study are located in the core of the girder and the measured strains are representative of concrete with a low exposure to drying conditions. Sensors located in different locations in the cross section could provide an insight into the effects of drying on the geopolymer concrete when applied in the form of a structural element. This study used one set of FBGs per girder, if multiple sets are used in a single structural member, data from the different sets can be used to gain an insight on the effects of drying on geopolymer concrete in the girder cross section.

A recommendation for further research is the apparent transmission length in the precast prestressed geopolymer girders. Additional sensors that reach further into the girder in the longitudinal axis are recommended to increase the accuracy and further analyse the behaviour. A larger amount of samples is also recommended, as this study only investigated 2 prestressed girders.

For the general use of the interrogator and FBG measuring, it is recommended to keep measuring without changing the frequency often. A static frequency between 5-20 Hz is recommended for monitoring. This allows a sufficient frequency of strain measurements, while also limiting file sizes for processing of the data.

For future work, the results of the shear test and mock-deck tests could be examined in greater detail. The FBG data from the shear test and the tests performed on the mock-deck were more complicated to evaluate using analytical methods. The results of analyses performed on the first test of the mock-deck were unexpected. The observed strain in both the in-situ FBGs and LVDTs located at the bottom of the slab were below the predicted strains using both the beam model and a model following the Guyon-Massonnet method. This contrasts with the deflection in the middle of the slab as measured by LVDTs, which was higher, compared with the deflection following the model.

References

Abdel-Jaber, H., & Glišić, B. (2019). Monitoring of long-term prestress losses in prestressed concrete structures using fiber optic sensors. *Structural Health Monitoring, 18*(1), 254-269.

Andrews-Phaedonos, F. (2014). Specification and use of geopolymer concrete. *Austroads Bridge Conference, 9th, 2014, Sydney, New South Wales, Australia.*

Bažant, Z. P., & Jirásek, M. (2017). *Creep and Hygrothermal Effects in Concrete Structures.* Evanston, Prague: Springer.

Berndt, M., Sanjayan, J., Castel, A., Rajeev, P., & Heidrich, C. (2015). *Progress Towards a Handbook for Geopolymer Concrete.* Melbourne: Conference: Concrete 2015.

Chatziaras, N., Psomopoulos, C., & Themelis, N. (2014). Use of alternative fuels in cement industry. *12th International Conference on Protection and Restoration of the Environment*, (pp. 521-529). Skiathos island.

Collins, F., & Sanjayan, J. (1999). Workability and mechanical properties of alkali activated slag concrete. *Cement and Concrete Research, 29*(3), 455-458.

Collins, F., & Sanjayan, J. G. (1999). Strength and shrinkage properties of alkali-activated slag concrete containing porous coarse aggregate. *Cement and Concrete Research*, 607-610.

CORDIS. (2018). *Safe and sustainable geopolymer concrete*. Retrieved from CORDIS: https://cordis.europa.eu/article/id/239529-safe-and-sustainable-geopolymer-concrete

Deb, P. S., Nath, P., & Sarker, P. K. (2015). Drying shrinkage of slag blended fly ash geopolymer concrete. *The 5th International Conference of Euro Asia Civil Engineering Forum. 125*, pp. 594-600. Surabaya: Procedia Engineering.

Derkowski, W., & Dyba, M. (2017). Behaviour of end zone of pre-tensioned concrete elements. *Procedia Engineering*, 19 – 26.

Diaz-Loya, E. I., Allouche, E. N., & Vaidya, S. (2011). Mechanical properties of fly-ash-based geopolymer concrete. *ACI Materials Journal, 108*(3), 300-306.

Du, Y., Sun, B., Li, J., & Zhang, W. (2019). *Optical Fiber Sensing and Structural Health Monitoring Technology.* Wuhan: Springer, Huazhong University of Science and Technology Press.

EN 1992-1-1 (Eurocode 2: Design of Concrete Structures. General Rules and Rules for Buildings). (2004).

Faassen, L. (2021). *FBG optical fibers in proof loading of concrete slab bridges.* Delft: Technische Universiteit Delft, Concrete structures.

Fabris, N., Faleschini, F., & Pellegrino, C. (2020). Bond Modelling for the Assessment of Transmission Length in Prestressed-Concrete Members. *CivilEng, 1*, 75-92.

Fang, G., Bahrami, H., & Zhang, M. (2018). Mechanisms of autogenous shrinkage of alkali-activated fly ash-slag. *Construction and Building Materials*, 377-387.

Geßner, S. (2017). *Bond and anchorage of pre-tensioning tendons.* Aachen: RWTH Aachen University 2019.

Glišić, B., & Inaudi, D. (2007). *Fibre optic methods for structural health monitoring.* Chichester: John Wiley & Sons Ltd.

Hardjito, D., Wallah, S., Sumajouw, D., & Rangan, B. (2004). On the Development of Fly Ash-Based Geopolymer Concrete. *Materials Journal, 101*(6), 467-472.

Hill, K., Fujii, Y., Johnson, D. C., & Kawasaki, B. (1978). Photosensitivity in optical fiber waveguides: Application to reflection filter fabrication. *Applied Physics Letters*.

Hoyer, E., & Friedrich, E. (1939). Beitrag zur Frage der Haftspannung in Eisenbetonbauteilen. *Beton und Eisen, 38*, pp. 107-110.

Kaklauskas, G., Sokolov, A., Ramanauskas, R., & Jakubovskis, R. (2019). Reinforcement Strains in Reinforced Concrete Tensile Members Recorded by Strain Gauges and FBG Sensors: Experimental and Numerical Analysis. pp. 19(1), 200.

Li, Z., Liu, J., & Ye, G. (2019). Drying shrinkage of alkali-activated slag and fly ash concrete; A comparative study with ordinary Portland cement concrete. *Heron, 64*(1-2), 149-163.

Lu, T. (2019). *Autogenous shrinkage of early age cement paste and mortar.* Delft: Delft University of Technology. doi:https://doi.org/10.4233/uuid:e06bd615-7fc4-481b-a334-37627f142e3d

Lucy Rodgers. (2018). Climate change: The massive CO2 emitter you may not know about. BBC News. Retrieved January 5, 2023, from https://www.bbc.com/news/science-environment-46455844

Ma, Y., & Ye, G. (2015). The shrinkage of alkali activated fly ash. *Cement and Concrete Research*, 75-82.

Mamlouk, M. S., & Zaniewski, J. P. (2018). *Materials for Civil and Construction Engineers.* Essex: Pearson.

Manfred Kreuzer. (2006). *Strain measurement with fibre Bragg grating sensors.* Darmstadt: HBM.

Marti, P., Alvarez, M., Kaufmann, W., & Sigrist, V. (1998). Tension Chord Model for Structural Concrete. *Structural Engineering International*.

Martí-Vargas, J. R., & Hale, W. M. (2013, December). Predicting Strand Transfer Length in Pretensioned Concrete: Eurocode versus North American Practice. *Journal of Bridge Engineering, 18*(12).

Masson-Delmotte, V., P. Z., Pirani, A., Connors, S., Péan, C., Berger, S., . . . (eds.), B. Z. (2021). *Climate Change 2021: The Physical Science Basis. Contribution of Working Group I to the Sixth Assessment Report of the Intergovernmental Panel on Climate Change.* Cambridge University Press.

Mast, R. F. (1998). Analysis of Cracked Prestressed Concrete Sections: A Practical Approach. *PCI Journal*, 80-91.

Matthys, S., Proia, A., Sun, Y., Ghorbani, S., & Krajnovic, I. (2022). *TEST REPORT – INTERIM VERSION FEB. '22.* Ghent: Ghent University: Magnel-Vandepitte Laboratory.

Mo, K. H., Alengaram, U. J., & Jumaat, M. Z. (2016, September 1). Structural performance of reinforced geopolymer concrete members: A review. *Construction and Building Materials*, pp. 251-264.

Nath, P., & Sarker, P. K. (2017). Flexural strength and elastic modulus of ambient-cured blended low-calcium fly ash geopolymer concrete. *Construction and Building Materials*, 22-31.

Neupane, K., Bajewa, D., Shrestha, R., Chalmers, D., & Sleep, P. (2014). Mechanical properties of geopolymer concrete: applicability of relationship defined by AS 3600. *Concr. Australia, 40*(1), 50-56.

Neville, A. (2011). *Properties of concrete, 5th edition.* Harlow: Pearson Education Limited.

Nitsch, A. (2001). *Spannbetonfertigteile mit teilweiser Vorspannung aus hochfestem Beton.* Aachen: RWTH Aachen University.

Peterman, R. J. (2007). The Effects of As-Cast Depth and Concrete Fluidity on Strand Bond. *PCI Journal*, 72-101.

Pineda, J. P. (2022, August). *Structural performance of geopolymer concrete: Shear and flexural behavior of a prestressed girder with cast in-situ topping under short-term loading.* Master thesis, Delft.

Provis, J. L. (2018). Alkali-activated materials. *Cement and Concrete Research*, 40-48.

Roy, D. M., & Idorn, G. M. (1982). Hydration, Structure, and Properties of Blast Furnace Slag. *ACI Journal Proceedings*.

Rüsch, H., Jungwirth, D., & Hilsdorf, H. K. (1983). *Creep and Shrinkage Their Effect on the Behavior of Concrete Structures.* New York: Springer-Verlag.

Sigrist, V., & Marti, P. (1994). Ductility of structural concrete: A contribution. *Workshop on Development of EN 1992 in Relation to New Research Results and to the CEB-FIP Model Code 1990* (pp. 211-223). Prague: Czech Technical University.

Simpson, A. (2005). *Optical Fiber Sensors and Their Interrogation.* Birmingham: Aston University.

Suleman, A. (2001). *Smart Structures: Applications and Related Technologies.* Springer-Verlag Wien GmbH.

Taylor, M., Tam, C., & Gielen, D. (2006). *Energy Efficiency and CO2 Emissions from the Global Cement Industry.* Paris: International Energy Agency.

The Boston Consulting Group. (2013). *The Cement Sector: A Strategic Contributor to Europe's Future.* Retrieved from Cembureau: http://cembureau.eu/media/cq5psr22/strategiccontributoreurope_bcg_2013-03-06.pdf

Wardhono, A., Gunasekara, C., Law, D. W., & Setunge, S. (2017). Comparison of long term performance between alkali activated slag and fly ash geopolymer concretes. *Construction and Building Materials, 143*, 272-279.

Zhang, S., & Ye, G. (2021). *Phase I additional results.* Delft: Microlab, Faculty of Civil Engineering & Geosciences, Delft University of Technology.

Zhang, S., Cheng, H., & Yang, Y. (2022). *Monitoring of Prestressed Geopolymer Girders using Smart Aggregates and Fibre Optic Sensors.* Delft: TU Delft.

List of figures

Appendix A: Technical drawings

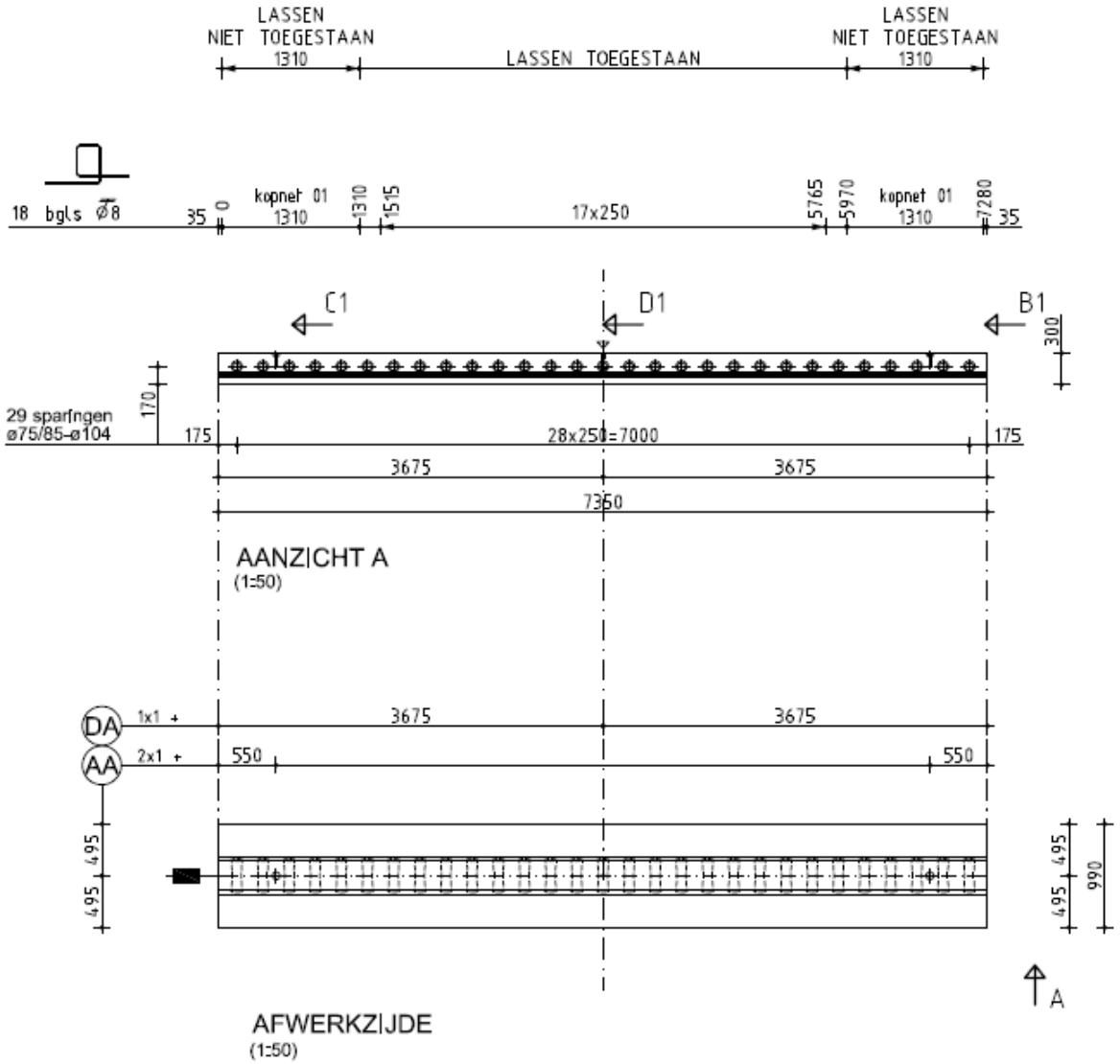

24-06-21	A
Datum:	Uitg.:
Schaal:	1:50

Tekeningnummer: 3089 KO-01

VOOR (PREFAB)-BETONCONSTRUCTIES IN:
- WEG- EN WATERBOUW - UTILITEITSBOUW

haltsma
BETON

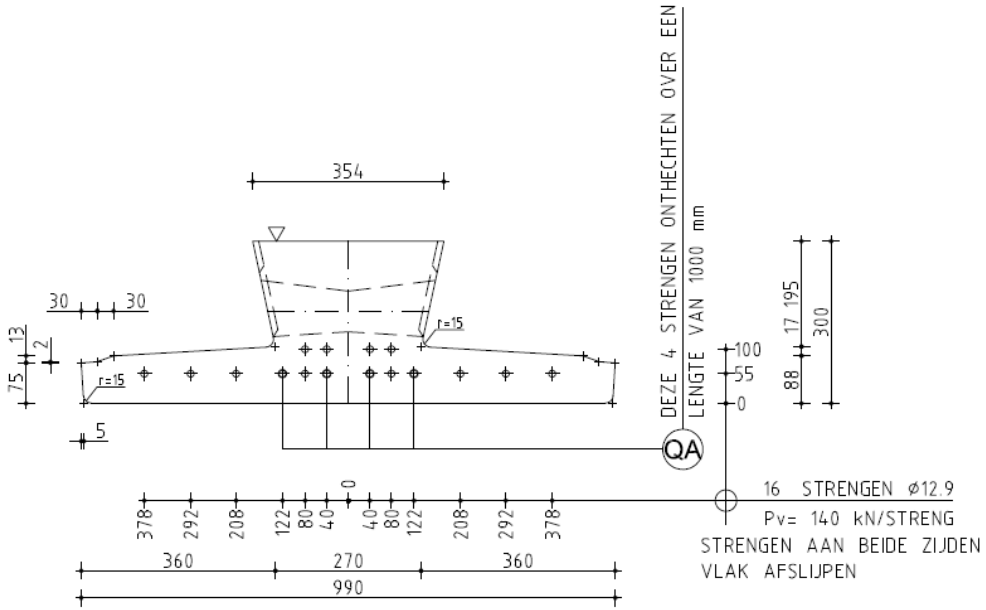

AANZICHT B1
(1:10)

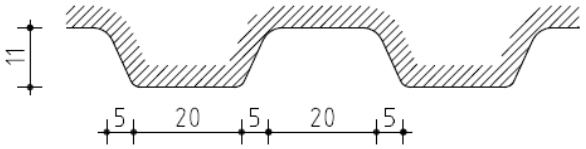

Detail ribbels

23-07-21	B
24-06-21	A
Datum:	Uitg.:
Schaal:	1:10

TekenIngnummer: 3089 KO-D1

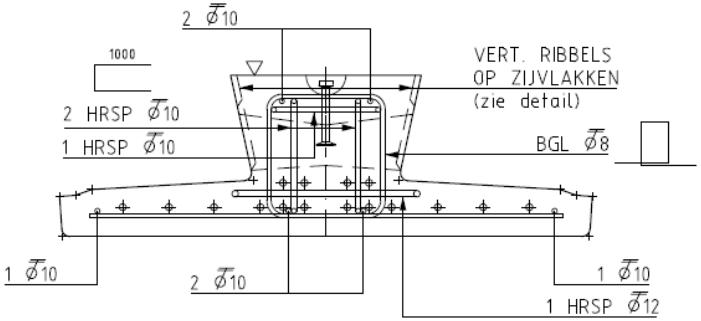

DOORSNEDE C1
(1:10)

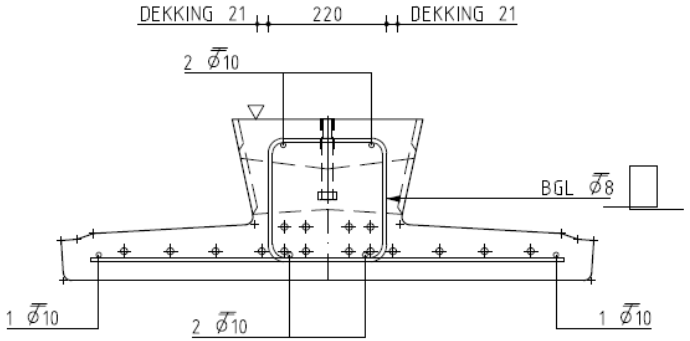

DOORSNEDE D1
(1:10)

23-07-21	B
24-06-21	A
Datum:	Uitg.:
Schaal:	1:10

Tekeningnummer: 3089 KO-D2

KOPNET 01

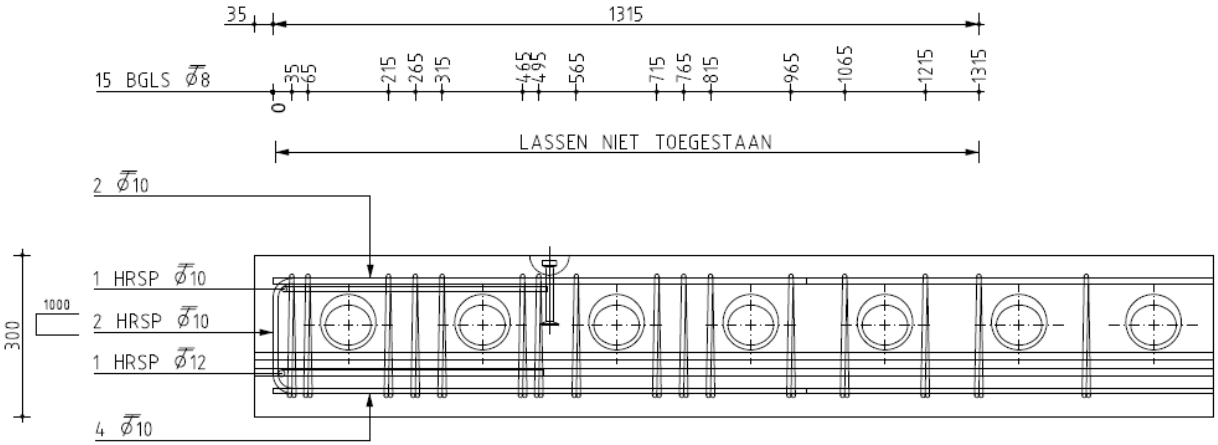

ZIJAANZICHT

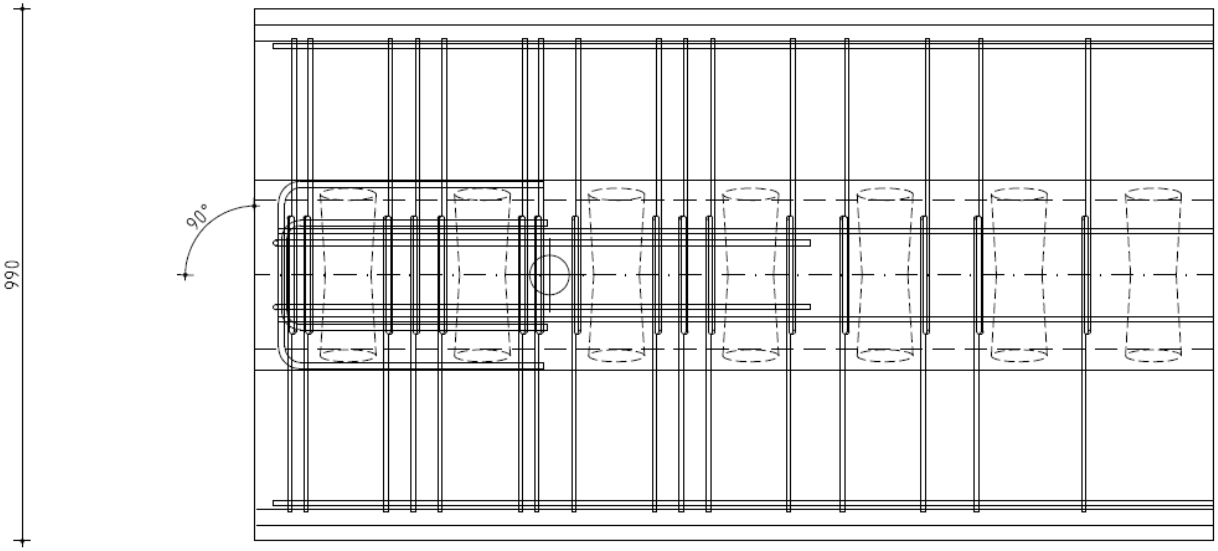

AFWERKZIJDE

DETAIL BALKEINDE KO-01

24-06-21	A
Datum:	Ultg.:
Schaal:	1:10

Tekeningnummer: 3089 KO-D3

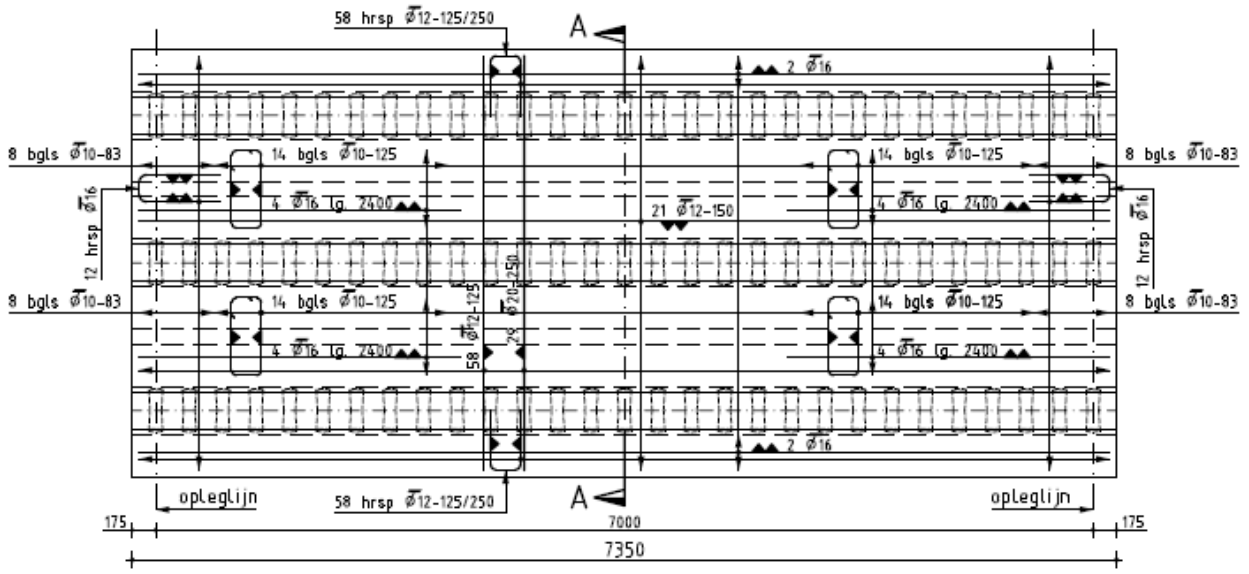

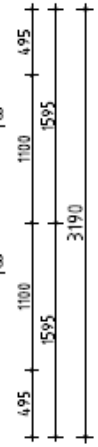

DEKKING = 50 mm

Bovenaanzicht (1:40)
(druklaag met 3 liggers)

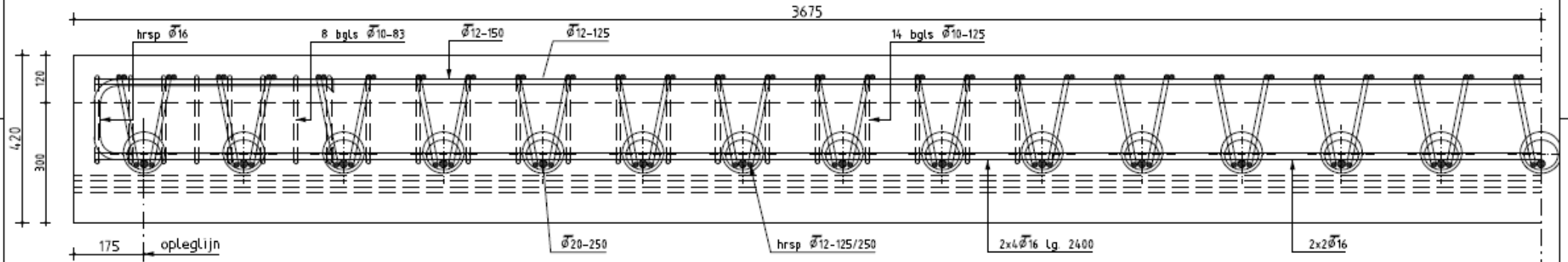

Half zijaanzicht (1:10)

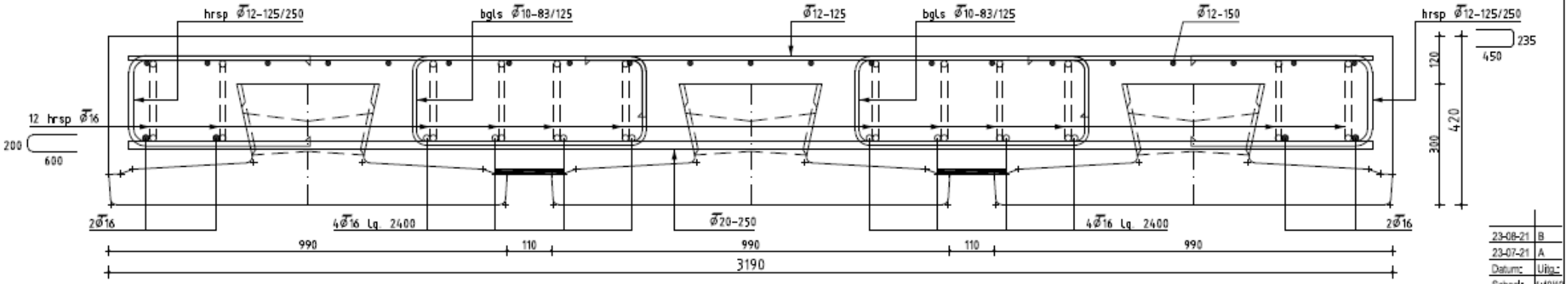

Doorsnede A-A (1:10)

23-08-21	B
23-07-21	A
Datum:	Uitg.:
Schaal:	1:40/10

Tekeningnummer: 3089 DR-01

haitsma BETON

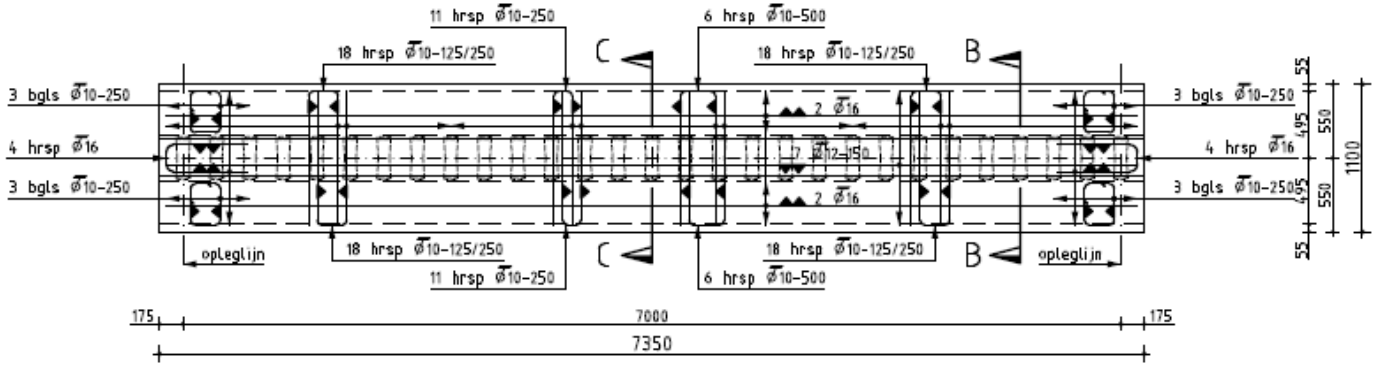

Bovenaanzicht (1:40)

(druklaag met 1 ligger)

DEKKING = 50 mm

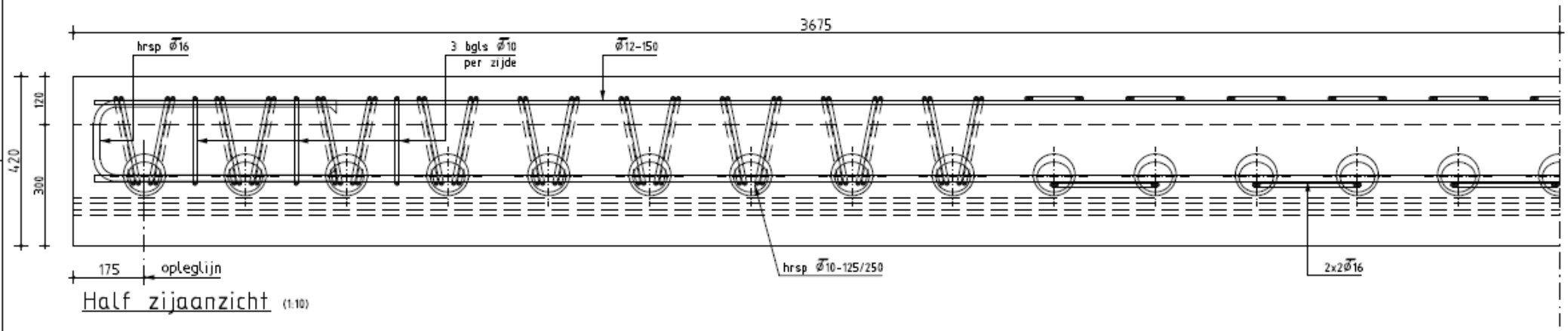

Half zijaanzicht (1:10)

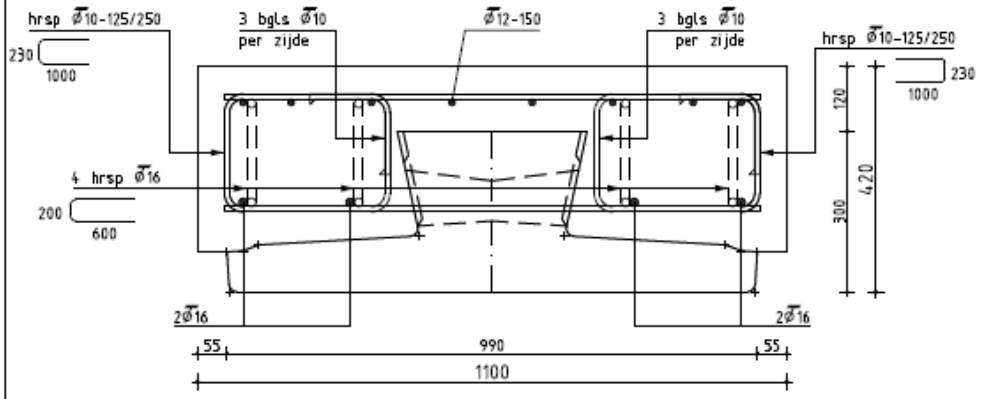

Doorsnede B-B (1:10)

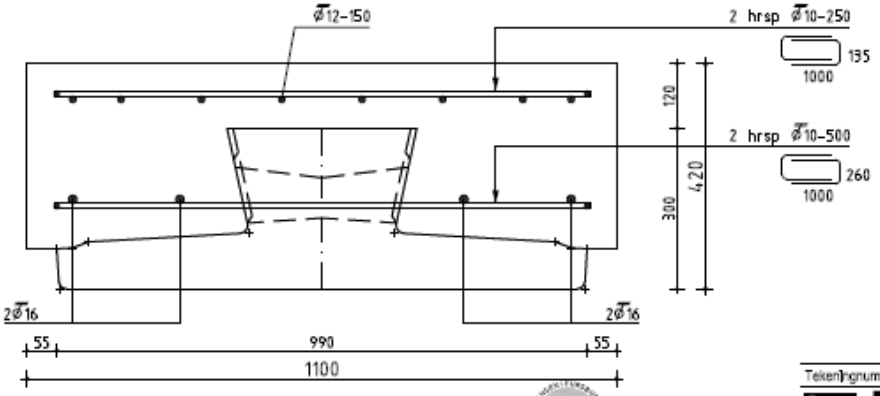

Doorsnede C-C (1:10)

23-08-21	B
23-07-21	A
Datum:	Uitg.:
Schaal:	1:40/10

Tekeningnummer: 3089 DR-02

voor (PREFAB)-BETONCONSTRUCTIES IN
- WEG- EN WATERBOUW - UTILITEITSBOUW

haitsma BETON

Appendix B1: Cyclic loading test setup

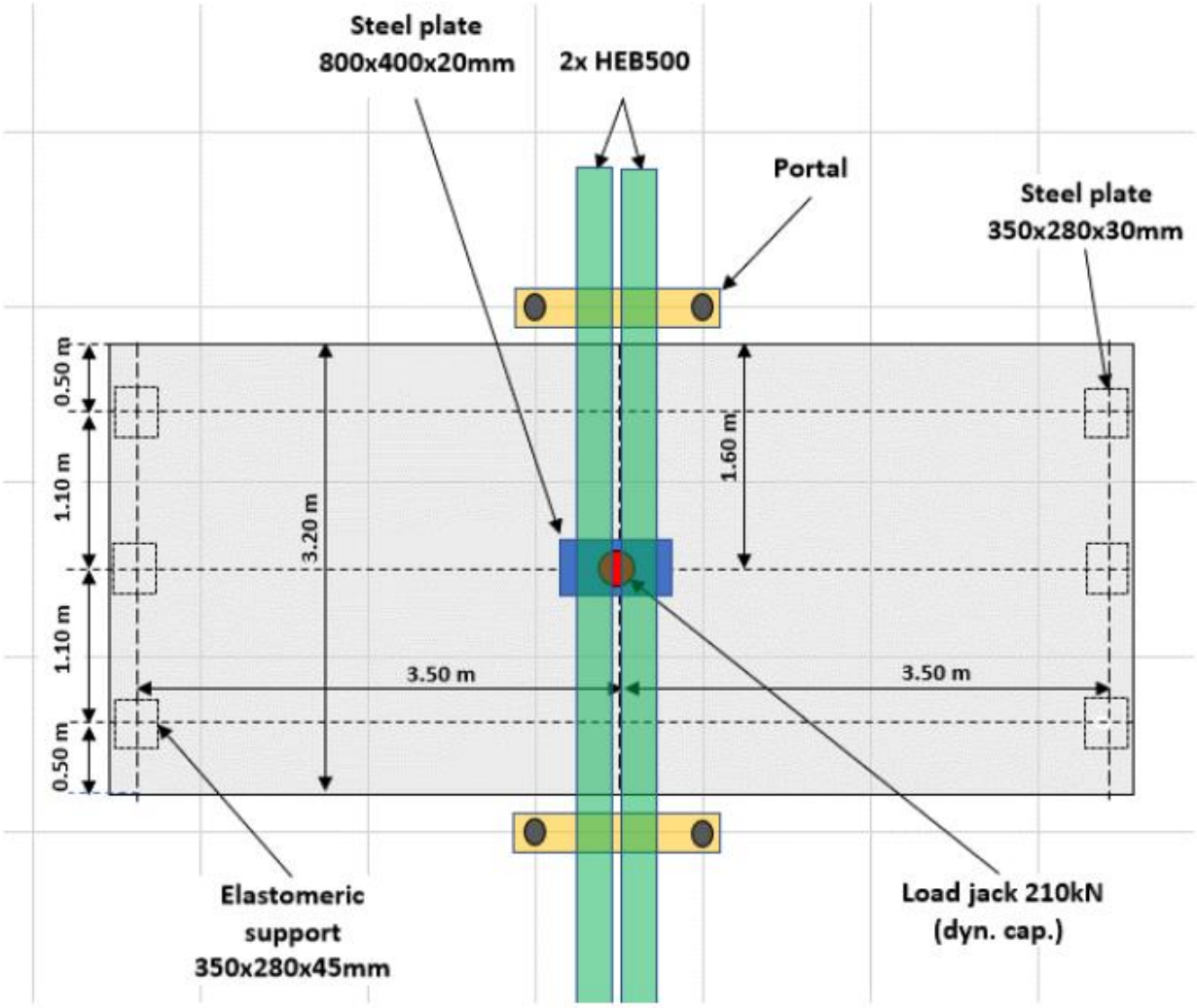

Appendix B2: Cyclic loading test measurements

Measurements performed at maximum (200 kN) and minimum loading (20 kN) during the test show no significant consistent changes in strain from the start to the end of the cyclic loading test at 3 million cycles. This indicates a minimal amount of damage as measured by FBG strain.

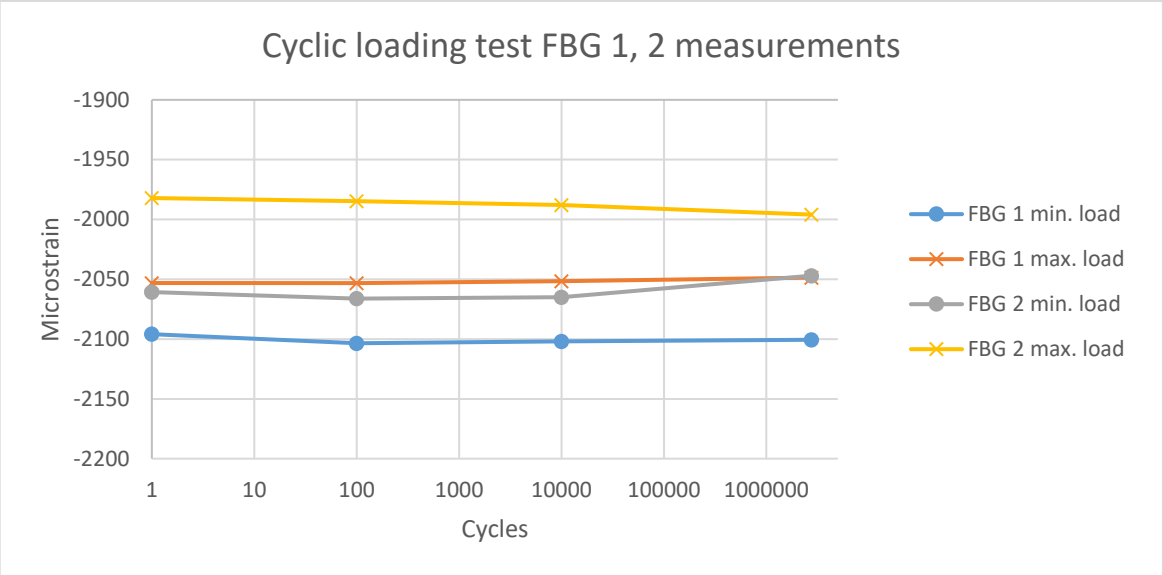

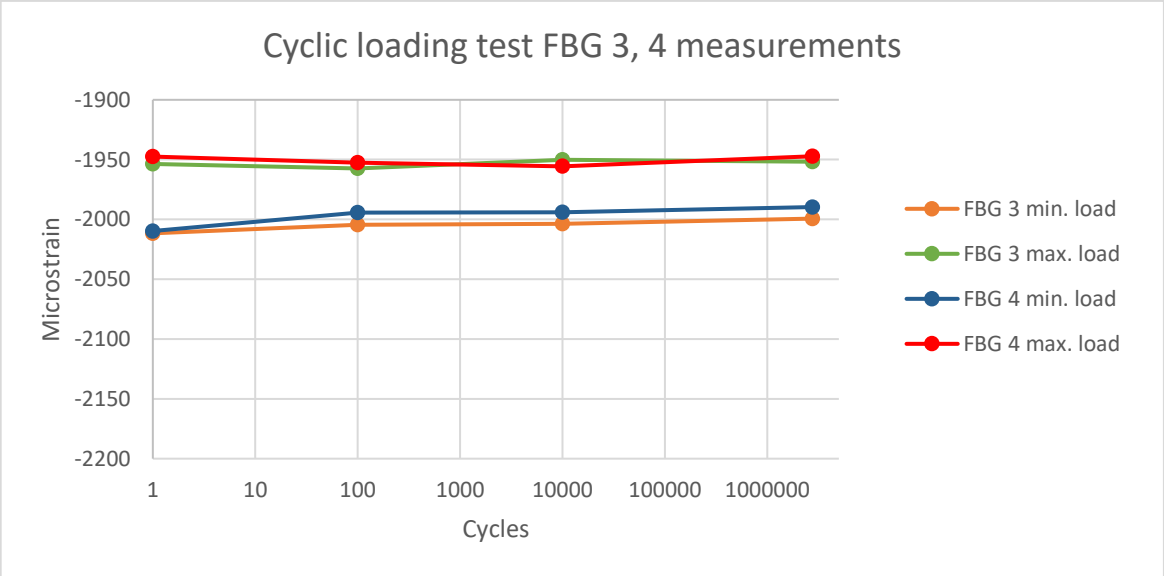

Appendix C: Modified cross section calculation details

When considering the lower bound E-modulus of the precast girder at 25.5 GPa and 26 GPa for the cast topping. They are assumed to be equal enough to not have a significant impact on the moment of inertia of the combined section. As $n = E_{topping} = E_{girder}$= 26/25.5 = 1.02

For the upper bound of the girder E-modulus at 30GPa, the ratio $n = E_{topping} = E_{girder}$= 26/30 = 0.87
To compensate the moment of inertia, the width of the topping needs to be multiplied by this ratio to obtain an equivalent cross section with an overall E-modulus of 30 GPa. Since the cross section of this topping is somewhat irregular, it is too complex to calculate by hand. AutoCAD has been used to assist in this.

The original cross section looks like the following:

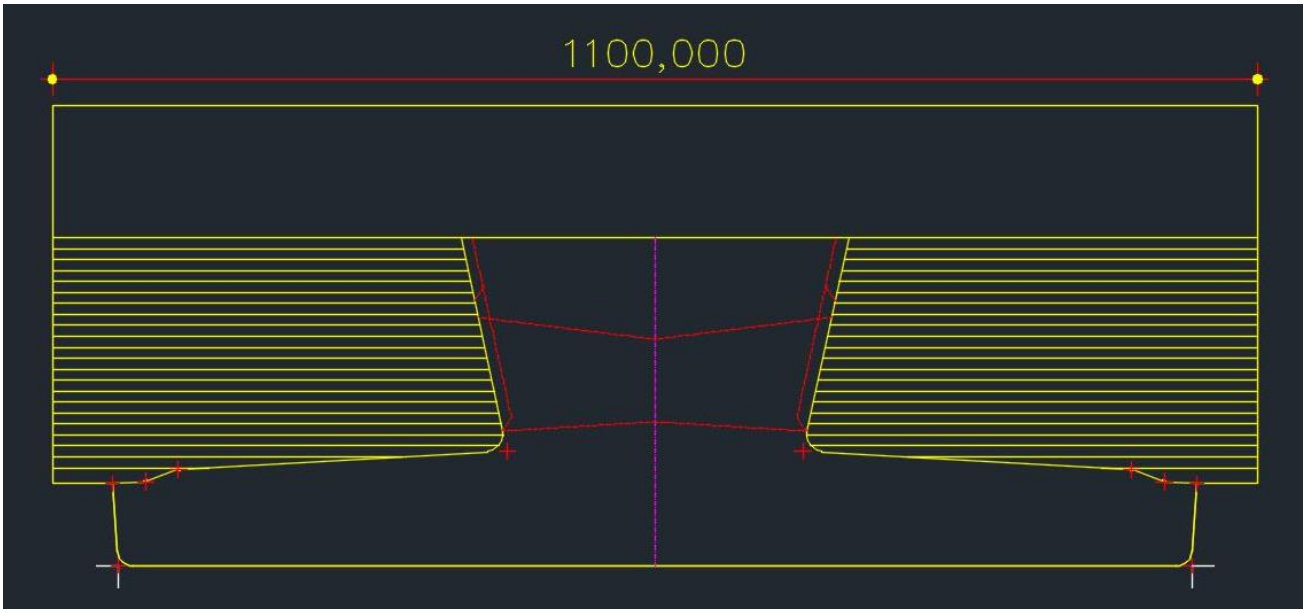

Where the topping alongside the precast girder is split into slices of 10 mm to accommodate for the ratio multiplication of 0.87. The properties of the original cross section are as follows:

```
Command:
Command: MASSPROP
Select objects: 1 found
Select objects:
 ----------------   REGIONS   ----------------
Area:                      453292
Perimeter:                 3019
Bounding box:           X: -550  --  550
                        Y: -214  --  206
Centroid:               X: 0
                        Y: 0
Moments of inertia:     X: 6520554276
                        Y: 44219765039
```

After modifying the topping widths according to the ratio n = 0.87 , the new cross section is as follows:

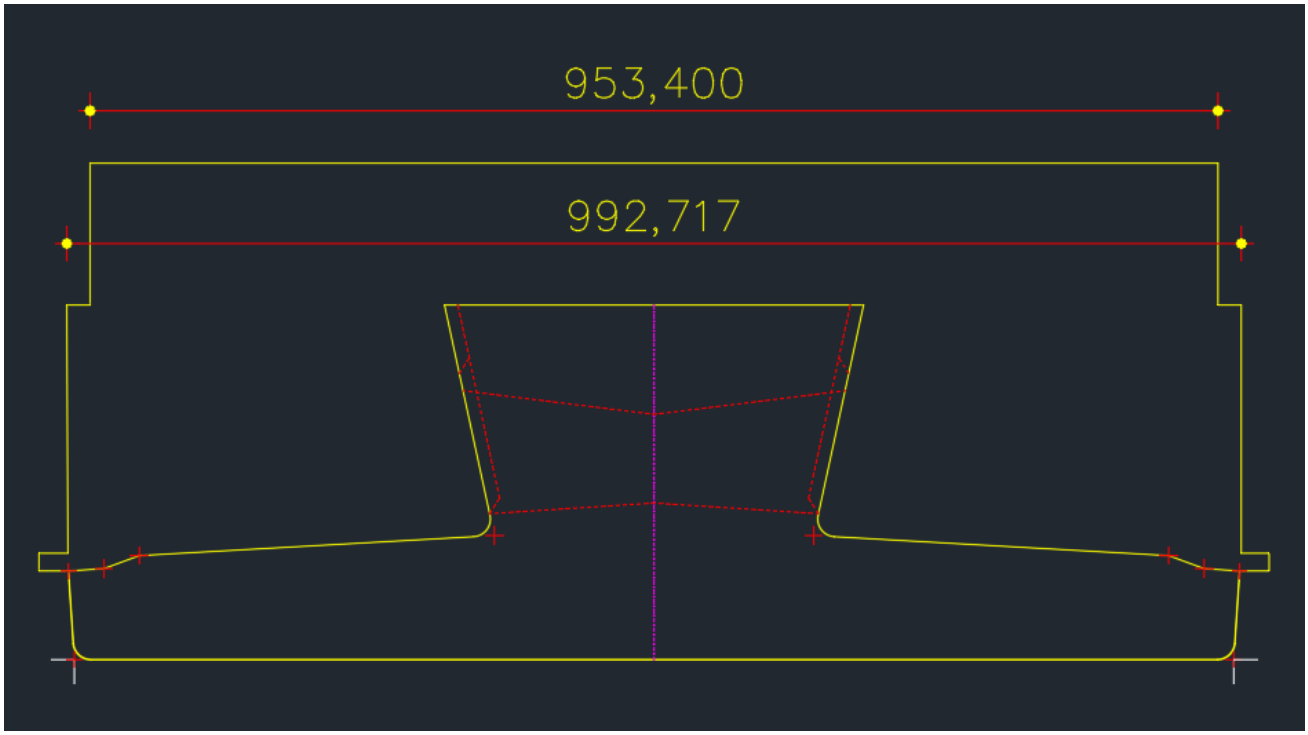

With a notable bulge near the bottom of the topping due to the nature of that slice. The moment of inertia is 600×10^6 mm^4, which is 9% lower than the moment of inertia with equal E-modulus for topping and girder. The center of gravity also shifts down by 5 mm, this has an effect on the stress distribution. Details of the cross section analysis are shown below.

```
----------------   REGIONS   ----------------
Area:                    412175
Perimeter:               2900
Bounding box:          X: -520  --  520
                       Y: -209  --  212
Centroid:              X: 0
                       Y: 0
Moments of inertia:    X: 6004521336
                       Y: 33122492648
```